Summer 2014

Cylinder Block / Valve Plate Interface Performance Investigation Through The Introduction Of Micro-Surface Shaping

Rene Chacon Portillo
Purdue University

Graduate School ETD Form 9
(Revised 01/14)

PURDUE UNIVERSITY
GRADUATE SCHOOL
Thesis/Dissertation Acceptance

This is to certify that the thesis/dissertation prepared

By Rene Chacon Portillo

Entitled
CYLINDER BLOCK / VALVE PLATE INTERFACE PERFORMANCE INVESTIGATION THROUGH THE INTRODUCTION OF MICRO-SURFACE SHAPING

For the degree of Master of Science in Mechanical Engineering

Is approved by the final examining committee:

Monika Ivantysynova

Andrea Vacca

Farshid Sadeghi

To the best of my knowledge and as understood by the student in the *Thesis/Dissertation Agreement. Publication Delay, and Certification/Disclaimer (Graduate School Form 32)*, this thesis/dissertation adheres to the provisions of Purdue University's "Policy on Integrity in Research" and the use of copyrighted material.

Monika Ivantysynova

Approved by Major Professor(s): _____

_____

Approved by: David Anderson 07/21/2014

Head of the Department Graduate Program Date

CYLINDER BLOCK / VALVE PLATE INTERFACE PERFORMANCE INVESTIGATION THROUGH THE INTRODUCTION OF MICRO-SURFACE SHAPING

A Thesis

Submitted to the Faculty

of

Purdue University

by

Rene Chacon

In Partial Fulfillment of the

Requirements for the Degree

of

Master of Science in Mechanical Engineering

August 2014

Purdue University

West Lafayette, Indiana

To my family

ACKNOWLEDGEMENTS

First of all, I would like to thank my advisor Dr. Monika Ivantysynova for the support, guidance and encouragement throughout my research here at MAHA Fluid Power Research Center. You taught me to challenge myself during these last two years and offered me invaluable guidance and knowledge all throughout my Master's degree. And in times in which I needed help, you were always there for me.

Second, I would like to thank my family, although, they are far away from Lafayette, IN. Their unconditional support all throughout my student life has been of the upmost importance for me. None of these would be possible without their support, many thanks for all.

Third, there are a number of colleagues which have been my friends during my stay here at MAHA. Special thanks to Marco Zecchi for his mentorship and friendship throughout my first months here at the lab. Many thanks to Andrew for his invaluable help with everything from taking care of the computer cluster Condor (which I used extensively), to the endless discussions on the research topic, sharing your knowledge, and for your friendship. Enrique, Ram, Matteo Pellegri, Nils, Dan, Taeho, Lizhi, Natalie, and Ashley, and many more for making my days at Maha always fun. I thank you all for being my friends.

Finally, I would like to thank the staff at Maha. Special thanks to Susan Gauger for being such a good person. You really keep this place going, you were of the biggest help to me when I needed it. For that I thank you. Also, Connie and Anthony, thank you for your work here at Maha, you make this place a unique place in the world.

TABLE OF CONTENTS

Page

LIST OF TABLES

LIST OF FIGURES

Figure Page

Figure Page

Figure Page

Figure Page

Figure Page

NOMENCLATURE

a	Acceleration	[m/s^2]
A	Area	[m^2]
A_0	Displacement chamber opening are	[m^2]
A_D	Surface area at the bottom of the displacement chamber	[m^2]
A_K	Piston surface area	[m^2]
b	Breadth	[m]
d_K	Piston diameter	[m]
h	Gap height	[m]
K	Bulk modulus	[Pa]
M	Torque	[Nm]
H_K	Piston stroke	[m]
F	Force	[N]
F_{BZ}	Resulting force in an axial direction	[N]
F_{FB}	Spring force	[N]
F_{DB}	Force due to pressure in displacement chamber, applied to the block	[N]
F_{DK}	Force due to pressure in displacement chamber, applied to the piston	[N]
F_{TB}	Friction force due to viscous friction in the piston/cylinder interface, applied to the block	[N]
F_{TK}	Friction force due to viscous friction in the piston/cylinder interface, applied to the piston	[N]
Fs_K	Swash plate reaction force	[N]
$F_{\omega B}$	Force due to centripetal acceleration transferred to block	[N]

$F_{\omega K}$	Force due to centripetal acceleration on the piston/slipper assembly	[N]
F_{RB}	Total radial force transmitted to the cylinder block	[Nm]
M	Torque	[Nm]
m_K	Piston mass	[kg]
n	Shaft rotational speed	[rpm]
p	Pressure	[Pa]
Δp	Pressure differential	[Pa]
P	Power	[W]
Q	Flow rate	[m^3/s]
R_b	Pitch radius	[m]
R_B	Outer radius cylinder block	[m]
r	Radial position	[m]
s_K	Piston displacement	[m]
T	Temperature	[°C]
t	Time	[s]
V	Velocity	[m/s]
v_K	Piston velocity	[m/s]
V_g	Geometric displacement	[m^3]
(r,φ,z)	Cylindrical reference system	
(x,y,z)	Cartesian reference system	
β	Swash plate angle	[°]
μ	Dynamic viscosity	[Pa s]
ρ	Oil density	[kg/m^3]
Φ_d	Viscous dissipation	[W]
φ	Shaft angular position	[°]
ω	Angular velocity	[rad/s]

LIST OF ABBREVIATIONS

B	Block
DC	Displacement chamber
LP	Low pressure
HP	High pressure
K	Piston
f	Fluid film
G	Slipper
T	Cylinder bore
CB	Cylinder block
VP	Valve plate
Δ	Variation
l	Loss
S	Leakage
m	Mechanical

ABSTRACT

Chacon, Rene. M.S.M.E., Purdue University, August 2014. Cylinder Block/Valve Plate Interface Performance Investigation through the Introduction of Micro-Surface Shaping. Major Professor: Monika Ivantysynova, School of Mechanical Engineering.

Swash plate type axial piston machines are widely used positive displacement machines in different fields of industry ranging from aerospace, agriculture, automotive, heavy machinery, etc. Lubricating gaps are the main source of energy dissipation in axial piston machines. This type of machines have three lubricating interfaces: slipper/swash plate interface, piston cylinder and the cylinder block/valve plate interface. The cylinder block/valve plate interface being one of the most critical design elements of the machine. Extensive research has been done at Maha Fluid Power Research Center in Purdue University both to model this interface and to study the effects of micro-surface shaping on the solids interacting in this interface. The aim of this work was a more in-depth simulation-based investigation into optimizing the cylinder block/valve plate interface by introducing micro-surface shaping in order to achieve a fluid film thickness that compromises between leakage and viscous friction, maximizing the overall machine performance.

CHAPTER 1. INTRODUCTION

Hydrostatic pumps and motors are positive displacement machines which are the heart of hydraulic systems. They are widely used in industry due to their compactness and high power density; some industry field examples: aeronautical, automotive, agriculture, heavy industries, construction, etc. Hydraulic pumps convert mechanical energy into hydraulic energy, and vice versa hydraulic motors convert hydraulic energy into mechanical energy. There are several types of positive displacement pumps, some of them are axial piston type, gear type, screw type, vane type, etc.

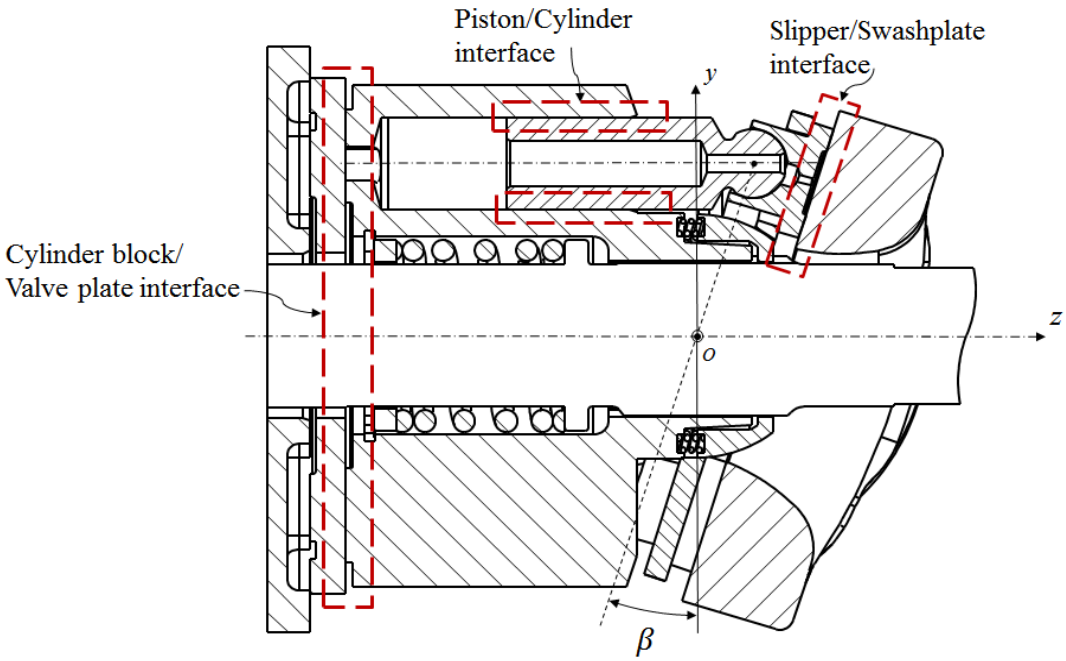

Figure 1.1. Axial piston machine swash plate type cross-section.

Axial piston machines of swash plate type are common positive displacement machines used in a wide range of hydraulic circuits. This type of machine has three lubricating interfaces: the slipper/swash plate, piston/cylinder, and the cylinder block/valve plate.

These lubricating gaps have to fulfill simultaneously a bearing and a sealing function under dynamic load conditions; on the other hand; they represent the main source of energy dissipation due to viscous friction and leakage flow. A cross-section of this machine is represented in Figure 1.1. The cylinder block/valve plate interface being one of the most important designs elements. This interface is also present in axial piston machines of bent-axis type.

1.1 State of the Art

In the last few decades, a lot of research has been conducted in order to understand the physical phenomena in the cylinder block/valve plate interface. The previous work done on this interface can be classified into two main categories: experimental work and the development of models to predict the behavior of the interface. On the experimental research, Yamaguchi (1990) dealt with different valve plate designs; studied the effect of different designs over the leakage in the cylinder block/valve plate interface. Kim (2003, 2005) focused in measuring the fluid film thickness between the cylinder block and the valve plate while using different valve plate designs and under different operating conditions. Furthermore, Bergada (2011) did experimental work in measuring the fluid film thickness in the lubricating interface. More experimental work has been done by Olems (2000), Jouini (2008), and Zecchi (2013) in measuring the temperature in the solid bodies of the interface, since there is a close relationship with the temperature prediction of the interface and the fluid film thickness of the gap.

In the modelling and prediction of performance of these machines as early as 1950 Sartchenko described the various forces acting on the cylinder block without going into much detail of those fluid forces generated in the lubricating gap with the valve plate. Also, Franco (1961) derived for the first time the pressure field in the gap due to the hydrostatic pressure variation in radial direction, although it was only valid for points away from the end of the ports. More researchers have done work on the analytical prediction of the performance of the cylinder block/valve plate interface (Shute and Turnbull, 1964; Hibbert et al., 1971; Taylor and Lin, 1984; Yamaguchi, 1986 and 1990;

Matsumoto, 1991; Manring, 2000; Ivantysyn and Ivantysynova, 2001). These earlier developed models neglected many important physical effects impacting the fluid film behavior like micro motion, surface deformation due to pressure and thermal loading. Therefore these models allowed a very limited prediction of fluid film behavior and machine performance. In more recent years computational power has had great advancements and the cost has also been driven down; allowing for more complex and complete models to be developed and used.

In 2002, Wieczorek and Ivantysynova developed the first model able to predict the fluid film thickness based on the assumption of force balance between external and fluid film forces. The model solved for the force balance between the external loads applied on the cylinder block and the fluid forces in the gap. They solved for the fluid film pressure field by solving the Reynolds and energy equation. The pressure field was generated by means of the hydrostatic pressure coming from the displacement chambers and the ports and also the hydrodynamic effects due to relative motion between the solids. This was big step forward towards a better calculation of the performance of the interface.

Later, elasto-hydrodynamic (EHD) models were developed by Deeken (2003) and Huang and Ivantysynova (2003). In the last, the model developed by Wieczorek and Ivantysynova in 2002 was coupled with FEM commercial software to calculate the elastic deformations due to pressure on the cylinder block surface.
Jouini (2008) extended on Huang's (2003) model to be able to predict the temperatures in the solid bodies, by calculating the heat flux coming from the lubricating gap due to viscous friction. Additionally, experimental work was done to validate the model through the measurement of temperature on the valve plate by embedding thermocouples on the valve plate. The simulation results were able to match the general temperature trends obtained in measurement.

More recently, Zecchi & Ivantysynova (2012) developed a novel fluid structure thermal interaction model able to predict more accurately the behavior of the fluid film. The

model includes different modules capturing the various physical phenomena like micro-motion of the cylinder block, non-isothermal flow in the lubricating gap, and pressure and thermal elastic deformation on the solid bodies; on both, the cylinder block and the valve plate/end case assembly. This model was then validated with temperature measurements on a valve plate of a 130 cc axial piston machine (Zecchi, 2013). These measurements were obtained similarly as in Jouini (2008) thermocouples were embedded into the valve plate a few millimeters away from the running surface. Simulation results matched the temperature measurements closely, within a few degrees.

Previous work on the micro-surface shaping has been done by Hargreaves (1990) and Rasheed (1998), which showed an improvement in the performance of lubricating film in sliding bearings. Baker and Ivantysynova (2008) predicted over a 50% reduction in total energy dissipation for a modified ±1 μm of amplitude and 15 waves in the circumferential direction. The highest reduction in energy dissipation was achieved at low pressure, low speed, and low displacement of a 75 cc/rev unit. The research was conducted using Huang's (2003) model. The authors also manufactured a valve plate prototype and conducted measurements on a pump test rig. The measurements showed an increase of overall pump efficiency of up to 10% (Baker &Ivantysynova (2009). In 2012, Zecchi repeated simulations of Baker's valve plate using his new fluid structure interaction model results showed the same trends however different magnitudes of reduction of energy dissipation. These results can be explained by effect of the elastic deformations due to thermal stresses on the lubrication film behavior. The elastic deformations due to thermal load are in the same order of magnitude as the introduced surface waves. Therefore a more comprehensive study of the impact of surface shaping on energy dissipation and load carrying ability of the fluid film is required using the new fluid structure interaction model developed by Zecchi.

1.2 Aim of this Work

The aim of the work presented in this thesis is to investigate the effects of micro-surface shaping on the cylinder block/valve plate interface utilizing the fluid structure interaction

model developed by Zecchi. The investigation has to be done over a comprehensive range of operating conditions, in order to understand the effect of the micro-surface waviness on the load carrying ability of the interface and the total energy dissipation of the lubricating gap. The trends found in this work will be useful in future design of this lubricating interface.

CHAPTER 2. THE CYLINDER BLOCK/VALVE PLATE INTERFACE

2.1 Introduction to Axial Piston Machines

Axial piston machines are commonly comprised of a rotating group composed by a cylinder block, with finite number of piston/slippers. Each piston/slipper assembly is pushed against the stationary swash plate by means of a fixed hold down or a spring push-down system. The inclination of the swash plate causes the piston/slipper assembly to move axially in and out of the cylinder bore while the cylinder block is rotating. The fluid intake from the machine inlet port takes place when the piston moves from its inner dead center, i.e. the displacement chamber volume increases during the suction stroke. Fluid is displaced to the pump discharge port when the piston moves from its outer dead center to its inner dead center. This type of machines can work both as pump or motor. The machine runs as a motor when high pressure fluid enters the displacement chamber while the piston moves from its inner dead center to its outer dead center. This means that the machine can turn mechanical energy into hydraulic energy; or vice versa, hydraulic energy back into mechanical energy.

2.2 Kinematics of Axial Piston Machines of Swash Plate Type

In the following section the main parameters derived from the machine kinematics of swash plate type axial piston machines are described. The cross section of the machine can be seen in Figure 2.1 with the main coordinate system used to determine the machine's kinematics.

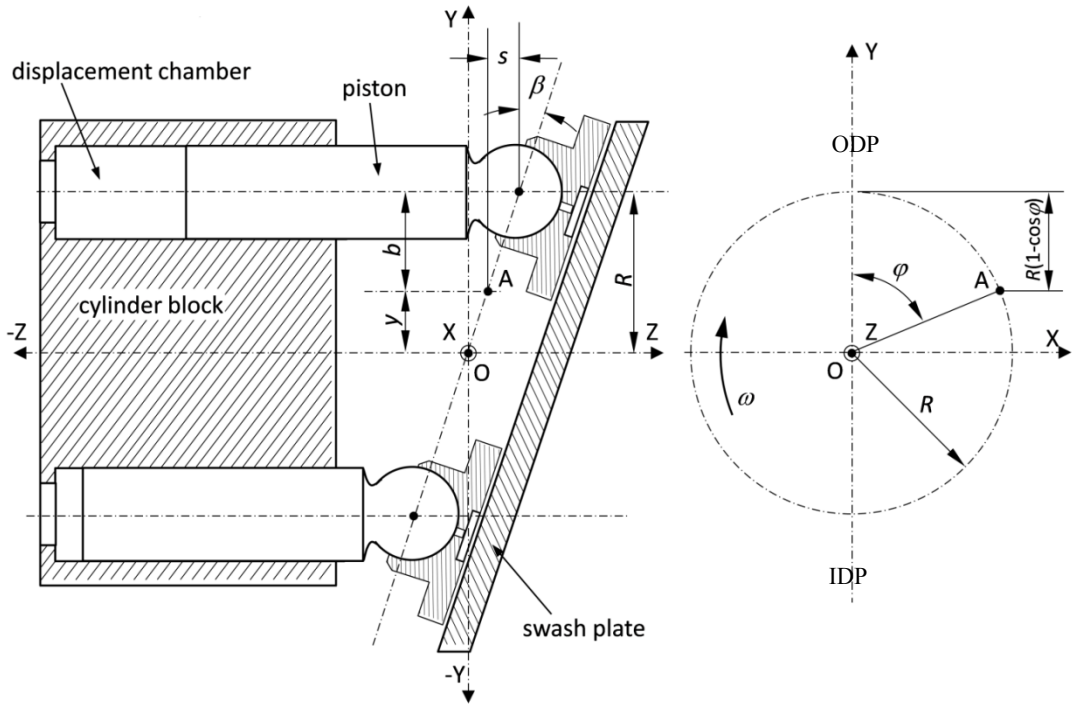

Figure 2.1. Schematic of an axial piston machine (Seeniraj & Ivantysynova, 2009).

The point O, references the origin of the coordinate system, it is determined by the intersection of the shaft axis and the plane parallel to the running surface of the swash plate, which intersects the centers of the ball joints between the slipper and piston. In Figure 2.1 the label ODP stands for the "Outer Dead Point" which is the position where the piston is the farthest from the cylinder bottom. Additionally, here is also where the machine operation transitions from the suction stroke into the delivery stroke. Similarly the label IDC stands for "Inner Dead Point" which is the position where the piston is the closest to the cylinder bottom; also, transitioning now from delivery to the suction stroke.

This position of the piston is indicated with the variable s_K, along the z-axis can be defined as (Ivantysyn and Ivantysynova, 2001):

$$s_K = -z\,. \tag{2.1}$$

From Figure 2.1 follows:

$$z = b \cdot \tan\beta\,. \tag{2.2}$$

And $$b = R - y\,. \tag{2.3}$$

Where $$y = R \cdot \cos\varphi\,. \tag{2.4}$$

$$s_K = -R \cdot \tan\beta(1 - \cos\varphi)\,. \tag{2.5}$$

$$H_K = 2 \cdot R \cdot \tan\beta\,. \tag{2.6}$$

The piston velocity and acceleration are defined as:

$$v_K = -\omega \cdot R \cdot \tan\beta \cdot \sin\varphi\,. \tag{2.7}$$

$$a_K = -\omega^2 \cdot R \cdot \tan\beta \cdot \cos\varphi\,. \tag{2.8}$$

The geometric displacement:

$$V_g = z \cdot A_K \cdot H_K = z \cdot \frac{\pi \cdot d_K^2}{2} \cdot R \cdot \tan\beta\,. \tag{2.9}$$

For the nominal flow:

$$Q_g = n \cdot z \cdot A_K \cdot H_K\,. \tag{2.10}$$

For a more complete derivation of the axial piston machine dynamics please refer to Ivantysyn and Ivantysynova (2001).

2.3 The Function of the Cylinder Block/Valve Plate Interface

The cylinder block/valve plate lubricating gap is one of the more critical design elements in axial piston machines of swash plate and bent axis type. This lubricating interface has to fulfill two main functions; bearing the external loads and sealing the pressurized fluid. The interface requires a sufficiently stable fluid film to bear the loads, and a thin fluid film to seal efficiently the pressurized fluid. Additionally, the cylinder block/valve plate interface represents one of the main sources of energy dissipation of the machine. It is composed by two sources; the leakage flow through the interface and the viscous friction in the fluid. To minimize energy dissipation these losses have opposite requirements. To reduce leakage flow a low fluid film is desired, whereas to minimize viscous friction a thicker fluid film is preferred.

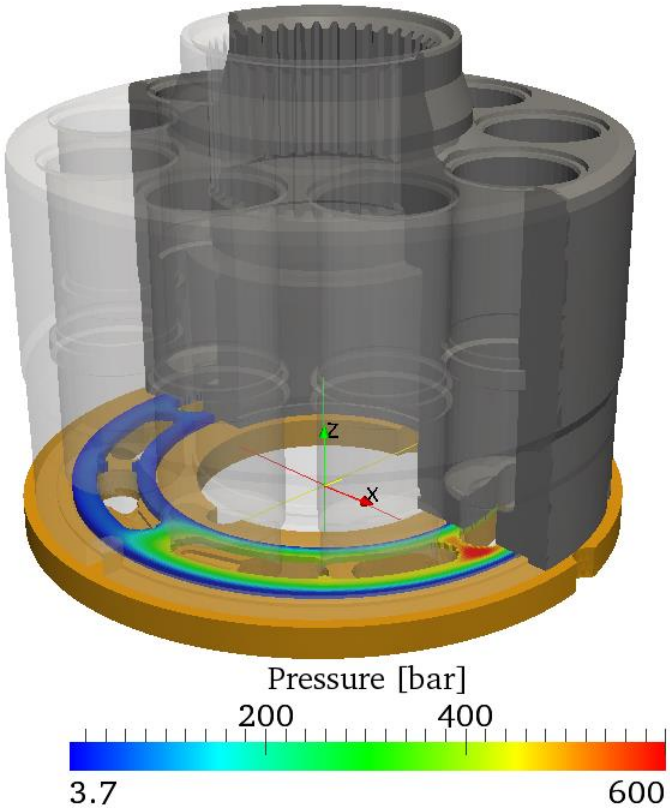

Figure 2.2. Representation of the fluid film between the cylinder block and the valve plate in color the pressure of the fluid is represented.

2.4 External Loads Applied to the Cylinder Block

The loads exerted on the cylinder block can be divided into two main categories. The first one being the loads directly applied to the cylinder block and the second one the loads related to the piston/slipper assembly. It is very important to correctly define the various forces that have an interaction with the cylinder block/valve plate interface in order to be able to understand and predict the performance of the machine.

2.4.1 External Loads on the Cylinder Block

The external forces exerted on the cylinder block are described on this section; and, they are represented in Figure 2.3. The cylinder is loaded simultaneously by all the pistons. The pressure in all the displacement chambers, the transverse forces and frictional forces, which will be transfer from all the pistons have to be considered.

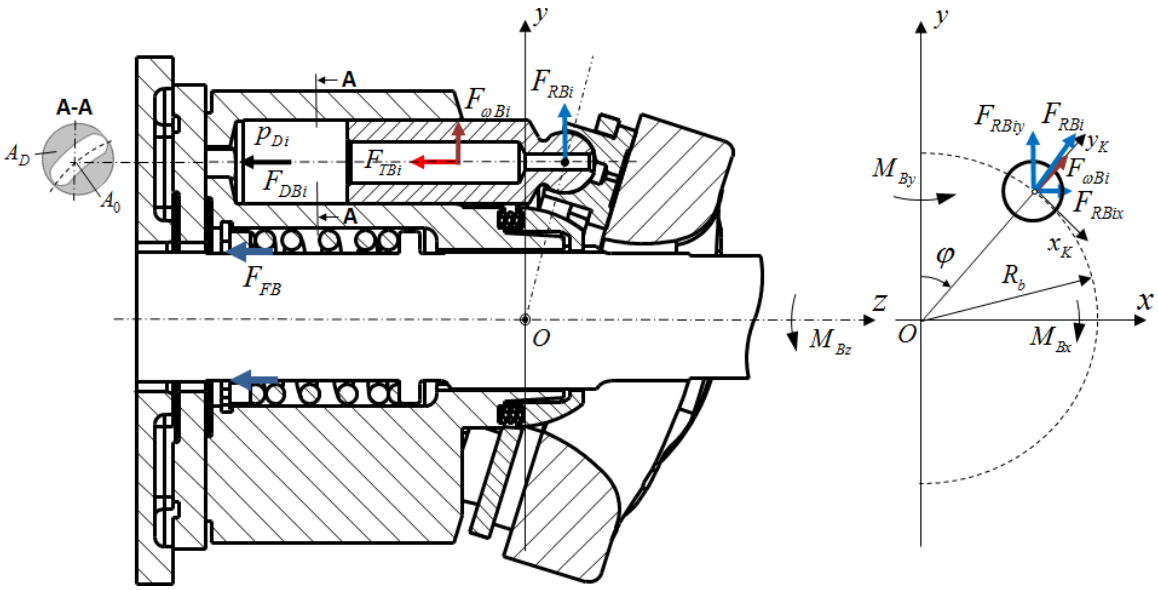

Figure 2.3. Cylinder block free body diagram.

The main force applied on the cylinder block is due to the pressurized fluid in the displacement chamber. The pressure force $F_{DB,}$ pushes on the bottom of the displacement chamber. The surface area at the bottom of the displacement chamber A_D is determined by the diameter of the piston and the area size of the displacement chamber opening.

$$F_{DB} = -p_{Di} \cdot A_D \,. \tag{2.11}$$

The surface area is defined by the geometry; piston diameter d_K and displacement chamber opening area.

$$A_D = d_K^2 \frac{\pi}{4} - A_0 \,. \tag{2.12}$$

Second, the spring force pushes down on the block in direction of the valve plate, on the z-axis, F_{FB}. The spring is placed between the cylinder bore and the shaft in order to prevent the block from tipping under specific operating conditions. Third, the force due to the friction between the piston and the cylinder bore in the piston/cylinder interface, F_{TB}, this force is calculated using a different model developed by Pelosi (2012). Furthermore, the force due to the centripetal acceleration of the piston/slipper assembly, $F_{\omega B}$, acts on the radial direction of the cylinder block, defined as:

$$F_{\omega Bi} = m_K \omega^2 R_B \,. \tag{2.13}$$

The forces acting on the piston/slipper assembly are shown in Figure 2.4.

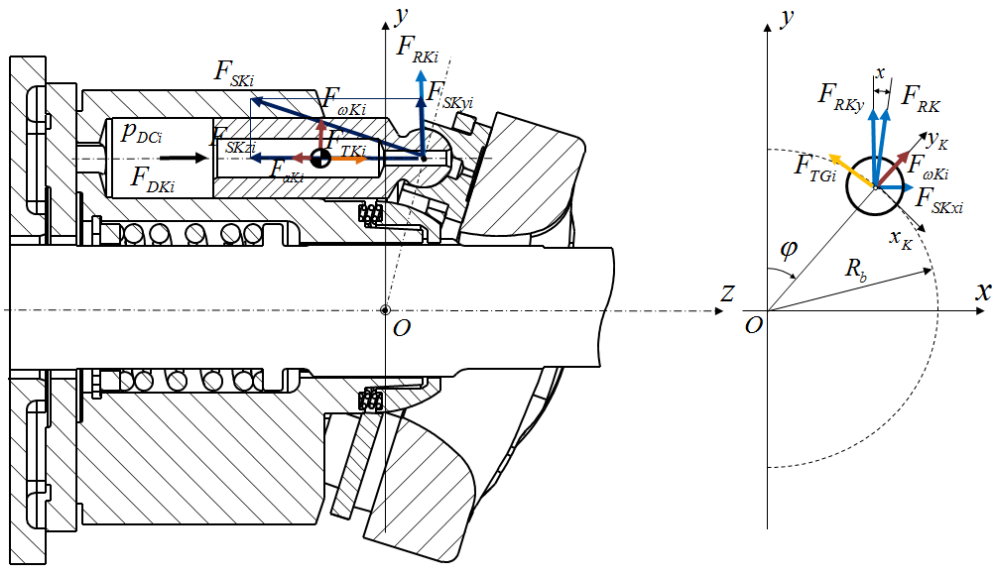

Figure 2.4. Piston/slipper assembly free body diagram.

The main force acting on the piston/slipper assembly is due to the pressurized fluid in the displacement chamber, F_{DK}, pushes the bottom of the piston in direction of the swash plate. The force due to the inertia of the piston/slipper assembly acts on the z-axis, $F_{aK;}$ and finally the force due to the friction between the piston and the cylinder bore also acts in the z-axis, F_{TK}. This last force, F_{TK}, has the same magnitude as F_{TB} but has opposite sign. The total sum of these forces, F_{DK}, F_{aK}, and F_{TK}, has to be reacted by the swash plate. Finally, the reaction force F_{SK} of the swash plate is acting on the piston/slipper assembly. More forces have an impact on the piston/slipper assembly; such as: the viscous friction between the slipper and swash plate on the local x_K direction as shown in Figure 2.4, F_{TG}; and the body force due to centripetal acceleration, $F_{\omega K}$. The latter force is the same force as the one represented in the Figure 2.3 by $F_{\omega B}$. The forces related to the piston/slipper assembly are all transmitted to the block summed into a resultant side force, $F_{RK,}$ which is the same force represented for a single piston on Figure 2.3 as F_{RBi}. This force can be defined as follows:

$$F_{RBx_i} = F_{\omega K_i} \sin\varphi - F_{TG_i} \cos\varphi \,. \tag{2.14}$$

$$F_{RBx_i} = F_{SK_i} + F_{\omega K_i} \cos\varphi + F_{TG_i} \sin\varphi \,. \tag{2.15}$$

The resulting forces and moments on the cylinder block can be expressed as follows:

$$F_{BZ} = F_{FB} + \sum_{i=1}^{z} F_{DBi} + \sum_{i=1}^{z} F_{TBzi} \,. \tag{2.16}$$

$$M_{Bx} = \sum_{i=1}^{z} y_i F_{DBi} + \sum_{i=1}^{z} y_i F_{TBzi} - \sum_{i=1}^{z} z_i F_{RByi} \,. \tag{2.17}$$

$$M_{By} = -\sum_{i=1}^{z} x_i F_{DBi} - \sum_{i=1}^{z} x_i F_{TBzi} + \sum_{i=1}^{z} z_i F_{RBxi} \,. \tag{2.18}$$

The external forces and moments Eq. (2.16), (2.17), and (2.18) need to be balanced by the forces and moments generated by the fluid film pressure field:

$$F_{fB} = \int_{sCB} pda \,. \tag{2.19}$$

$$M_{fx} = \int_{sCB} pyda \,. \tag{2.20}$$

$$M_{fy} = -\int_{sCB} pxda \,. \tag{2.21}$$

2.5 Cylinder Block/Valve Plate Interface Fluid Film Geometry

For the analysis of the performance of the fluid film in the cylinder block/valve plate interface it is necessary to define the fluid film geometry. A cylinder block and valve plate are shown in the Figure 2.5. This figure shows a design where both solids have a flat surface.

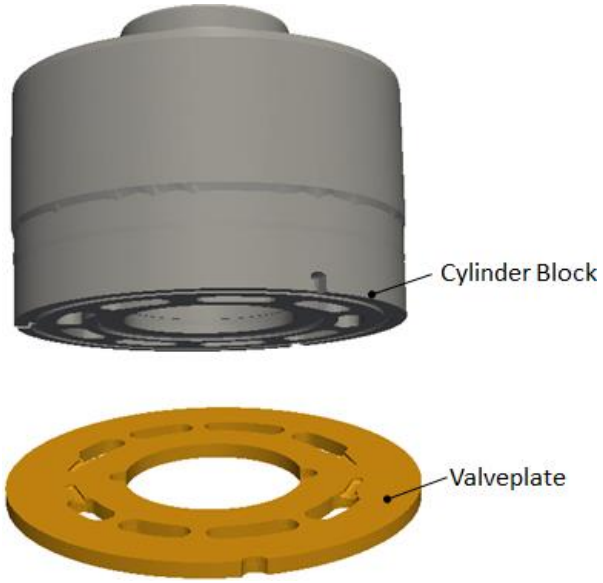

Figure 2.5. Cylinder block and valve plate.

In the case of a rigid model, i.e. without consideration of solid bodies, the fluid film geometry is described solely by the relative position of the cylinder block with respect to the valve plate. This is represented in Figure 2.6, where

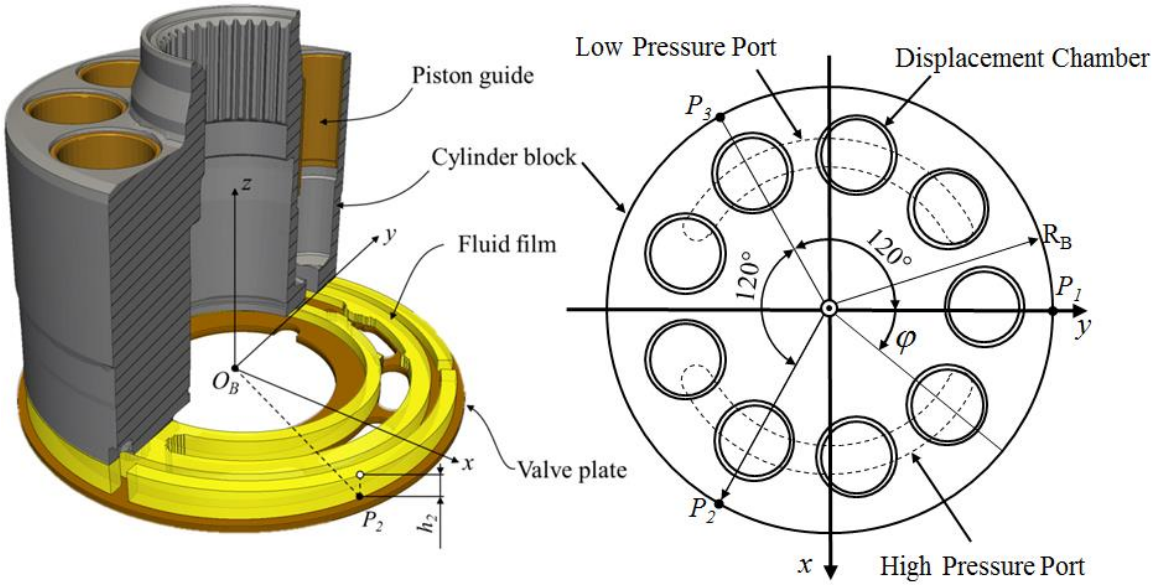

Figure 2.6. Fluid film geometry.

The local coordinate system's origin, O_B, is located in the intersection of the valve plate's running surface plane and the shaft axis, with the z-axis pointing towards the swash plate and the y-axis is pointing in the direction of the outer dead center of the machine, the x-axis is pointed towards the high pressure port of the machine. The fluid film geometry can be described in any point P by the position of the cylinder block with three control points P_1, P_2, and P_3, with respect to the valve plate surface (plane z=0). The geometry can be described as expressed by Eq. (2.22) as in Wieczorek and Ivantysynova (2002).

$$h(r,\varphi) = \frac{1}{\sqrt{3}R_B} r\sin\varphi(h_{P_2} - h_{P_3}) + \\ + \frac{1}{3R_B} r\cos\varphi(2h_{P_1} - h_{P_2} - h_{P_3}) + \frac{1}{3}(h_{P_1} + h_{P_2} + h_{P_3}) \quad (2.22)$$

In case of considering, surface deformation due to pressure and thermal loading, as well as surface shaping (2.21) need to be modified in order to determine the film geometry. In order to capture the different possible designs, wear-in profiles and elastic deformations the fluid film is expressed as follows (Zecchi and Ivantysynova, 2013).

$$h_{CB}(r,\varphi)=\frac{1}{\sqrt{3}R_B}r\sin\varphi(h_{P_2}-h_{P_3})+ \\ +\frac{1}{3R_B}r\cos\varphi(2h_{P_1}-h_{P_2}-h_{P_3})+\frac{1}{3}(h_{P_1}+h_{P_2}+h_{P_3})+\delta h_{CB}(r,\varphi) \quad (2.23)$$

$$h_{VP}(r,\vartheta)=\delta h_{VP}(r,\vartheta)\,. \quad (2.24)$$

In Eq. (2.23) and (2.24) the terms $\delta h_{CB}(r,\vartheta)$ and $\delta h_{VP}(r,\vartheta)$ were added to incorporate any elastic deformations due to pressure or thermal effects, and if desired micro-surface shaping. A representation of this is shown in were all the deformations and inclinations have been exaggerated for illustration purposes.

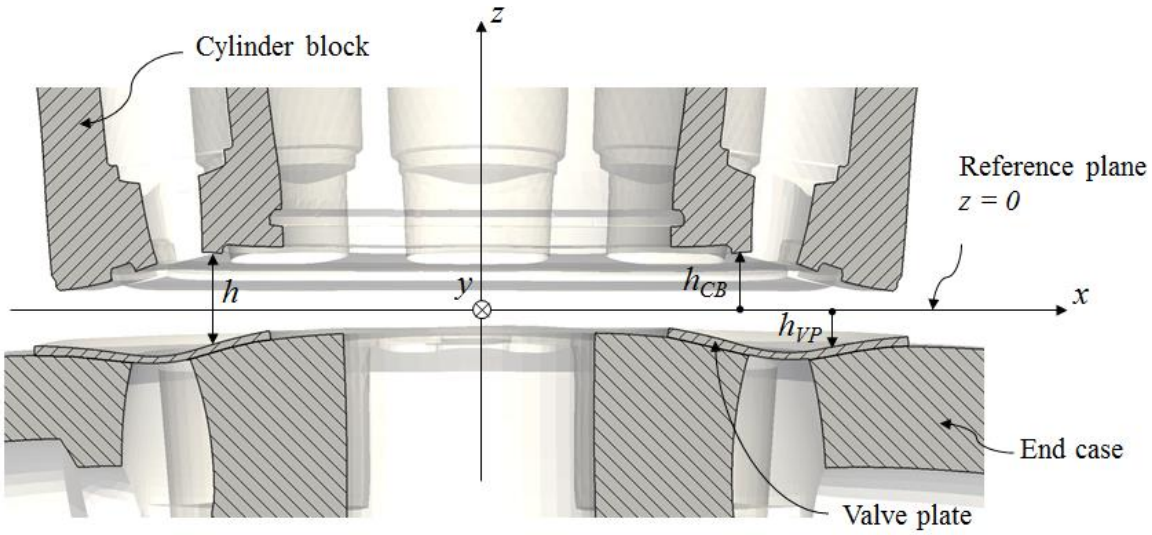

Figure 2.7. Fluid film geometry with elastic deformations (Zecchi, 2013).

The fluid film thickness at any point can be expressed by putting together Eq. (2.23) and (2.24) as follows, see (Zecchi and Ivantysynova, 2013):

$$h(r,\varphi)=\frac{1}{\sqrt{3}R_B}r\sin\varphi(h_{P_2}-h_{P_3})+ \\ +\frac{1}{3R_B}r\cos\varphi(2h_{P_1}-h_{P_2}-h_{P_3})+\frac{1}{3}(h_{P_1}+h_{P_2}+h_{P_3})+\,. \\ +(\delta h_{CB}(r,\varphi)-\delta h_{VP}(r,\varphi)) \quad (2.25)$$

The cylinder block's squeeze motion can be described by the time derivative of the fluid film height as in Eq. (2.26).

$$\dot{h}(r,\vartheta) = \frac{1}{\sqrt{3}R_B} r \sin\varphi(\dot{h}_{P_2} - \dot{h}_{P_3}) + \\ + \frac{1}{3R_B} r\cos\varphi(2\dot{h}_{P_1} - \dot{h}_{P_2} - \dot{h}_{P_3}) + \frac{1}{3}(\dot{h}_{P_1} + \dot{h}_{P_2} + \dot{h}_{P_3}) + . \\ +(\delta\dot{h}_{CB}(r,\vartheta) - \delta\dot{h}_{VP}(r,\vartheta)) \tag{2.26}$$

CHAPTER 3. NUMERICAL MODELS

3.1 Overview of the Numerical Models

In this section various numerical models that were utilized in the work done for this thesis are described. The models that were utilized in this simulation-based investigation were: a lumped parameter approach to calculate the instantaneous pressure in the displacement chamber, an influence matrix generator, and an in-house fluid structure thermal interaction model for the cylinder block/valve plate interface.

3.2 Instantaneous Pressure in the Displacement Chamber

The instantaneous pressure in each displacement chamber is a fundamental parameter in axial piston machines for the correct calculation of the forces exerted on the cylinder block. The instantaneous pressure in the displacement chamber changes continuously over one shaft revolution and it's therefore a function of time; nevertheless, it can be assumed that the pressure is uniform in the entire displacement chamber. A lumped parameter approach can be applied.

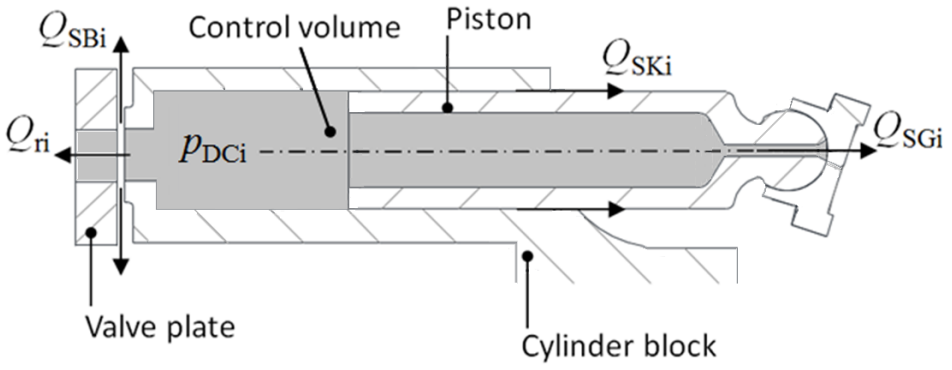

Figure 3.1. Instantaneous pressure calculation control volume.

The pressure build-up equation can be written as:

$$\frac{dp_{DCi}}{dt} = \frac{K}{V_i}(Q_{ri} + Q_{SKi} + Q_{SBi} + Q_{SGi} - \frac{dV}{dt}) . \quad (3.1)$$

In Eq. (3.1), the left hand side is the derivative of the pressure over time, on the right hand side K is the bulk modulus, V is the fluid volume and dV/dt is its derivative over time; the various Q terms are the flow in and out of the volume, as illustrated in Figure 3.1. Each flow is by convention positive when it enters in the control volume, since this would force the pressure to increase. The flow Q_{ri} is the main flow through the volume while the other flows labeled with Q_S are the corresponding leakages through the three lubricating gaps: the flow through the slipper/swash plate interface, Q_{SGi}; the flow through the piston/cylinder interface, Q_{SKi}; and finally, the flow through the cylinder block/valve plate interface, Q_{SBi}.

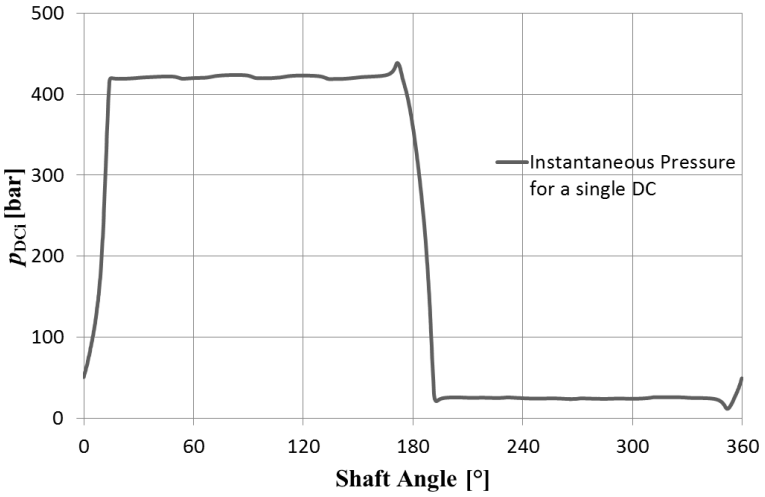

Figure 3.2. Instantaneous pressure in a single displacement chamber.

An example of the instantaneous pressure for a single displacement chamber is illustrated in the following Figure, for a 130 cc/rev unit in pumping mode at an operating condition of 3200 rpm, a pressure differential of 420 bar and full displacement. In the first 180° of the shaft revolution we can observe the delivery stroke of the piston as the pressure is built up over the first few degrees, and then we can observe the pressure pulsations due to the changing number of piston that are on the delivery stroke as they transition from one stroke to the next one. For more information on the lumped parameter approach to

calculate p_{DCi} please refer to previous work done by Wieczorek and Ivantysynova (2002), Seeniraj (2009), and Klop (2010).

3.3 Fluid Structure Thermal Interaction Model

3.3.1 Overview of the Model

The numerical model utilized to predict the behavior of the fluid film is a novel fluid structure thermal interaction model specifically designed for the prediction and calculation of the behavior of the lubricating gap in the cylinder block/valve plate interface; it was developed by Zecchi (2012). The model assumes full fluid film lubrication and accounts for all the machine kinematics, deformation of surfaces of the solids due to pressure and thermal loading, and micro-motion of the parts. It also calculates the power losses in the lubricating gap due to leakage flow and viscous friction. The model is composed of four main modules. The first one and most important is the gap flow module, where the Reynolds and the energy equation are solved. Second, an in-house linear FEM module that solves for the elastic deformation due to the pressure field in the lubricating gap. Third, a finite volume module that solves for the temperature distribution in the 3D volume of the solids. Finally, another FEM module solves for the elastic deformation due to the thermal stresses.

The Reynolds equation is solved to calculate the pressure field in the gap. The energy equation is solved to obtain the temperature distribution in the gap and additionally the heat flux towards the solid body surfaces. Both pressure and temperature have an impact in the fluid properties due to the high dependence to the pressure and temperature. These are used to update the fluid properties in the gap. The pressure field is fed into another module, an in-house linear FEM module, which using the linear superimposition principle using influence matrixes calculates for the elastic deformation due to pressure in the gap. The deflection of the bodies is then fed back into the gap flow module to update the fluid film geometry; this is done with every angle of rotation. Additionally, the heat flux calculated every degree step, in the gap module, is then used in the finite volume module to calculate the temperature in the solid bodies every revolution. Furthermore,

this temperature is then used to calculate the thermal stresses in the body. These are then fed to a second FEM module similar to the first to calculate the elastic deformations due to thermal effects. The elastic deformations due to thermal effects are fed back into the gap flow module to update the geometry of the fluid film. This process repeats until a steady state convergence is achieved. A general overview of the structure of the model is illustrated in the Figure 3.3:

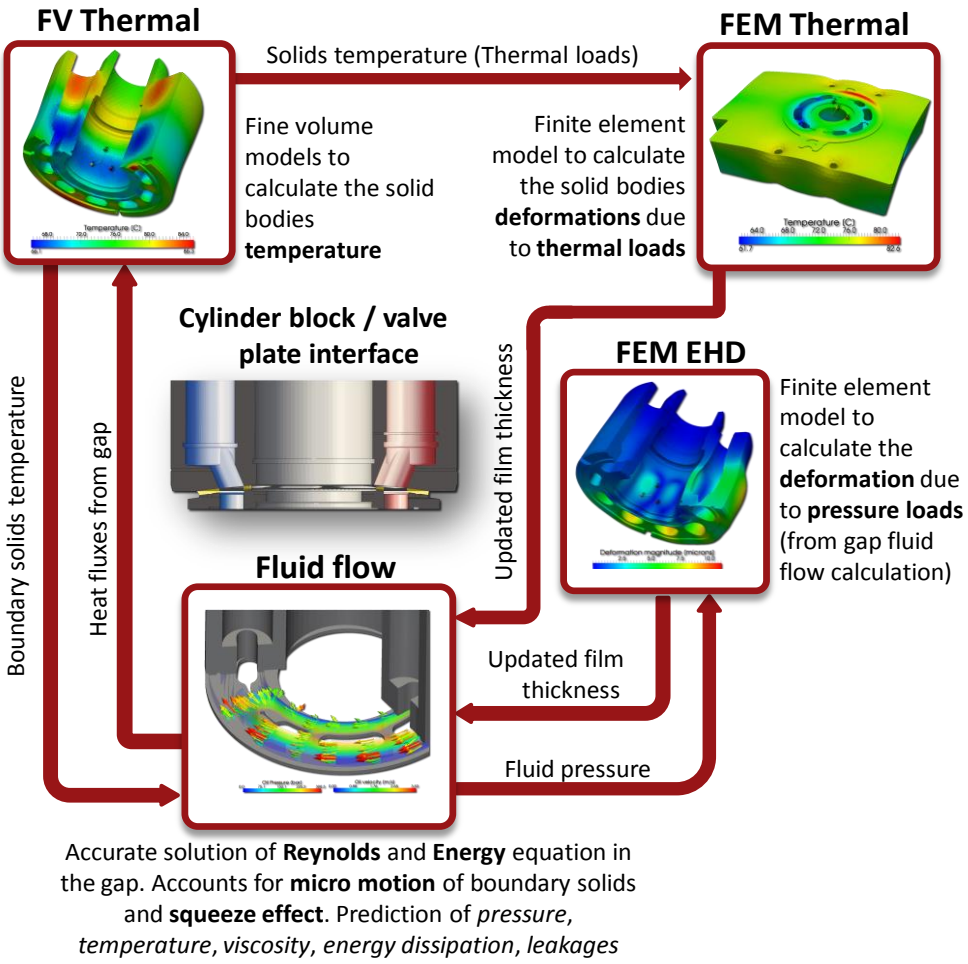

Figure 3.3. Fluid structure thermal interaction model (Zecchi, 2012).

3.3.1.1 Work Flow

In this section a more in-depth description of the general work flow of the fluid structure thermal interaction model is given. The general work flow can be observed on the block

diagram in Figure 3.4. The model begins with some initial value and goes in into the force balance loop, where it calculates the pressure in the fluid film gap by solving the Reynolds equation and it then calculates the external forces exerted by the kinematics of the machine. The model assumes full fluid film lubrication, so then the model checks for balance of forces between the external loads and the fluid forces in the gap, this is never the case on the first iteration, a multidimensional root finding Powell's method is utilized to search for a different squeeze velocity that will aid in balancing the loads through generating more or less pressure through the squeeze motion. This goes on until some convergence is achieved or a maximum number of iterations have been completed.

After the force balance loop, the model advances to the fluid structure interaction loop (EHD Convergence loop). The model uses the final pressure field obtained in the force balance loop and the influence matrices to calculate the elastic deformation of the solid bodies; the valve plate/end case assembly and the cylinder block. These elastic deformations are then used to update the fluid film geometry and a simple form of the Reynolds equation is solved. The solution of the Reynolds equation is very sensitive to the geometry of the fluid film so the solution will return a different fluid film which also corresponds to a different elastic deformation of the solid bodies. An under relaxed pressure field is utilized with a dynamic relaxation technique to avoid divergence. The model then solves the energy equation; calculates the gap temperature distribution and calculates the heat fluxes to the solid bodies.

Both the pressure and the temperature are used to update the fluid properties. The squeeze velocity is used to update the new position of the cylinder block for the next time step, one degree of rotation. The model advances one time step (one degree of a revolution). If a whole revolution hasn't been completed the model goes through the force balance and the fluid structure interaction loops again.
At the end of a revolution, the thermal analysis is conducted in the finite volume method module; where the temperatures in the solid bodies are calculated. Later, the elastic deformations are calculated using the other FEM module. The new elastic deformations

and temperature distribution in the solid bodies is fed back into the gap module; starting with the force balance loop and following the fluid structure interaction loop. This process goes on for several iterations until the whole simulation has reached convergence.

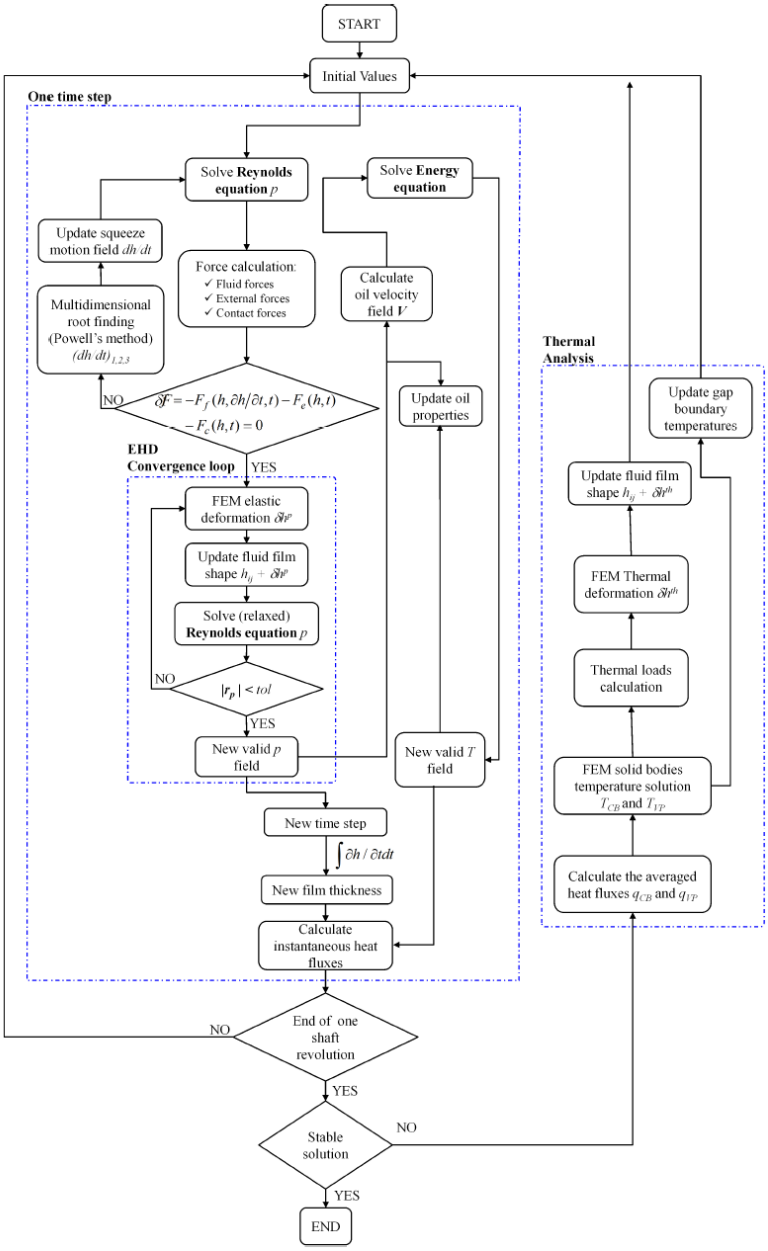

Figure 3.4. Work flow of the model (Zecchi, 2013).

Further details of the different schemes represented in the block diagram in Figure 3.4 can be found in Zecchi (2013).

3.4 The Gap Module

In this section, the finite volume method module is used to solve a non-isothermal fluid flow which is governed by both the Reynolds and the energy equation is described. This module calculates the pressure and temperature distribution in the lubricating fluid film. These parameters are crucial for the correct prediction of the performance of the cylinder block/valve plate interface.

3.4.1.1 The Reynolds Equation

First, the Reynolds equation is derived from two main equations: the Navier-Stokes equation and the Continuity equation. The final derivation of the Reynolds equation as in Zecchi and Ivantysynova (2013):

$$\frac{1}{r}\frac{\partial}{\partial r}\left(-\frac{\rho h^3}{12\mu}r\frac{\partial p}{\partial r}\right)+\frac{1}{r}\frac{\partial}{\partial \varphi}\left(-\frac{\rho h^3}{12\mu}r\frac{\partial p}{\partial \varphi}\right)=\omega\left(\rho\frac{\partial h_{CB}}{\partial \varphi}-\frac{1}{2}\frac{\partial(\rho h)}{\partial \varphi}\right)-\rho\frac{\partial h}{\partial t}. \tag{3.2}$$

On the left hand side of the equation model the hydrostatic component through the diffusion from the boundaries. The terms on the right hand side are the source in the Reynolds equation they include the physical wedge, the translational squeeze and the normal squeeze component.

3.4.1.2 The Energy Equation

The energy equation is solved to obtain the temperature distribution of the fluid film between the cylinder block and the valve plate; the temperature determines the fluid physical properties; i.e. density, viscosity, bulk modulus, etc. Additionally, the energy equation defines the heat flux that is transmitted to the solid bodies from the fluid film. The energy equation can be expressed as follows as in Zecchi (2013):

$$\nabla\cdot\left(\rho\mathrm{V}T-\frac{\lambda}{c_p}\nabla T\right)=\frac{\mu}{c_p}\Phi_d. \tag{3.3}$$

The Eq. (3.3) contains the source term Φ_d, which is the mechanical dissipation function. It expresses the heat power generated per volume unit due to the viscous shear of the

fluid in the thin fluid film. It is assumed that all the work to change the fluid element shape at constant volume is all converted to heat. It can be expressed by Eq.(3.4).

$$\Phi_d = \left(\frac{\partial u}{\partial z}\right)^2 + \left(\frac{\partial v}{\partial z}\right)^2 + \frac{4}{3}\left(\frac{u}{r}\right)^2 + \left(\frac{v}{r}\right)^2 . \tag{3.4}$$

For the full derivation of Eq.(3.4) please refer to Zecchi (2013).

3.4.1.3 Calculation of the Total Energy Dissipation

The mechanical dissipation function, described by Eq. (3.4), expresses the amount of power per unit volume that is dissipated into heat in the fluid flow; therefore the integration of Eq. (3.4) throughout the volume V of clearance determines the total power dissipated

$$P_l = \int_V \Phi_d dv . \tag{3.5}$$

Eq. (3.5) also includes the power loss due to leakage flow. The mechanical energy in the pressurized fluid is dissipated into heat, when it leaks through the gap. The leakage flow can be calculated by integrating the velocity field of the film at the lateral boundaries. The velocity is expressed in Eq. (3.4).

$$\begin{cases} u = \dfrac{1}{2\mu}\dfrac{\partial p}{\partial r}[z^2 - z(h_{CB} + h_{VP}) + h_{CB}h_{VP}] \\ v = \dfrac{1}{2\mu}\dfrac{\partial p}{\partial \varphi}[z^2 - z(h_{CB} + h_{VP}) + h_{CB}h_{VP}] + \omega r\left(\dfrac{z - h_{VP}}{h}\right) \end{cases} . \tag{3.6}$$

In Eq.(3.6) u and v represent the radial and circumferential components, respectively. Most of the leakage in the cylinder block/valve plate interface comes from u, the radial component, due to the Poiseuille flow. The power loss related to the leakage can be calculated, as shown in

$$P_{l,s} = Q_{SB}\Delta p . \tag{3.7}$$

The mechanical loss can be calculated as the difference of the total power dissipated Eq.(3.6) and the leakage loss Eq. (3.7).

3.5 Mesh Generation

Two main types of meshes were used in the numerical models: the fluid mesh, used to solve the Reynolds and energy equation in the gap; and the solid mesh, used to calculate the temperature distribution of the bodies and to generate the influence matrices.

3.5.1 Fluid Mesh

The fluid mesh as mentioned previously was used to solve the Reynolds and energy equation. The correct definition of the mesh is important since the precision of the model depends on it. The generation of the fluid mesh represents a complex problem, since the geometry of the fluid film is defined by two different geometries: the cylinder block sealing surface and the valve plate running surface. Additionally, the geometry of the fluid film which is in contact with the solids is constantly changing over one shaft revolution due to the nature of the kinematics of the machine. As the cylinder block rotates over the valve plate, the geometry is changing as the displacement chamber openings keep rotating around the shaft axis. An example of the fluid domain for each solid is shown Figure 3.5; the intersection of the domain in both surfaces defines the fluid film computational domain. The definition of these areas is achieved via the use of CAD files in the STL format.

As shown in Figure 3.5, the grid size is too coarse to correctly define the fluid film domain. The solution, when calculating the force due to the pressure field in the gap, is to interpolate the pressure to a different grid which covers exactly the interface's area. As shown in the figure below:

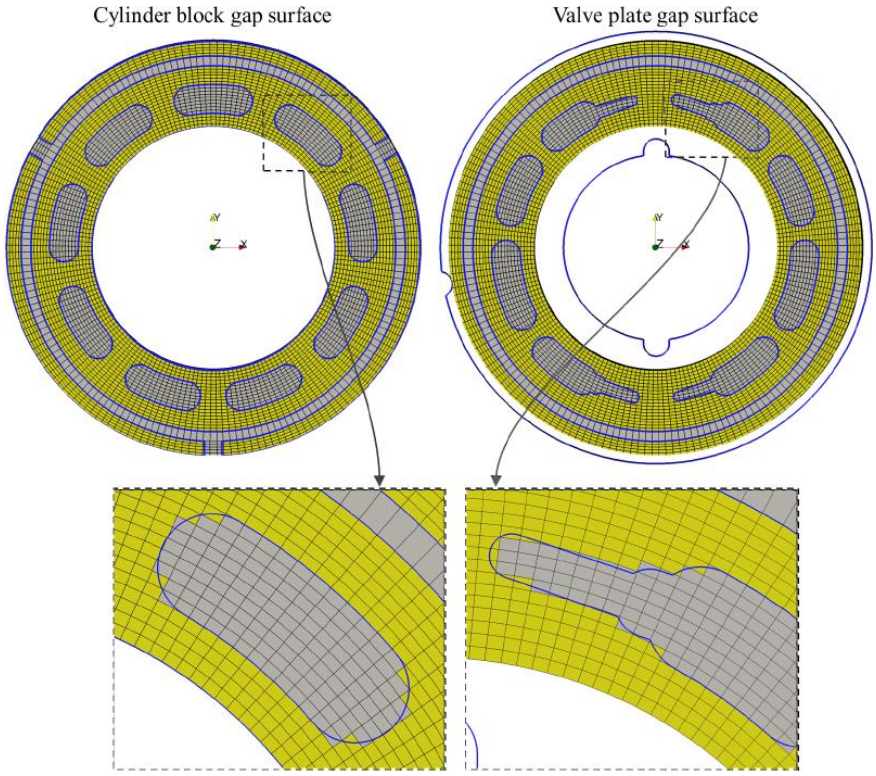

Figure 3.5. Fluid mesh grid, on the left the cylinder block's fluid domain is shown in yellow on the right the valve plate's fluid domain (Zecchi, 2013).

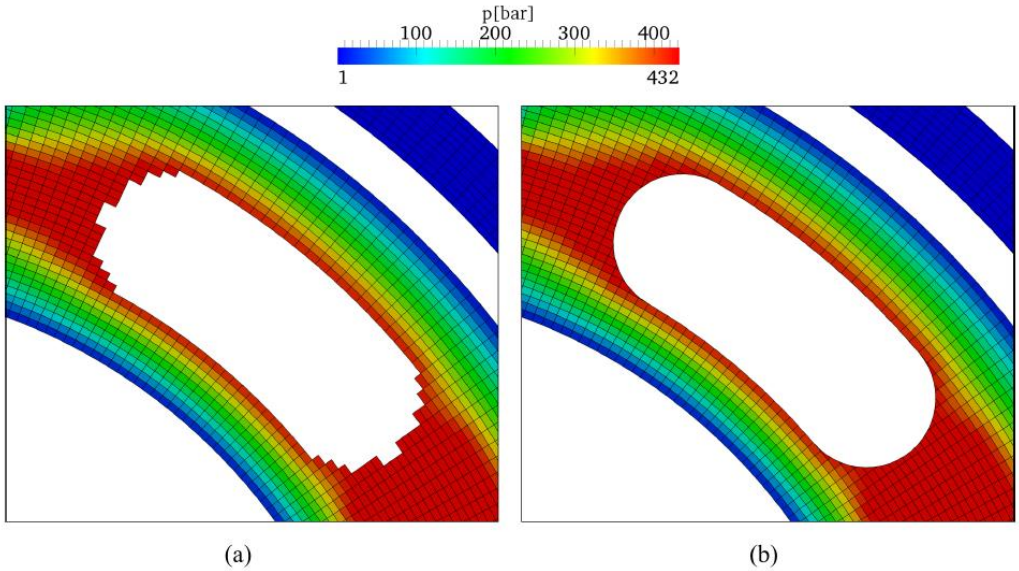

Figure 3.6. Fluid mesh with pressure representation on the left (a), interpolated pressure field to grid covering the fluid film area on the right (b) (Zecchi, 2013).

3.5.2 Solid Mesh & Influence Matrix Generation

The solid mesh also represents an important input to the numerical model. It is used to generate the influence matrices which are then used to calculate online the deformation due to pressure; and also used to calculate the temperature in the solid bodies. For the generation of the solid meshes, commercial software HyperMesh Altair was utilized. Simple tri-elements for the 2D elements were used to define the surfaces. Tetrahedrons were used for the 3D elements due to their simplicity it made it easier to mesh the solids. Example of a 3D mesh shown in

Figure 3.7. Solid mesh for the cylinder block.

As mentioned this mesh is utilized to generate the influence matrices necessary to calculate the elastic deformation due to pressure on the fluid structure interaction model. Each of the faces that form part of the sealing gap, on the cylinder block or the valve plate, is loaded with a reference pressure of 100 bar including the displacement chambers, and suction and delivery ports. There are two possible options for the physical constraint of the solid body; fixed constraint, or inertia relief. The deformation for all the 3D tetrahedral elements is calculated but only the deformation in the z-direction of the elements conforming the sealing land are stored and save in an influence matrix. Later, when in the fluid structure interaction loop, these influence matrices are used to calculate the deformation of the sealing surface of the solid body by an off-line calculation method based on the superimposition principle and defines the deformation of the solid parts

through a certain number of influence matrices. An example of the influence matrices generated is shown in the following Figure 3.8. The deformation in the lubricating gap is shown for two cases, on the left a reference pressure is applied to a single face that composes the sealing surface of the lubricating gap, and on the right the deformation due to a reference pressure applied in the displacement chamber.

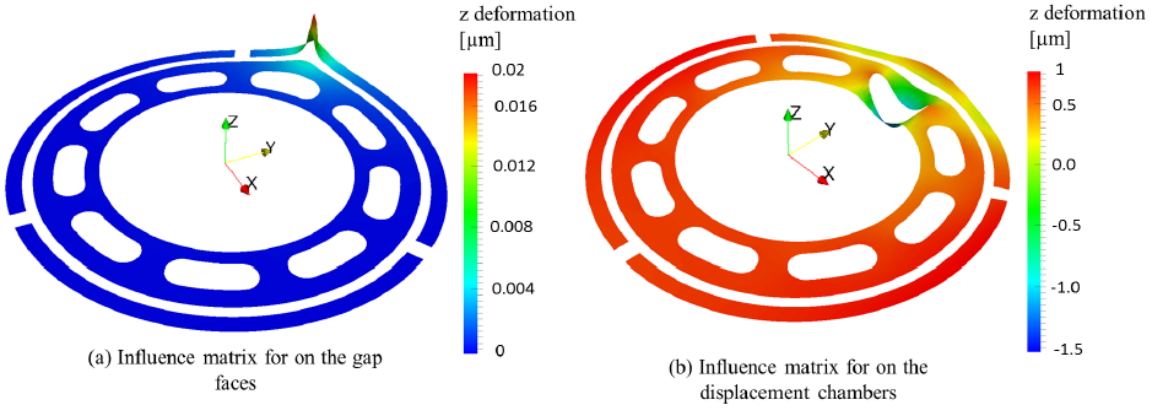

(a) Influence matrix for on the gap faces

(b) Influence matrix for on the displacement chambers

Figure 3.8. Deformation due to the reference pressure of 100 bar applied on an element face on the sealing land (a) and in one of the displacement chambers (b) (Zecchi, 2013).

CHAPTER 4. INVESTIGATION OF SURFACE SHAPING

In this section, the parameters and operating conditions for the simulation-based investigation are described. Some of these are the geometry definition of the sinusoidal wave, the selected operating conditions, and some boundary conditions.

4.1 Sinusoidal Wave Geometry

A micro-surface shaping of the running surface of the valve plate is proposed in this work. The sinusoidal wave is introduced in the circumferential direction of the valve plate. The following figure defines the coordinate system that is used in to define the waved surface.

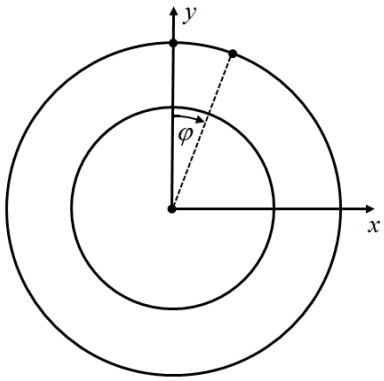

Figure 4.1. Coordinate system used to define micro-shaping.

The wave has three main parameters that define its geometry:

1. Amplitude: The amplitude is self-explanatory; it is the amplitude of the sine wave. This is illustrated in Figure 4.2

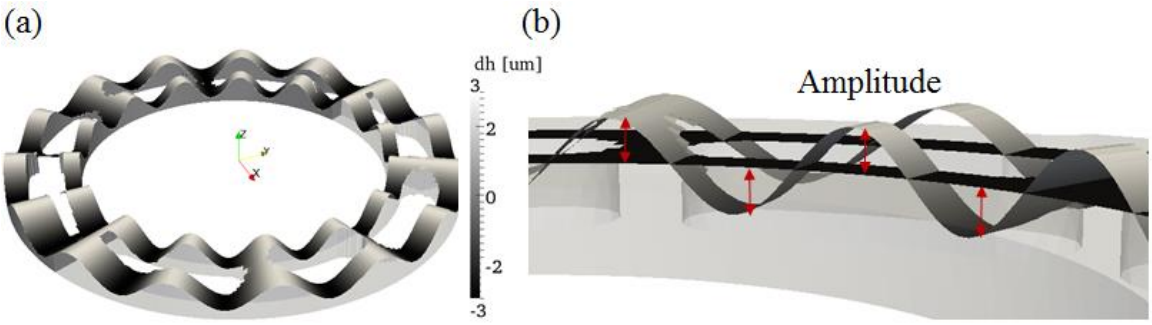

Figure 4.2. Waved surface of valve plate (Scaled x1000) (a); amplitude of sinusoidal wave on (B) (Amplitude = 3 μm).

2. Frequency: The frequency refers to the number of waves in the circumferential direction.
3. Offset: The offset defines the starting point of the wave in the valve plate. In previous research (Baker, 2008; Zecchi, 2012) the sine wave always started at the outer dead point (φ=0°). When the offset is set to be 0° this means the wave will start on the point P_1 represented in Figure 2.5Figure 4.3.

The surface geometry of the valve plate is defined, as follows:

$$\delta h_{VP} = A \cdot \sin(f(\varphi + offset)) . \tag{4.1}$$

One more example of the waved pattern on the valve plate is shown on the following Figure, where a view from the top (top) and a lateral view on the (bottom).

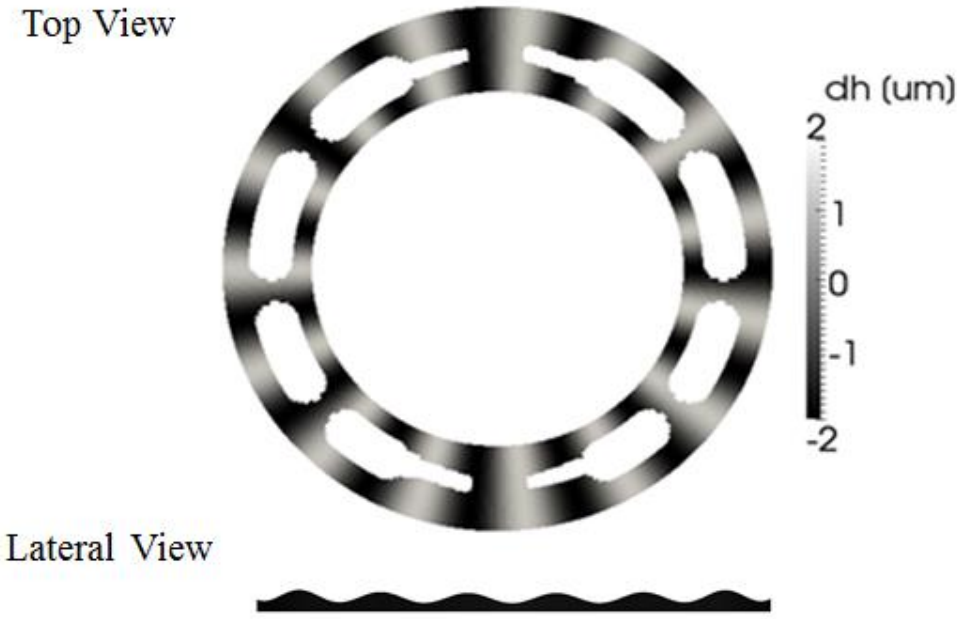

Figure 4.3. Waved pattern on valve plate, 2μm amplitude, frequency of 15 waves and offset of 9°.

4.2 Waved Profiles Selected

For this work, various designs were selected to identify the potentials of the micro-surface shaping. Moreover, in order to be able to study the effects of the design parameters the simulations were run using different combinations of the parameters. The amplitude was varied from 1-4 μm with a step of 1 μm. The frequency was varied from 10 to 30 in steps of 5. Finally, the offset was varied in percentage; a full sinusoidal wave is of different length in degrees depending on the frequency; i.e. for a frequency of 10 a full sinusoidal wave occurs in 36° (an offset of 18° would be corresponding to a 50%) whereas for a frequency 15 the sinusoidal wave occurs in only 24° (an offset of 12° corresponds to a 50%). The offset was varied from 0-75% in steps of 25%.

A list of the various waved surface selected for the simulation-based investigation are shown in Table 4.1.

Table 4.1. Waved surface parameter conditions.

Design No.	Amplitude [µm]	Offset [%]	Frequency [-]
1	1	0	10-30
2	1	25	10-30
3	1	50	10-30
4	1	75	10-30
5	2	0	10-30
6	2	25	10-30
7	2	50	10-30
8	2	75	10-30
9	3	0	10-30
10	3	25	10-30
11	3	50	10-30
12	3	75	10-30
13	4	0	10-30
14	4	25	10-30
15	4	50	10-30
16	4	75	10-30

4.3 Operating Conditions

In the simulation-based investigation a number of simulations were run using several selected operating parameters of the machine in pumping mode. The parameters that define the operating conditions considered in this work are the pressure differential in bar, Δp, rotational speed in rpm, n, and the machine's displacement, β, expressed as a percentage. These operating conditions are listed in Table 4.2. . The fluid selected for these simulations was hydraulic oil with viscosity grade 32.

Table 4.2. Operating conditions.

OC No.	Δp [bar]	n [rpm]	Tinlet [°C]	Toutlet [°C]	Tcase [°C]	β [%]
1	50	1000	52	54	60.5	20
2	50	1000	52	53	63	100
3	420	1000	52	66	85	20
4	420	1000	52	60.5	80	100
5	50	3200	52	54	81	20
6	50	3200	55	57	83	100
7	420	3200	52	65	87	20
8	420	3200	52	59	84	100

These operating conditions were selected since they are the most extreme operating conditions for a selected 130 cc/rev axial piston machine unit. The main objective of this investigation study how the load carrying ability of the cylinder block/valve plate interface can be improved while simultaneously reducing the energy dissipation through a micro-surface shaping. The operating conditions simulated are represented in Figure 4.4.

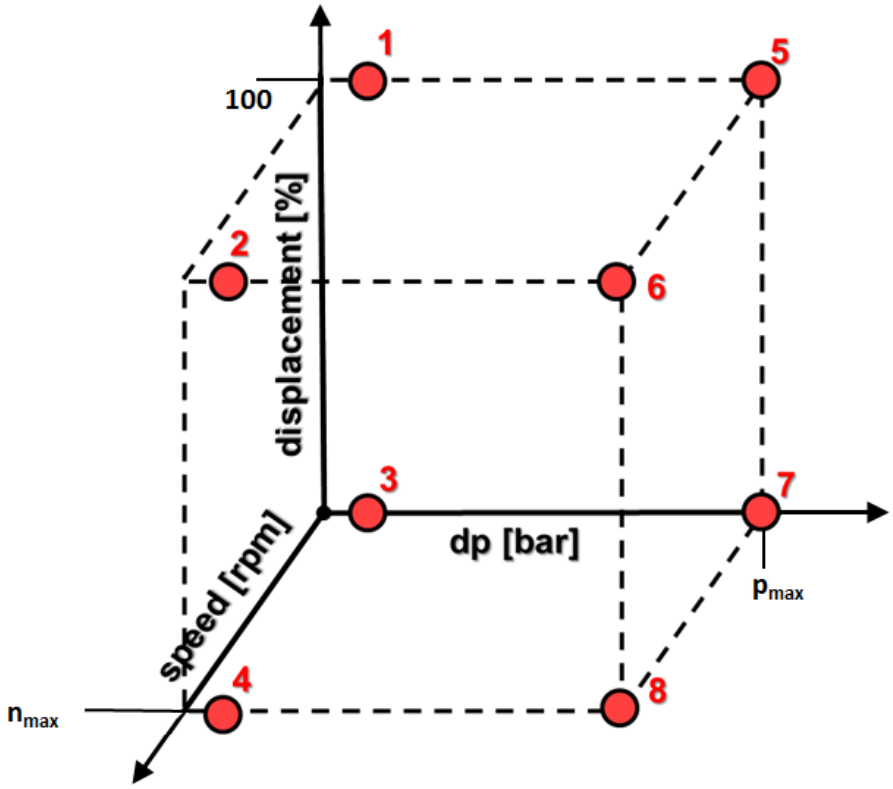

Figure 4.4. Operating conditions.

4.4 Boundary conditions

The numerical models described in Chapter 3 require many different boundary conditions. These different boundaries will be described in this section. Some of the boundaries that need to be defined are the ones needed to solve the Reynolds equation in the lubricating gap, others the boundary conditions for the elastic deformation analysis of the solid bodies; both for the thermal and pressure problem.

4.4.1 Gap Flow Boundary Conditions

In the gap flow module the pressure boundary conditions need to be defined correctly in order for the correct calculation and prediction of the behavior of the cylinder block/valve plate interface. This is due to the fact that the Reynolds equation represents a full Dirichlet problem, where the pressure boundaries have to be defined.

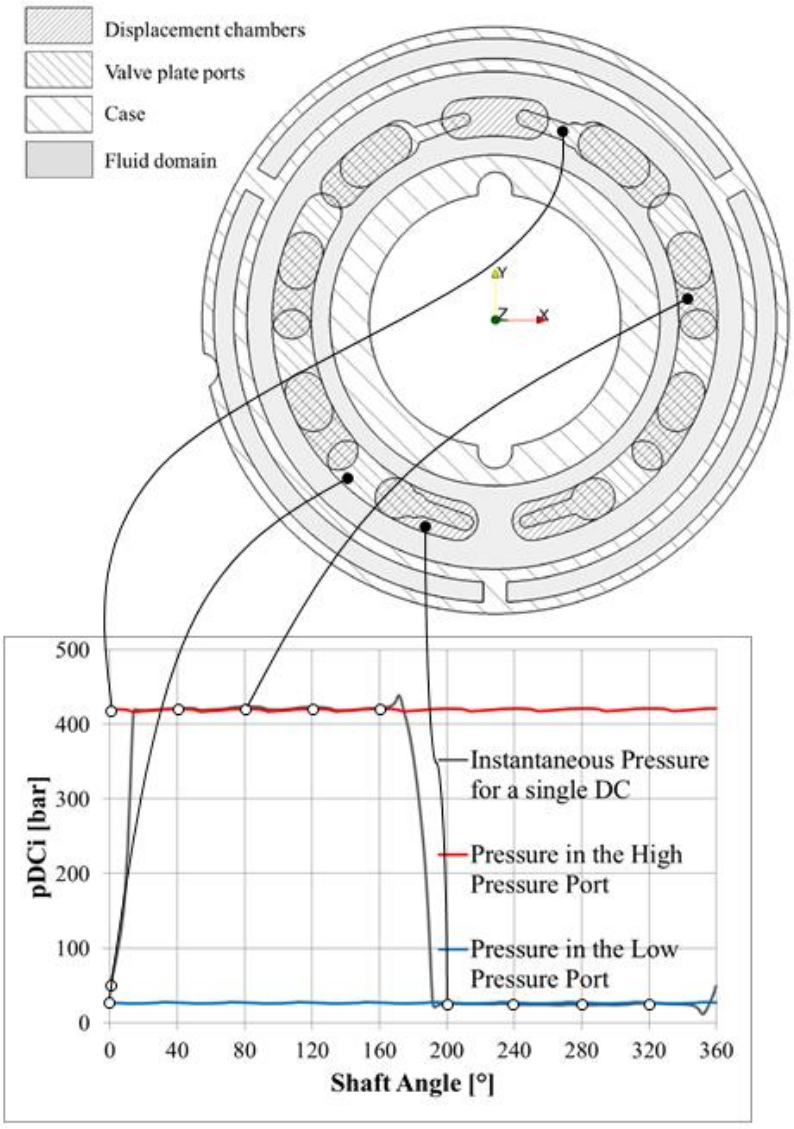

Figure 4.5. Pressure boundary conditions for the Reynolds equation (Zecchi, 2013).

4.4.2 Influence Matrix Boundary Conditions

Moreover, when generating the influence matrices for the elastic deformation due to pressure the pressure boundary conditions have to be defined in the 3D volumes defining the solid. An example of the pressure boundaries for the generation of the influence matrix is shown in Figure 4.6.

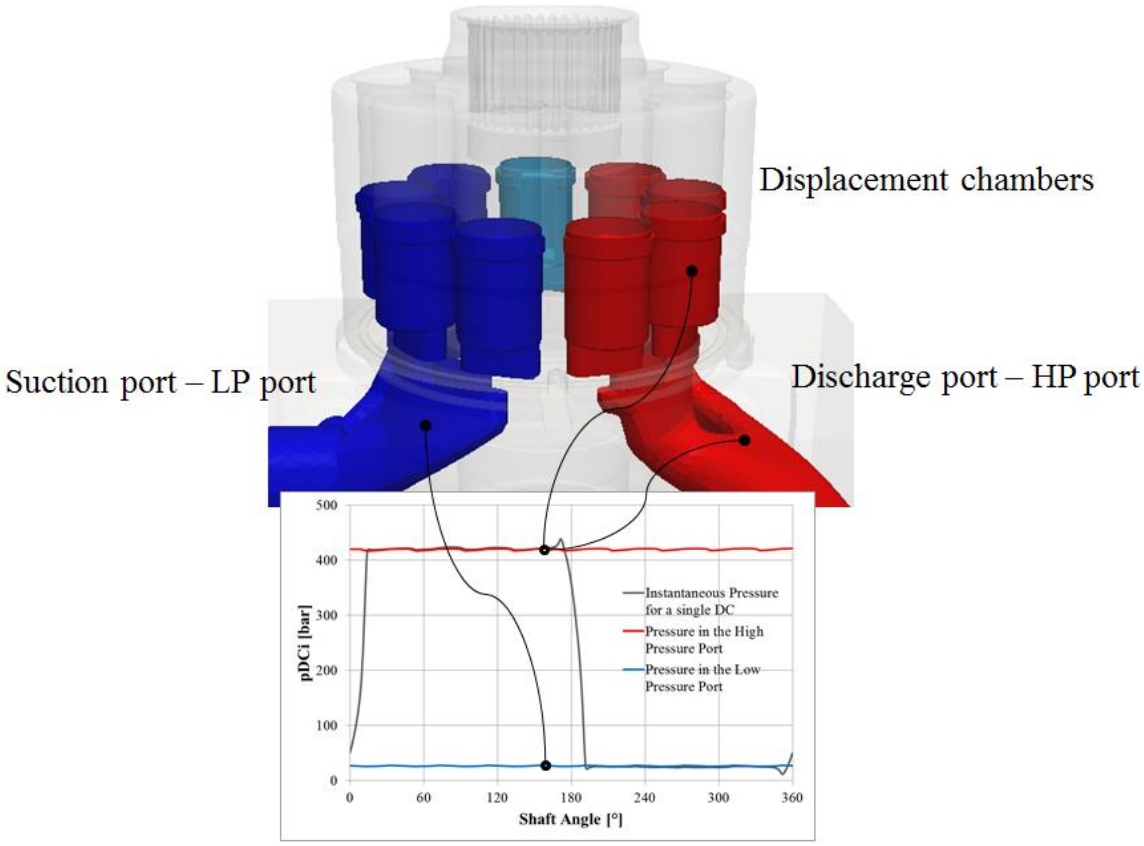

Figure 4.6. Pressure boundary conditions to define IMs.

4.4.3 Thermal Problem Boundary Conditions

The boundary conditions are of a high significance for the thermal problem as well. Since, this will determine to which surface faces to apply different conditions:

1. Constant temperature boundary condition (Dirichlet boundary): Utilized only when the boundary condition temperature is known. This boundary was not utilized in this investigation.
2. Mixed boundary condition: In this boundary condition a temperature and a convection coefficient at infinite are specified for this boundary condition. This is typically applied to all the external surfaces of the cylinder block, since we know the operating rotational speed and temperature, the convection coefficient can be estimated from literature or some CFD approach. (Pelosi, 2012; Zecchi, 2013)

3. Neumann boundary condition: The normal gradient of temperature at the boundary cell is given. The average heat flux is calculated from the energy dissipated in the gap clearance and applied to the surface in contact.(Pelosi, 2012)

In the following figure the boundary conditions that were used are represented. For more information on the calculation of the convection coefficient please refer to Zecchi (2013), since it is out of the scope of this work. Also the temperatures that were used together with the mixed boundary condition were taken from measurements.

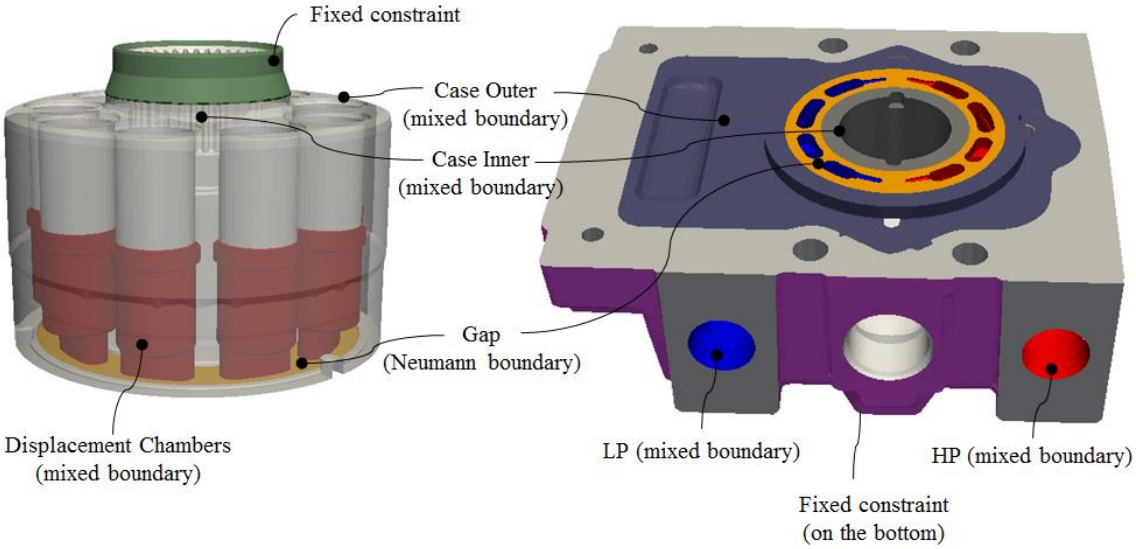

Figure 4.7. Thermal boundaries on the volume mesh.

CHAPTER 5. BASELINE SIMULATION RESULTS ANALYSIS

5.1 Cylinder Block/Valve Plate Interface: Analysis of Gap Flow Results

In this section, the simulation results for the standard design of 130 cc/rev unit in pumping mode are presented. The simulations were run for eight different selected operating conditions as described by Table 4.2. The results from these simulations will be shown and described in detail. In Figure 5.1, an example of the simulation results showing the fluid film thickness in the cylinder block/valve plate interface. The figure uses the same local coordinate described in section 2.5, where the fluid film geometry is described.

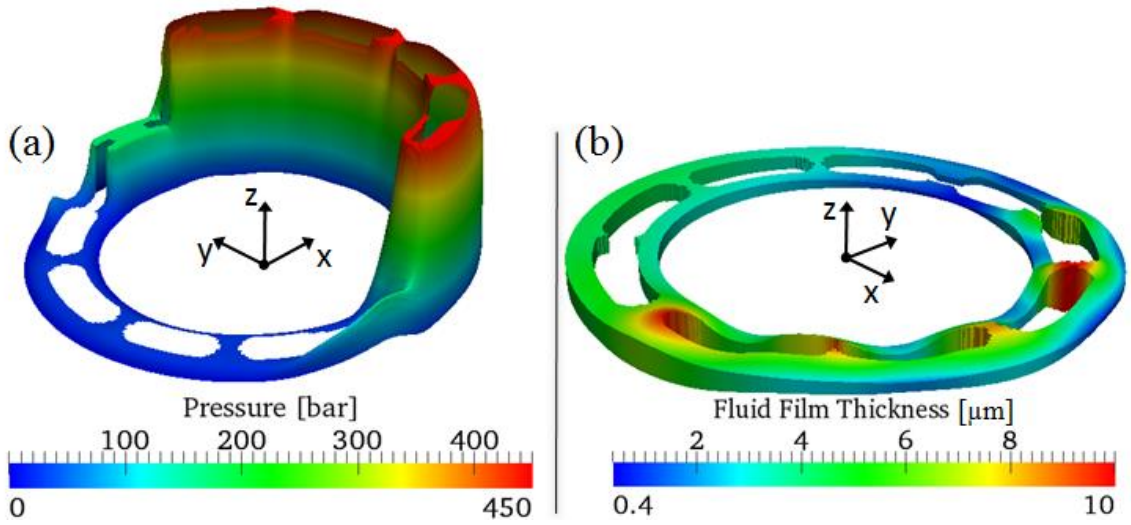

Figure 5.1. Example of the pressure field (a), and the fluid film thickness (b).

In Figure 5.2, simulation results shown are for operating conditions 1 and 2 defined in Table 4.2 (n = 1000 rpm, Δp=50 bar, β=20% and n = 1000 rpm, Δp=50 bar, β=100%, respectively). The low displacement results are shown on the top and full displacement results on the bottom. On the left, a 3D representation of the pressure is shown; and, on the right, the normalized fluid film thickness. The film thickness were normalized for all

presented results in thesis using time average of the maximum fluid film thickness of the baseline design.

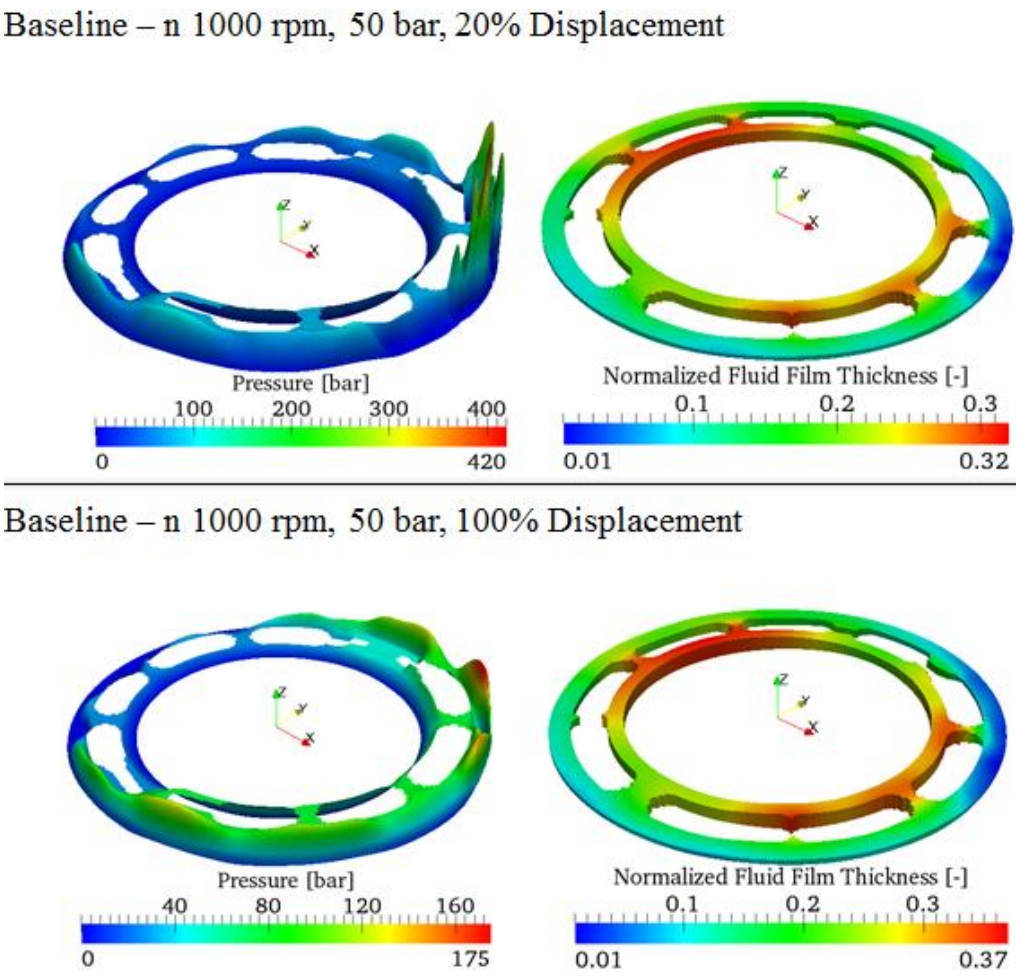

Figure 5.2. 3D Representation of the fluid film pressure (left) and thickness (right) for n=1000 rpm, Δp=50 bar, β=20% (top) and n=1000 rpm, Δp=50 bar, β=100% (bottom).

In Figure 5.2, shows the results obtained from the model. Full and low displacement operating condition results exhibit similar results in terms of pressure fields and fluid film thickness. It is observed that the fluid film has difficulties carrying the loads exerted on the cylinder block. The pressure distribution across the fluid film is represented; the pressure field is dominated by the hydrostatic pressure diffused into the gap from the displacement chambers and ports. Moreover, the pressure due to hydrodynamic effects comes mostly from the squeeze motion of the block. Extremely low fluid film thicknesses

are present on the high pressure side of operation of the interface, which corresponds to the high pressure side near the outer dead point. This can be well explained by the tipping moments trying to rotate the block in the positive direction of the x- and y- axis. The moment on the x-axis, M_{Bx}, is much larger in magnitude which is the reason of the lower fluid film thickness on the high pressure side.

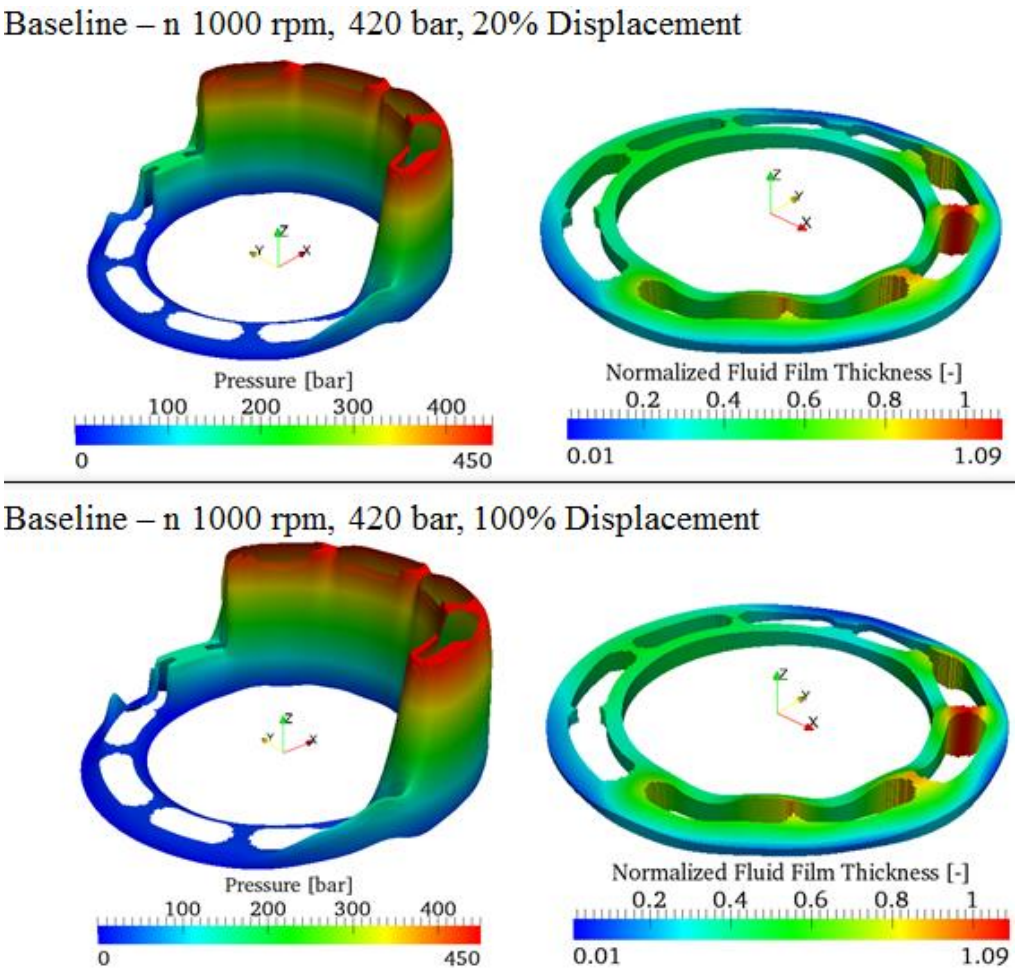

Figure 5.3. 3D Representation of the fluid film pressure (left) and thickness (right) for n=1000 rpm, Δp=420 bar, β=20% (top) and n=1000 rpm, Δp=420 bar, β=100% (bottom).

Figure 5.3 shows simulation results for operating conditions 3 and 4 (n = 1000 rpm, Δp = 420bar, β = 20% and n = 1000 rpm, Δp=420bar, β=100%, respectively). The pressure field is also dominated by the pressure diffusion from the displacement chambers and ports. The fluid film thickness is sufficiently thick and seems to have an adequate load carrying capacity at this operating point. The fluid film is much thicker overall than in the

previous operating condition (low pressure). An overall good behavior of the fluid film at this operating condition.

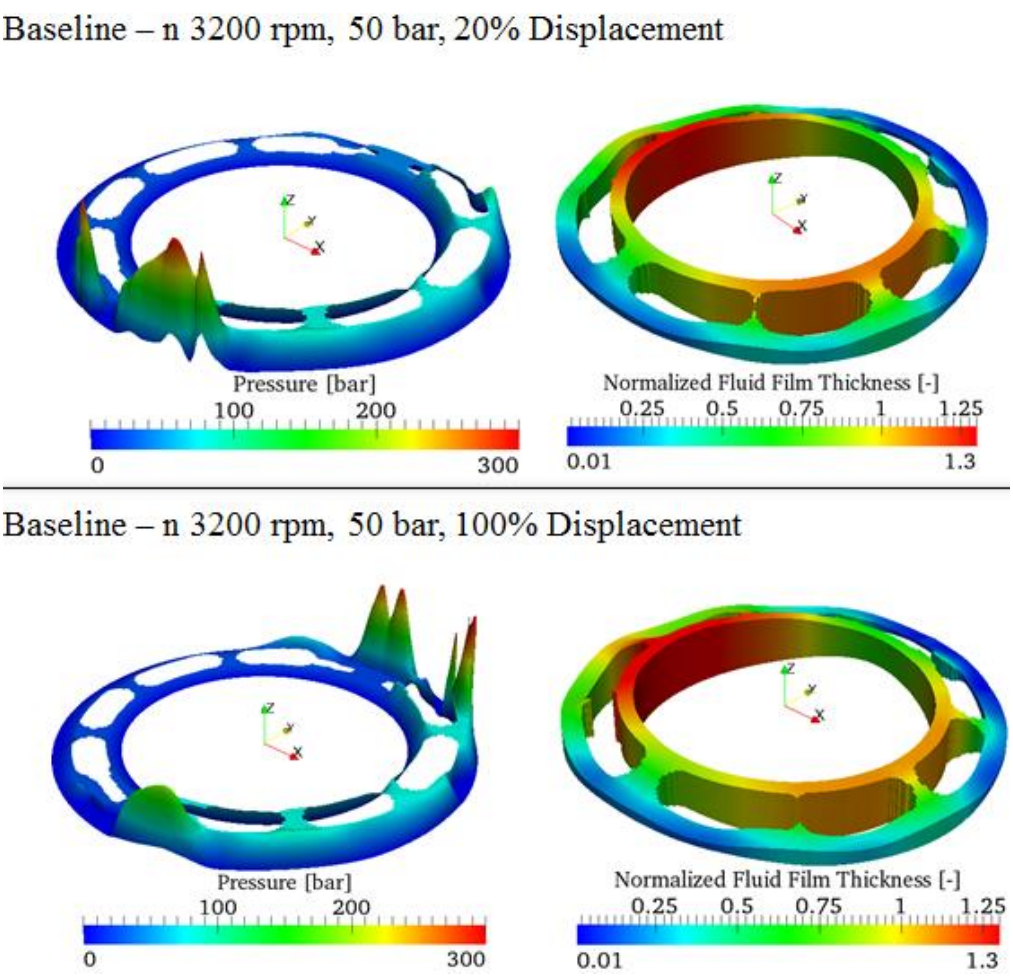

Figure 5.4. 3D Representation of the fluid film pressure (left) and thickness (right) for n=3200 rpm, Δp=50 bar, β=20% (top) and n=3200 rpm, Δp=50 bar, β=100% (bottom).

Figure 5.4 shows simulation results for operating conditions 5 and 6 (n = 3200 rpm, Δp=50 bar, β=20% and n = 3200 rpm, Δp=50 bar, β=100%, respectively). The pressure field has pressure spikes near the areas of localized low fluid film. The thin fluid film is not able to carry the loads. Additionally, the fluid film thickness is high on the inner edge (inner radius) and extremely low in some point on the outer edge (outer radius). Poor performance of the cylinder block/valve plate interface at these operating conditions.

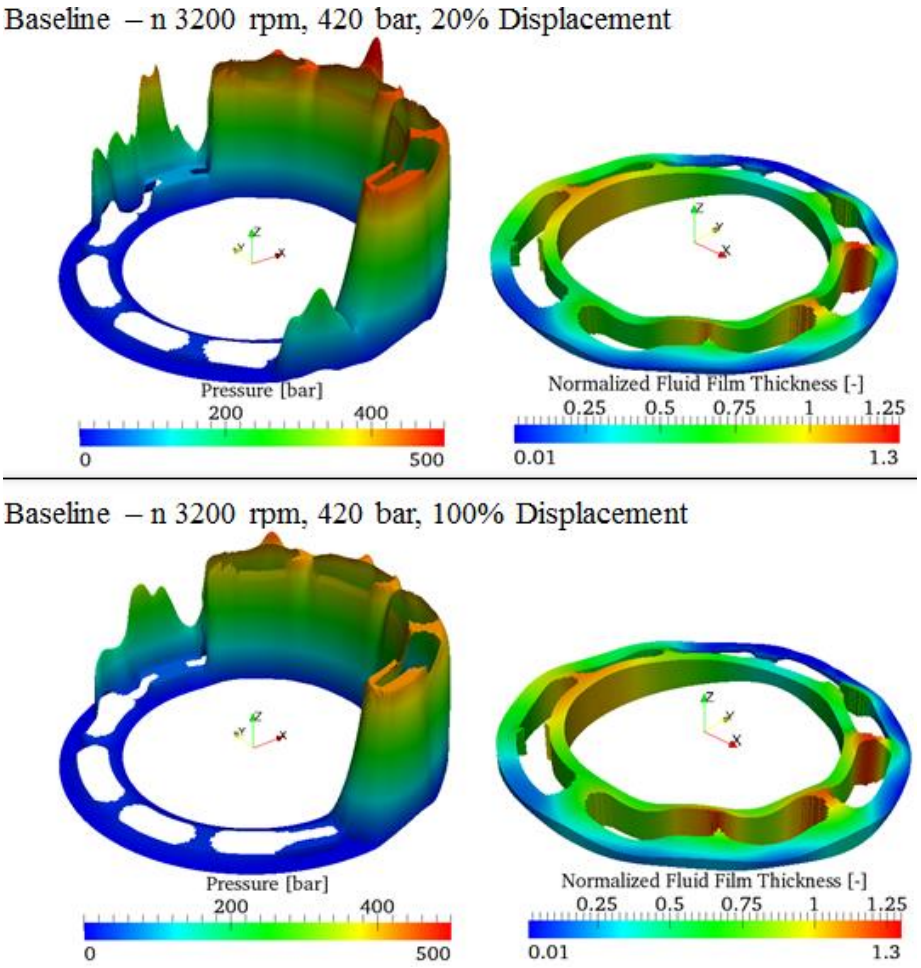

Figure 5.5. 3D Representation of the fluid film pressure (left) and thickness (right) for n=3200 rpm, Δp=420 bar, β=20% (top) and n=3200 rpm, Δp=420 bar, β=100% (bottom).

Figure 5.5 shows simulation results for operating conditions 7 and 8 (n = 3200 rpm, Δp = 420bar, β = 20% and n = 3200 rpm, Δp = 420bar, β = 100%, respectively). The pressure field is also dominated by the pressure diffusion from the displacement chambers and ports. Pressure spikes are present on the outer dead center (positive y-axis), corresponding to low fluid film. The fluid film thickness is extremely low close to the outer dead point; besides this the fluid seems to be able to carry the load without problems.

More results have been illustrated in order to have a full comprehension of the performance of the interface at such operating conditions. The leakage and friction losses

were plotted in the following figures. The leakage values for all presented results in this thesis were normalized using the highest average leakage of the baseline design. Similarly, the friction torque losses were normalized using the highest friction torque loss from the baseline design.

At operating condition 1, it is observed a very low leakage flow, which corresponds to the previous figures shown in Figure 5.2. An extremely low fluid film thickness was shown. Simultaneously the torque losses are quite high.

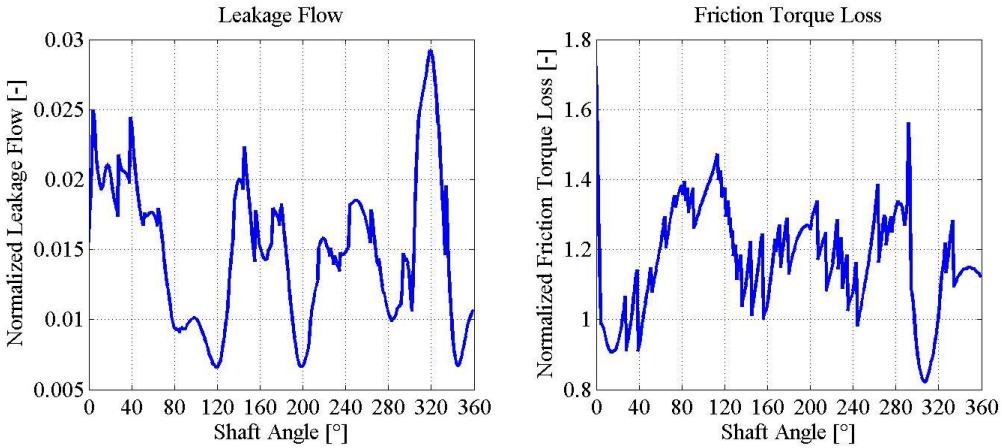

Figure 5.6. Normalized leakage (left) and normalized friction losses (right) for n=1000 rpm, Δp=50 bar, β=20% (operating condition 1).

Operating condition 2 shows similar results to the ones seen in the previous figure. Low leakage and high friction loss both correspond to the fact that an extremely low fluid film thickness is observed at both operating conditions, also shown in Figure 5.2.

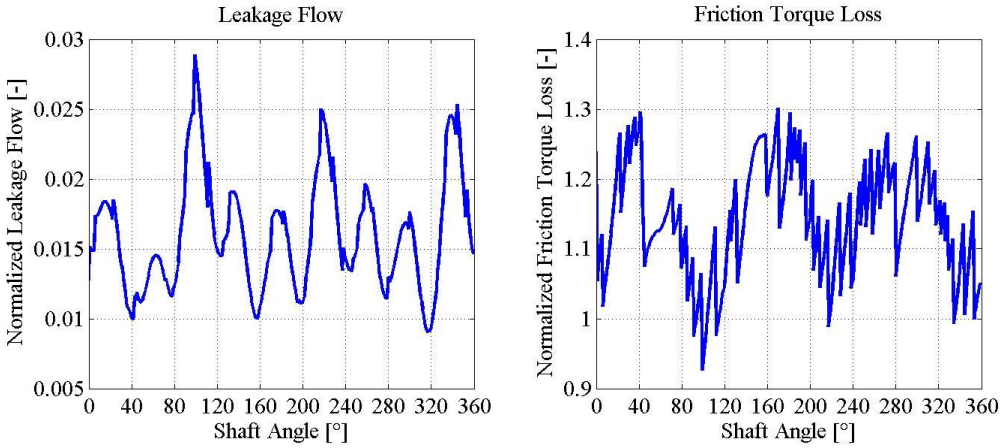

Figure 5.7. Normalized leakage (left) and normalized friction losses (right) for n=1000 rpm, Δp=50 bar, β=100% (operating condition 2).

In the following, operating condition 3, shows a higher leakage flow and a much lower friction loss. These results can be well explained with results shown previously on Figure 5.3, the fluid film presented a more uniform and thicker thickness over the whole lubricating gap which results in a good load carrying ability; and simultaneously, moderate leakage and low friction torque loss.

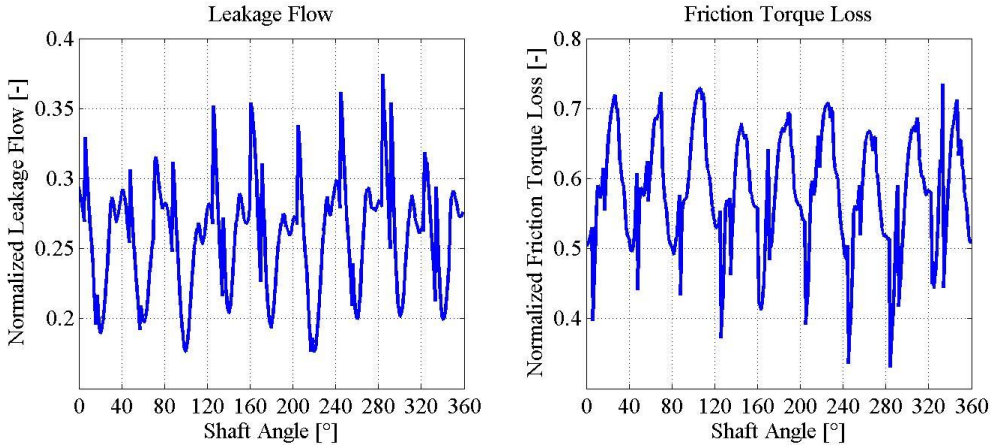

Figure 5.8. Normalized leakage (left) and normalized friction losses (right) for n=1000 rpm, Δp=420 bar, β=20% (operating condition 3).

Next operating condition 4 shows a moderate leakage flow and low friction loss, similar to operating condition 3. These results can be well explained with results shown previously on Figure 5.3, the fluid film also presented a more uniform and thicker

thickness which results in a good load carrying ability; and simultaneously, moderate leakage and low friction torque loss.

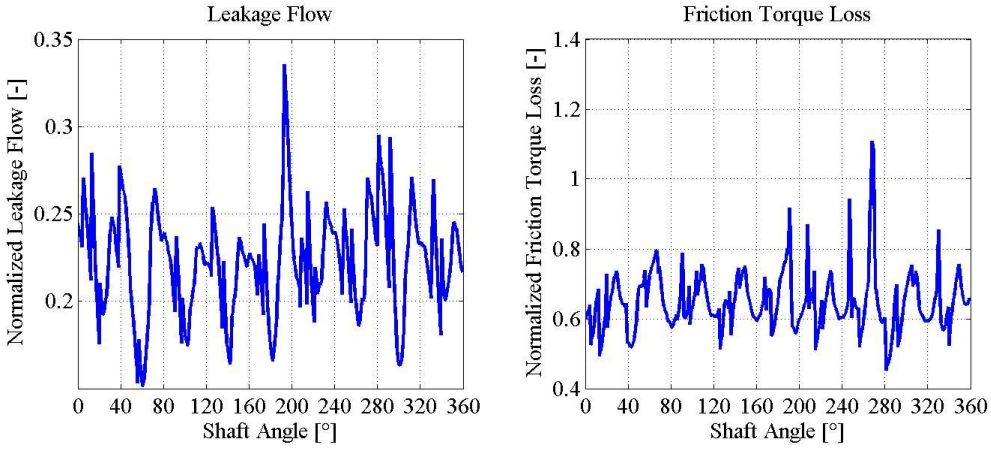

Figure 5.9. Normalized leakage (left) and normalized friction losses (right) for n=1000 rpm, Δp = 420 bar, β = 100% (operating condition 4).

Operating condition 5, shows higher leakage. This can be explained by the fact that the fluid film thickness is thicker on the inner edges (or inner radius) as shown in Figure 5.4. Also, high friction torque losses are observed, again explained in the same Figure 5.4 where low fluid film thickness is observed in the outer edge (or outer radius). This fluid film geometry or behavior can be explained by the thermal deformations of the solids (explained in the following section).

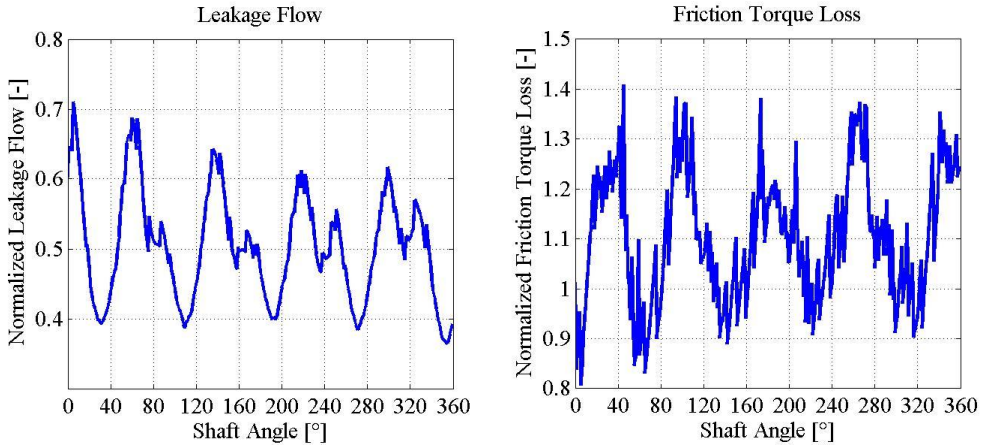

Figure 5.10. Normalized leakage (left) and normalized friction losses (right) for n=3200 rpm, Δp = 50 bar, β = 20% (operating condition 5).

Similarly as in the previous simulation results, but now for operating condition 6, relatively high leakage is observed. The leakage is explained by the thick fluid film in the inner radius shown in Figure 5.4. The friction torque loss is lower than the one shown for operating condition 5, but is still quite high.

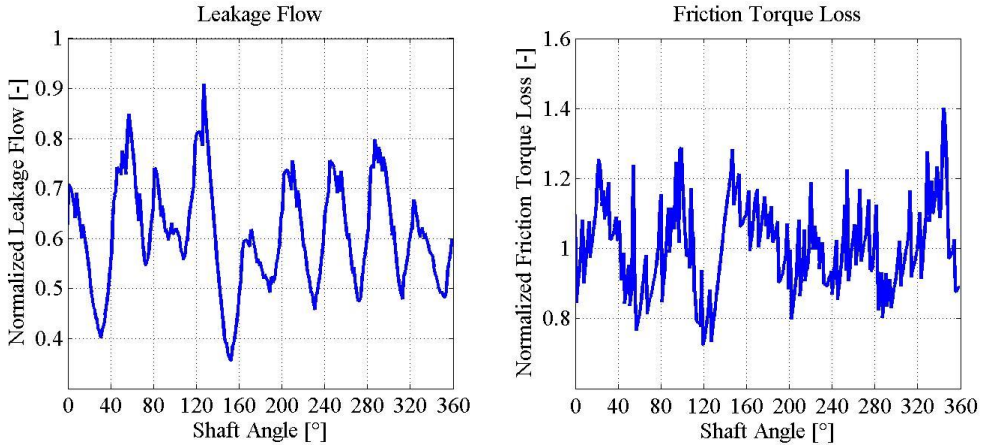

Figure 5.11. Normalized leakage (left) and normalized friction losses (right) for n=3200 rpm, Δp = 50 bar, β = 100% (operating condition 6).

Following, operating condition 7 and 8 show the highest leakages of all of them. Two main reasons, a thicker fluid film and higher pressure differential than operating condition 5 and 6. The friction torque loss is moderate relatively due to the fact that the operating condition pressure differential is higher.

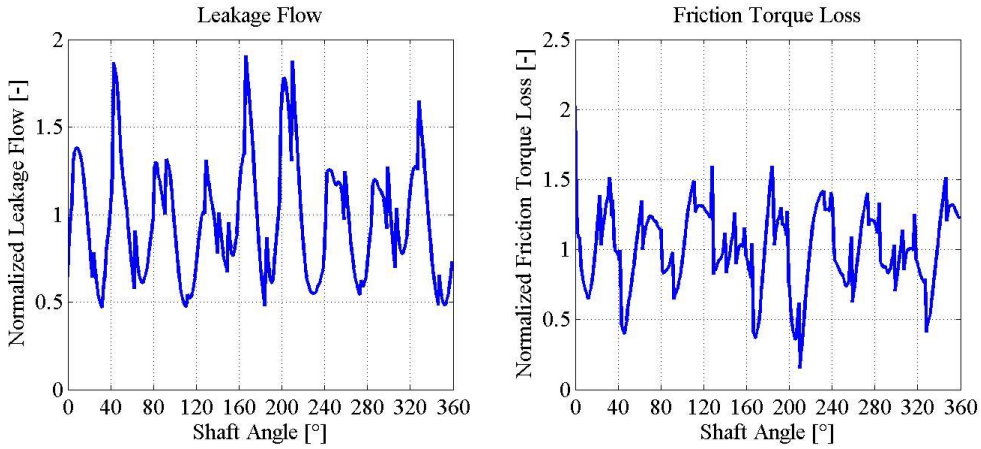

Figure 5.12. Normalized leakage (left) and normalized friction losses (right) for n=3200 rpm, Δp = 420 bar, β = 20% (operating condition 7).

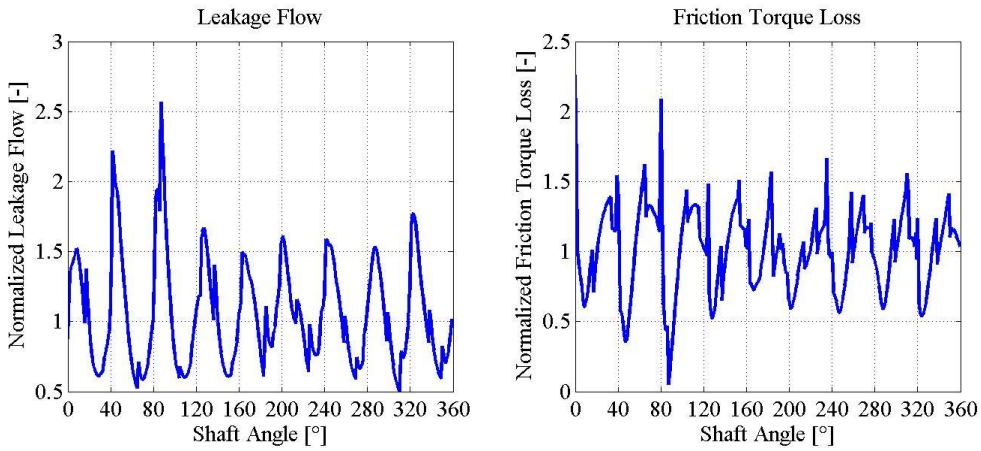

Figure 5.13. Normalized leakage (left) and normalized friction losses (right) for n=3200 rpm, Δp = 420 bar, β = 100% (operating condition 8).

From the previous results, it can be concluded that the fluid film thickness and performance is tightly related to the shaft rotational speed and the pressure differential, whereas not so much on the machine's displacement.

In the following figure the total energy dissipated from the interface was normalized with respect to the theoretical power delivered by the axial piston machine at different operating conditions (labeled in the x-axis; the numbering corresponds to Table 4.2. Operating conditions).

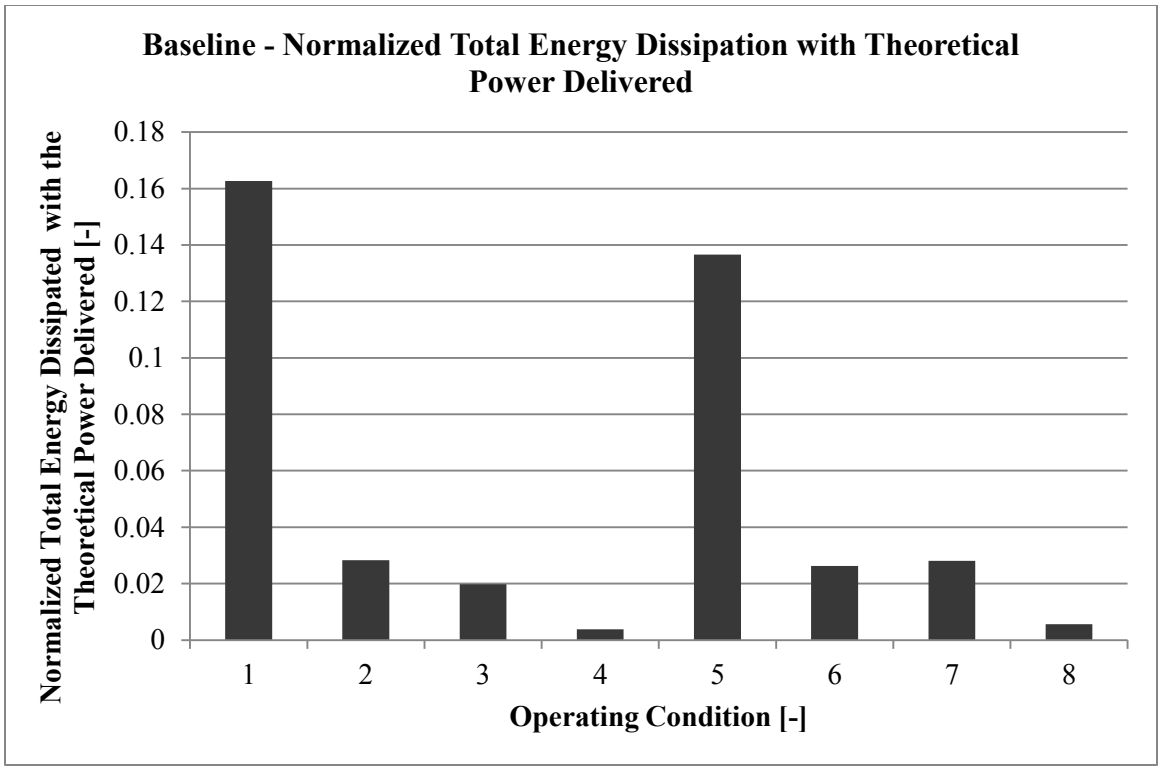

Figure 5.14. Normalized total energy dissipated with respect to theoretical power delivered.

From this graph, it is clear that the total energy dissipated is higher at the lower pressure differential and lower displacement operating conditions, when compared to the theoretical power delivered. This last figure corresponds to the fact that the overall piston machine efficiency drops at lower pressures. The potential to improve the overall machine's performance is significant, possible through improving the performance of the cylinder block/valve plate interface. Is important to note, the cylinder block/valve plate interface is not the only source of power loss. Other main contributors exist such as the energy dissipated in the two other lubricating interfaces: piston/cylinder and slipper/swashplate interface.

5.2 Cylinder Block/Valve Plate Interface: Elastic Deformations Effects

In this work, elastic deformations of the solids were considered through the use of the model developed by Zecchi (2012). The elastic deformations of the solids due to pressure

and thermal loading have a great impact on the general performance of the fluid film. They directly impact the fluid film geometry.

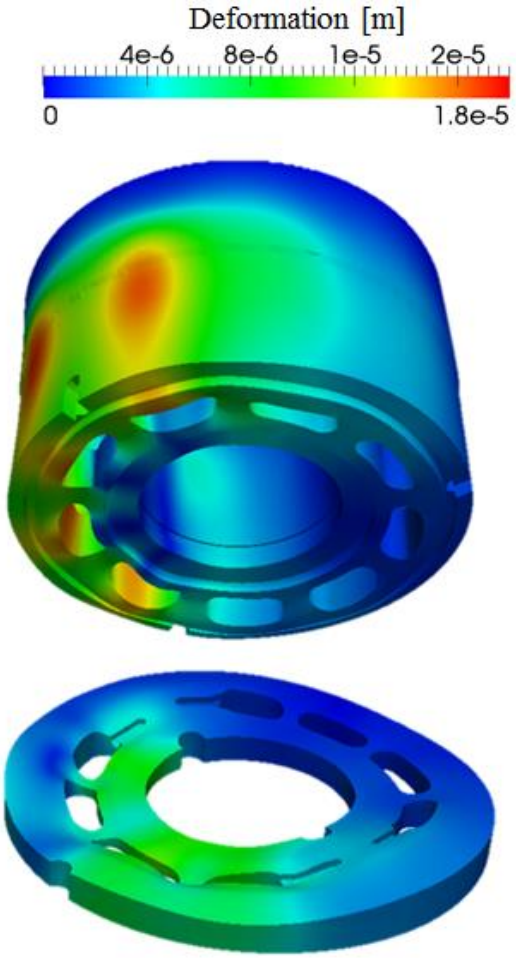

Figure 5.15. Example elastic deformation of the solids; cylinder block (top) and valve plate (bottom) (Scaled x1000).

In Figure 5.15, an example deformation of the solids due to pressure and thermal effects are shown. It is seen the large deflection that the solids reflect on the lubricating surfaces. In Figure 5.16, these deformations on the surfaces have been broken down into: thermal deflections and pressure deformations.

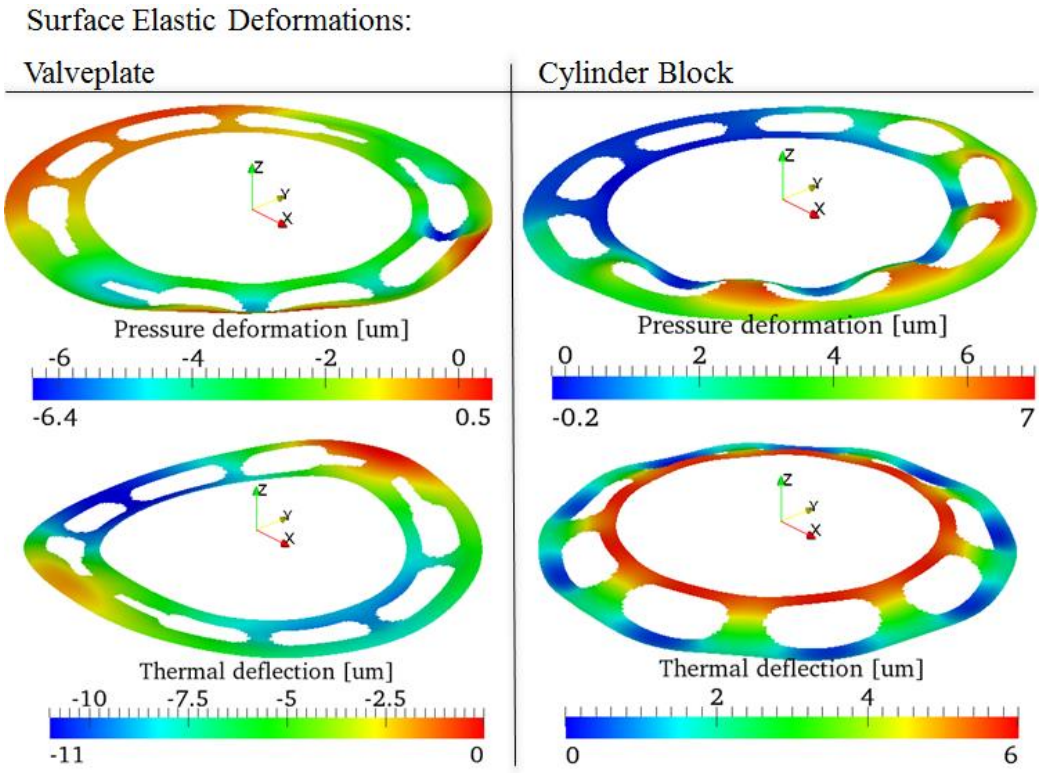

Figure 5.16. Elastic deformations of the solids due to pressure and thermal effects.

Figure 5.16 shows a representation of the deformation of the solids at a specific operating condition. The deflections on the surfaces are in the same order of magnitude than the fluid film thickness itself. In the case of pressure deformation it is beneficial for the performance of the cylinder block interface at some operating conditions. It is beneficial for two main reasons:

1. Additional pressure generation due to hydrodynamic effects thus increased load carrying capacity. This extra hydrodynamic effect is explained by how the running surface of the cylinder block deforms. The cylinder block has pressurized fluid acting on the sealing land and inside the displacement chamber. The pressure in the displacement chamber makes the surface deform in a waved pattern shape, this induces extra hydrodynamic effects due to the wedge effect. The pressure deformation of the cylinder block is shown in Figure 5.17 (b). These deformations are the relative deformations of the solids in the z-direction, the deformations are relative to the undeformed surface of the valve plate (plane z=0)

in the case of the cylinder block the deformation is in the + z-direction and in the case of the valve plate the deformation is in the – z-direction.

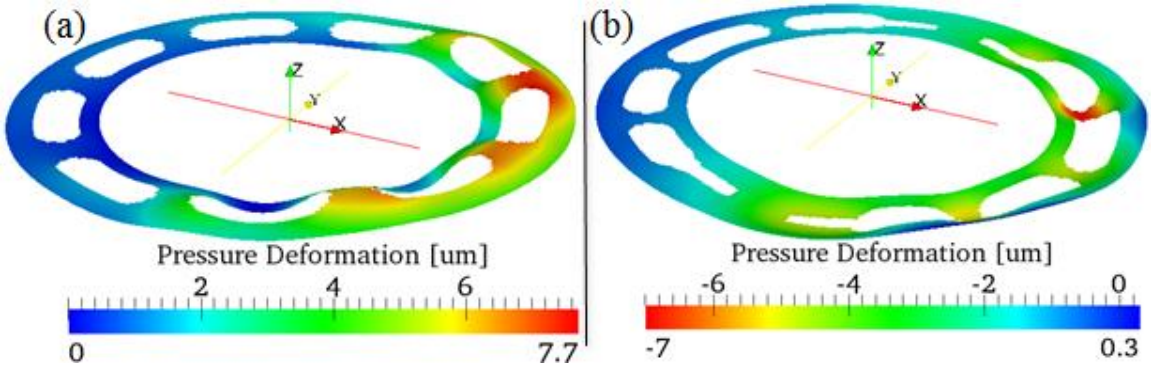

Figure 5.17. Pressure deformations; the cylinder block (a) on the left and the valve plate (b) on the right (Scaled x1000).

2. The pressure deformation in both the cylinder block and valve plate is observed in Figure 5.17. It is clear that the surface deforms concavely, thus increasing the load carrying capacity of the interface. Moreover, the 3D representation of the fluid film between these two surfaces is represented in Figure 5.1, where the concavity of the surfaces is confirmed.

The thermal effects are also of high significance. The solution of the Energy equation is used to calculate the temperature distribution in the gap and calculate an average heat flux transmitted from the gap towards the contacting surfaces of the solid bodies; cylinder block and valve plate. This information is in turn used to calculate the distribution of the temperature in the bodies. An example of this temperature distribution is shown in the following figure.

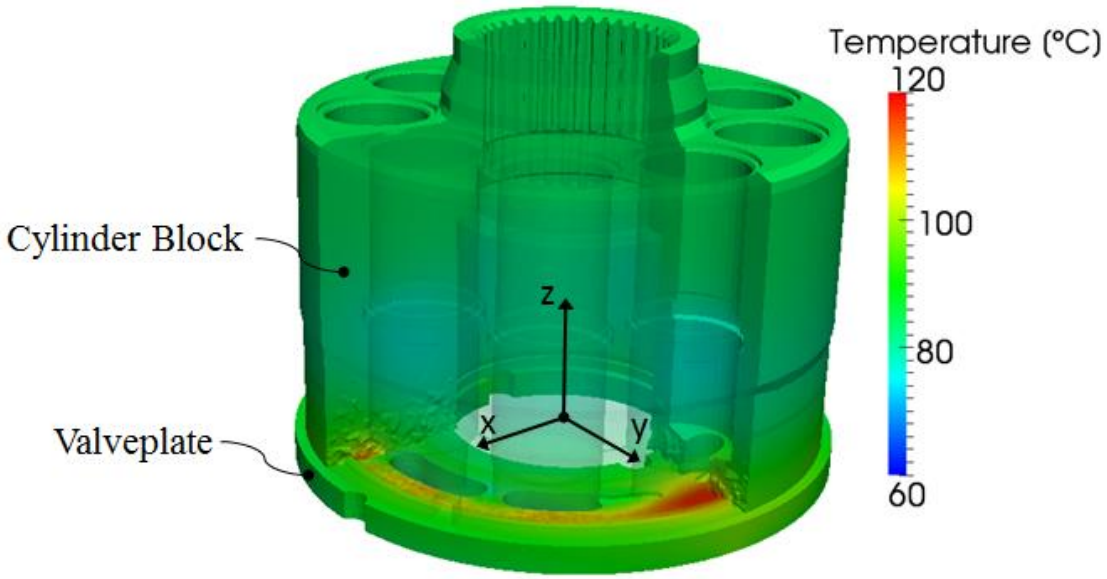

Figure 5.18. Temperature distribution of cylinder block and valve plate solid bodies.

Figure 5.18 shows the temperature distribution of the solid bodies composing the cylinder block/valve plate interface. It is shown that the hot spots are clearly on the surfaces contacting the lubricating film. These temperature gradients in the solids introduce thermal stresses into the solid bodies and cause them to deflect elastically.

Examples of such elastic deformations due to thermal effects are shown in Figure 5.19 and Figure 5.20, where the temperature and thermal deflection are shown for the valve plate and the cylinder block, respectively.

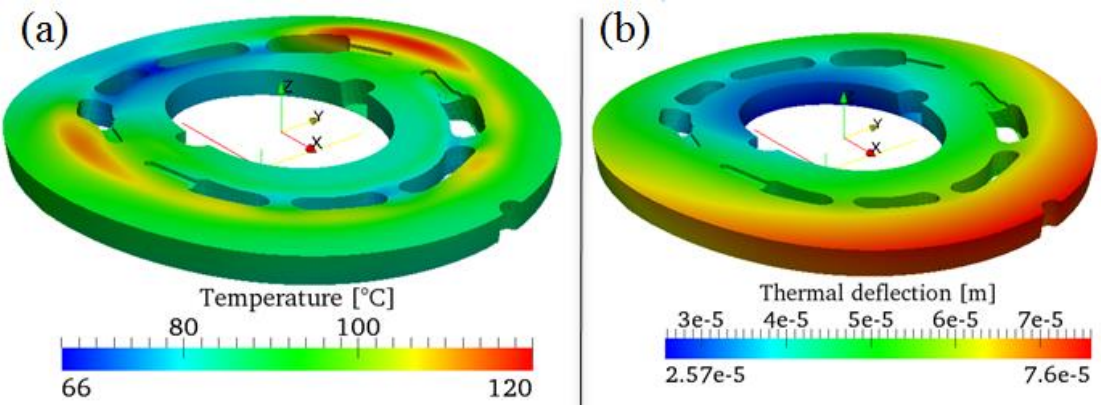

Figure 5.19. 3D Representation of the deformation of the solid bodies (Scaled x1000); temperature distribution represented in (a) and thermal deflection magnitude in (b).

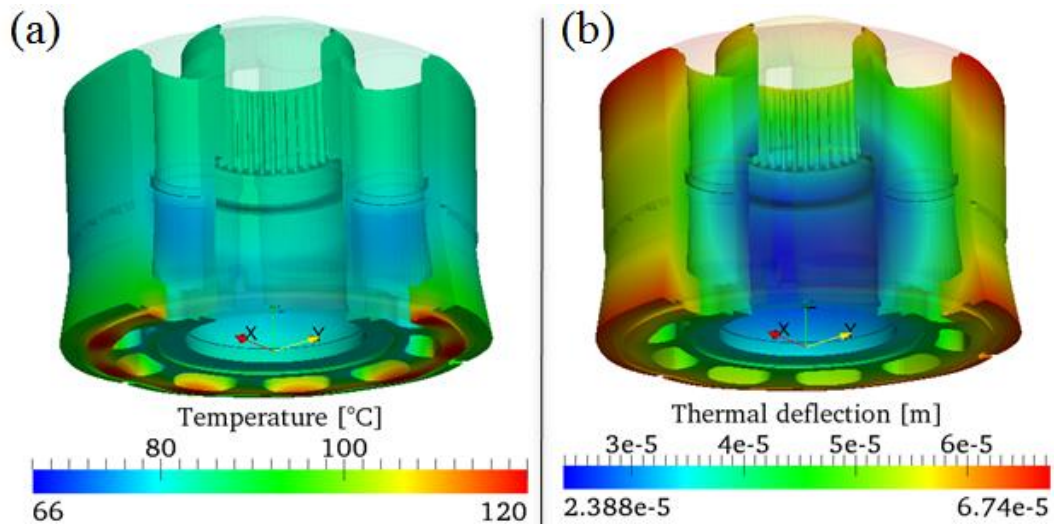

Figure 5.20. 3D Representation of the deformation of the solid bodies (Scaled x1000); temperature distribution represented in (a) and thermal deflection magnitude in (b).

In the figures above, thermal deflections are explained by the two predicted temperature fields of the cylinder block, and valve plate/end case assembly. The temperature profile of the valve plate is typically non-symmetric; the region at high temperature is related to the low fluid film region location. A convex deformation is observed on the valve plate due to the geometry of the valve plate and end case, thus reducing the load carrying capacity of the gap. The cylinder block is characterized by an axisymmetric temperature profile, where the higher temperature region is over the sealing land. The deformation is concave about the shaft axis, axisymmetric; it deforms the fluid film in the same order of magnitude as the fluid film thickness itself. It is critical to account for thermal effects for the correct prediction of the fluid film thickness and shape, in order to predict the behavior of the thin fluid film accurately.

CHAPTER 6. MICRO-SURFACE SHAPING ON THE VALVE PLATE

In this section, complete analyses of micro-surface shaping effects on the cylinder block/valve plate's interface are described. First, the simulation results for the best design are shown. Second, in the parameters used to define the sinusoidal wave on the valve plate's running surface were studied; varying amplitude, frequency (number of waves), and offset (starting point). The purpose of this section is to understand the effects of the micro-surface shaping on the cylinder block/valve plate's interface performance. the overall simulation results will be analyzed. Finally, the simulation results will be divided into three more sections; the effects of the amplitude, the frequency and the offset on the performance of the interface.

6.1 Results for a 2μm Amplitude, Frequency 15 and 75% Offset Profile

The base design of 2μm amplitude, frequency 15 and 75% offset, was chosen to illustrate the simulation results of this investigation. It presents the best compromise between reduction in total energy dissipation at low pressure operating conditions, and a moderate increase in leakage at higher pressure operating conditions.

In Figure 6.1, a 3D representation of the pressure and fluid film thickness are shown; on the left hand side the pressure and on the right the fluid film thickness values. The figures on the top are the results for the standard design valve plate, and the results for the micro shaping for design 2 μm amplitude, frequency of 15 and 75% offset are shown in the bottom. These simulation results are for operating condition 1 (n=1000 rpm, Δp=50 bar, and β=20%) defined in Table 4.2. Various features represented in this figure are significant for the performance of the interface. In Figure 6.2 (top-left), the pressure in the standard design is presented and in (top-right) the fluid film thickness is illustrated,

the fluid film thickness as seen is presenting an extremely low fluid film thickness. This condition can lead to high torque losses and possible contact solid to solid, which could cause wear-in or catastrophic failure. On the other hand, the representation for the micro-surface shaping results are presented in Figure 6.1 on the bottom. The effect of the waves is clear; hydrodynamic pressure is built in in the gap. Additional pressure spikes are observed at every location where it coincides with the peak of a wave, due to the wedge effect. The additional hydrodynamic pressure built in the gap results in an increase of the load carrying ability of the interface; thus increasing the fluid film thickness throughout the gap.

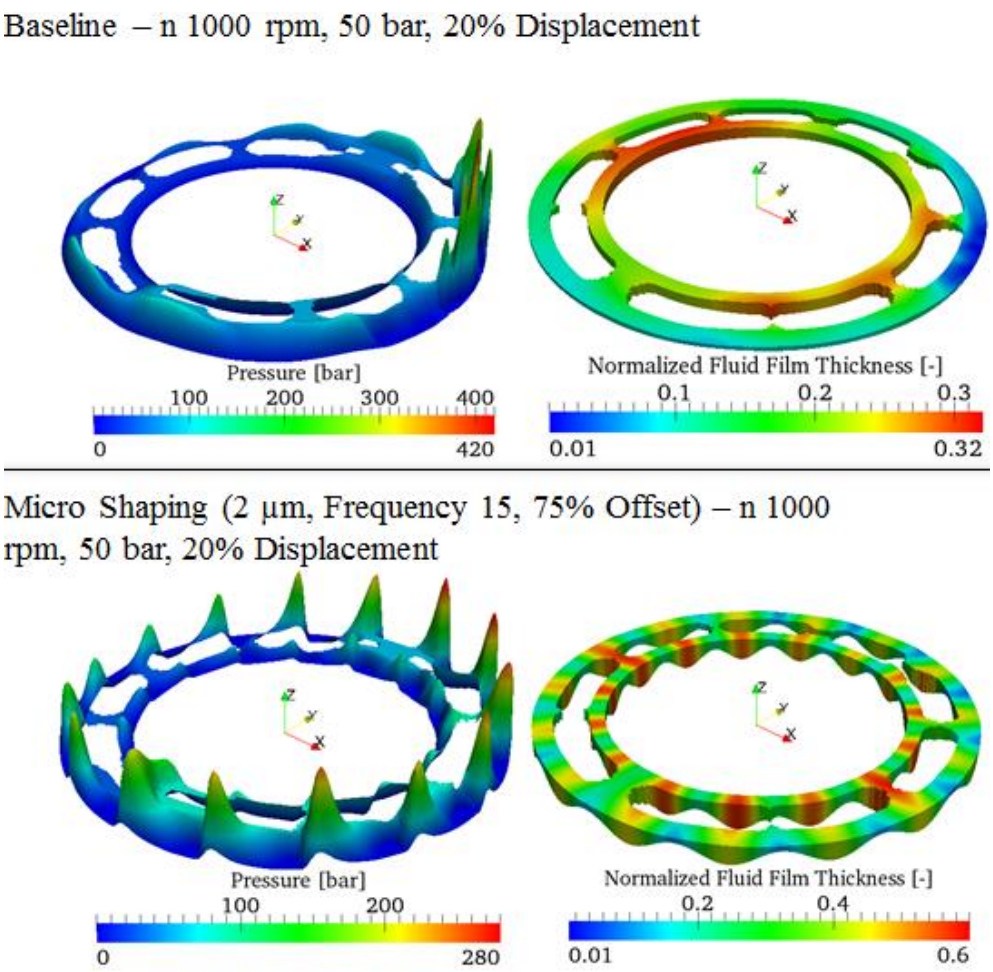

Figure 6.1. Comparison between standard and micro-shaping (2 µm, frequency 15, and 75% offset) at n=1000 rpm, Δp=50 bar, and β=20%; pressure (left) and fluid film thickness (right).

The results for operating condition 1 are shown in Figure 6.1. A thicker fluid film is observed for the waved valve plate resulting in lower friction torque losses and a moderate increase in leakage.

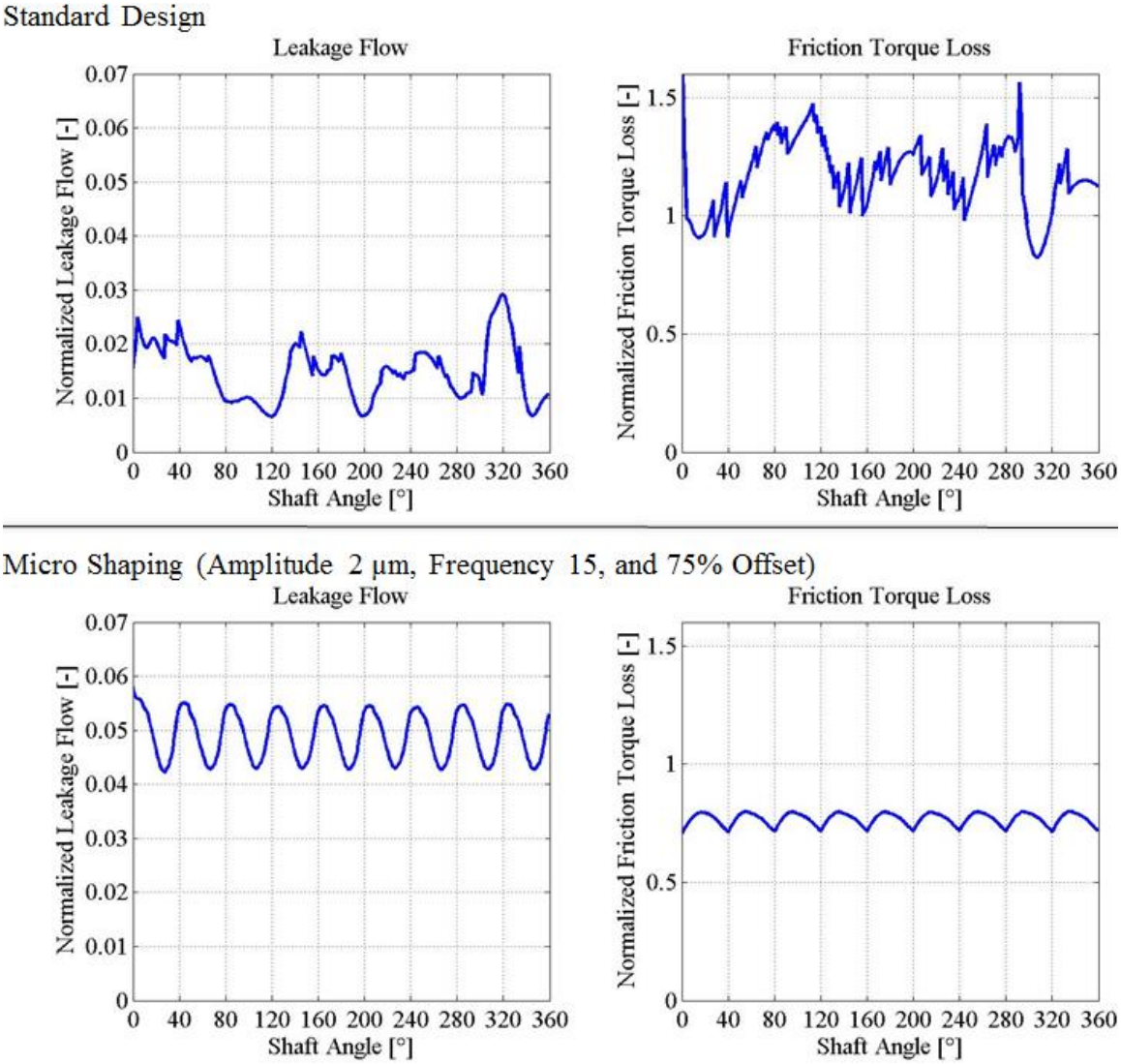

Figure 6.2. Leakage flow and friction torque loss for the standard and micro-shaping design (1000 rpm, 50 bar and 20% displacement).

In Figure 6.2, the leakage flow and torque loss predicted at this operating condition (1000 rpm, 50 bar, and low displacement) are represented, the standard design (top) and the micro-surface shaping design (bottom), respectively. It is clear that the fluid film is having problems carrying the load exerted on the cylinder block, thus experiencing extremely low fluid film thickness and high friction torque losses. This is why we see

such disturbances on the torque loss. On the other hand, the waved design shows a very smooth friction torque loss, which reflects an increased load carrying ability of the fluid film. A total of 40% reduction in total energy dissipation is achieved for the interface.

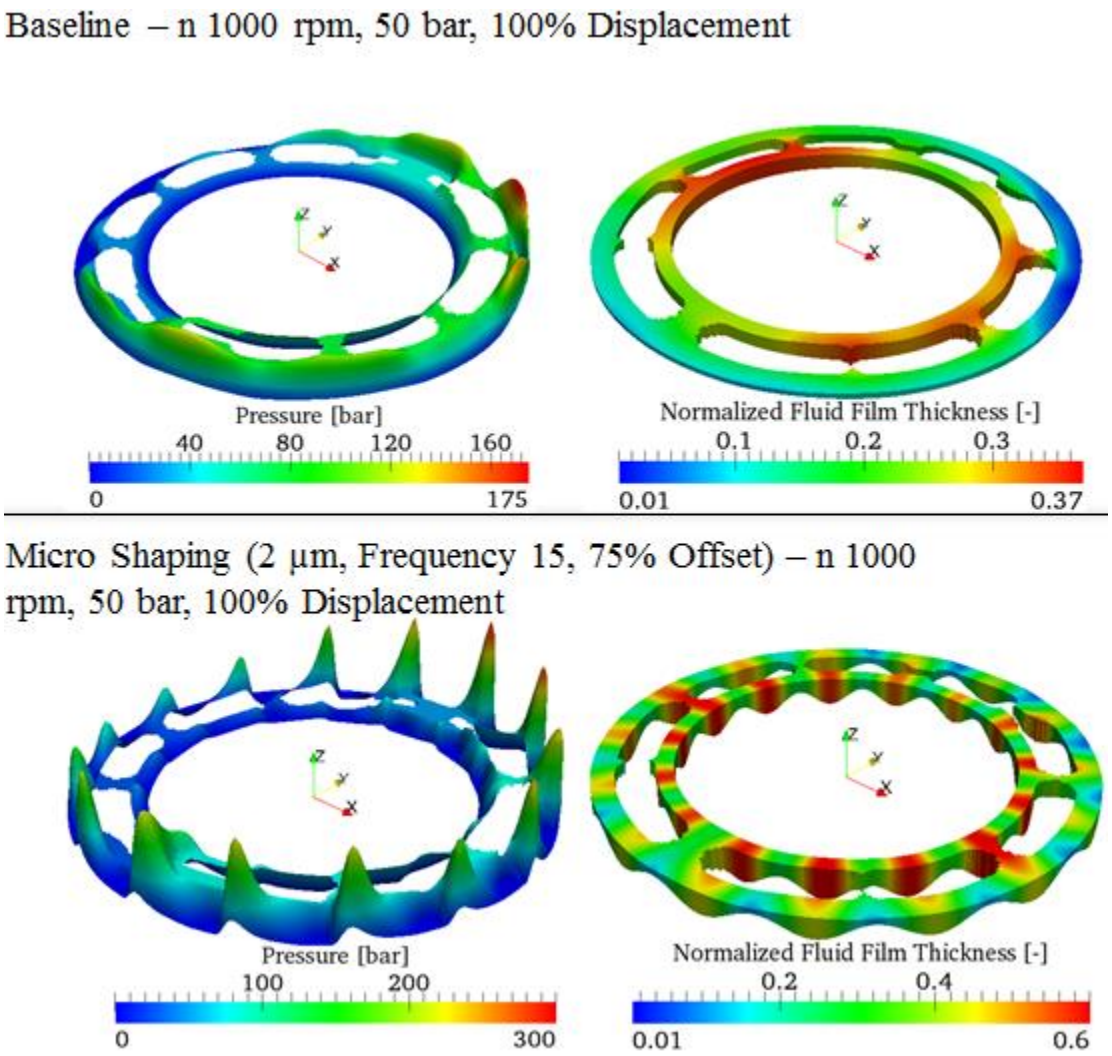

Figure 6.3. Comparison between standard (top) and micro-shaping (bottom, 2 µm, frequency 15, and 75% offset) at n=1000 rpm, Δp=50 bar, and β=100%; pressure (left) and fluid film thickness (right).

In Figure 6.3, the pressure and fluid film thickness are represented for the standard (top) and the micro-surfaced design (bottom). This operating condition, n=1000 Δp=50bar β=100%, shows a similar behavior as the previous operating condition discussed. Both show a significant increase in load carrying capacity due to the additional hydrodynamic

pressure built up in the gap. Simultaneously, the fluid film becomes thicker and the friction torque losses are significantly reduced.

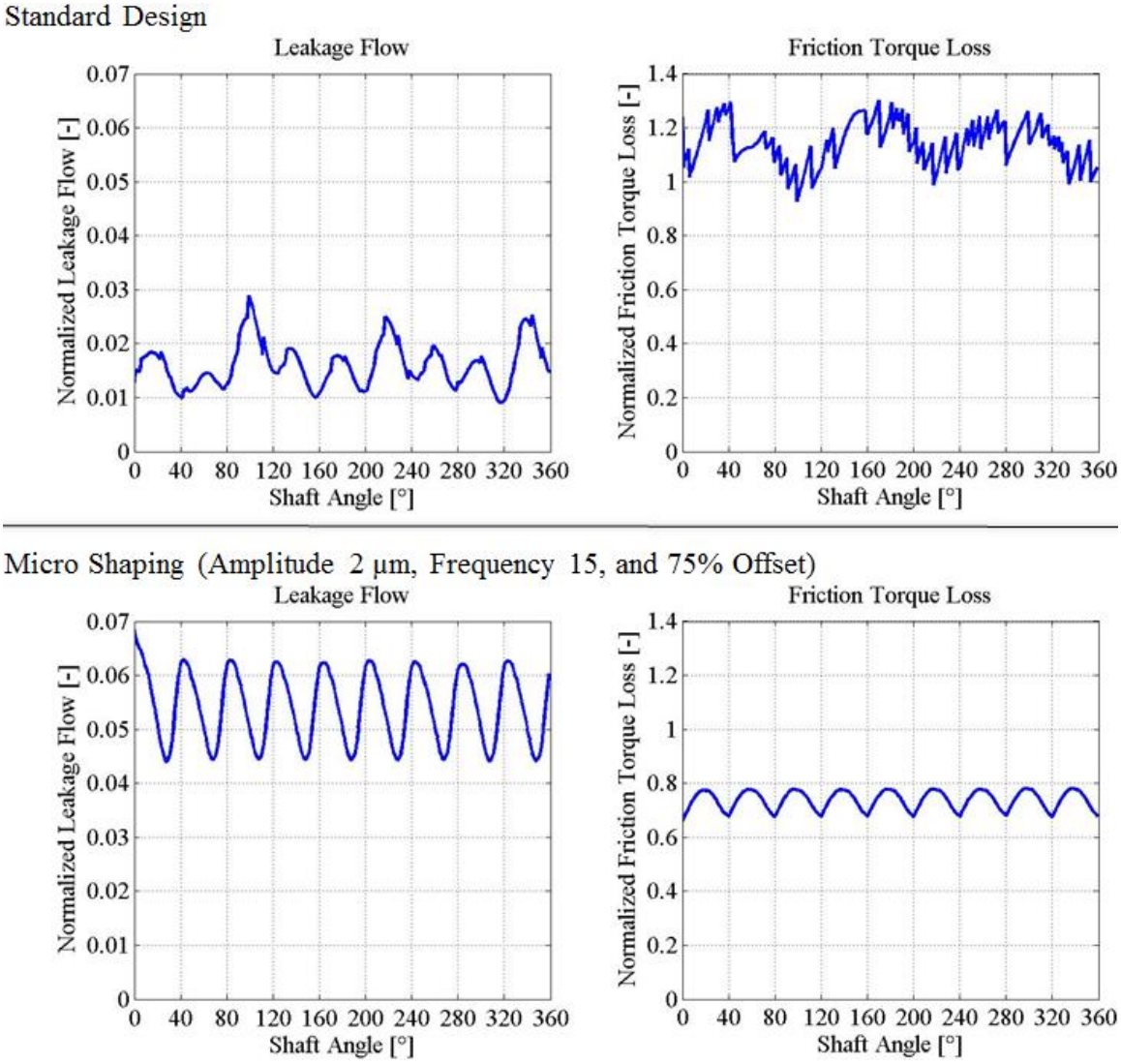

Figure 6.4. Leakage flow and friction torque loss for the standard and micro-shaping design (1000 rpm, 50 bar and 100% displacement).

In Figure 6.4, the leakage flow and torque loss predicted at this operating condition (1000 rpm, 50 bar, and low displacement) are represented, the standard design (top) and the micro-surface shaping design (bottom), respectively. The increase in load carrying ability increased the fluid film thickness, thus reducing the high friction torque losses. On the top-right figure, disturbances on the torque loss are visible due to the extreme low fluid film thickness. On the other hand, the waved design shows a very smooth friction torque

loss, which reflects an increased load carrying ability of the fluid film. A decrease in total energy dissipated in the gap of 34% relative to the baseline design was achieved.

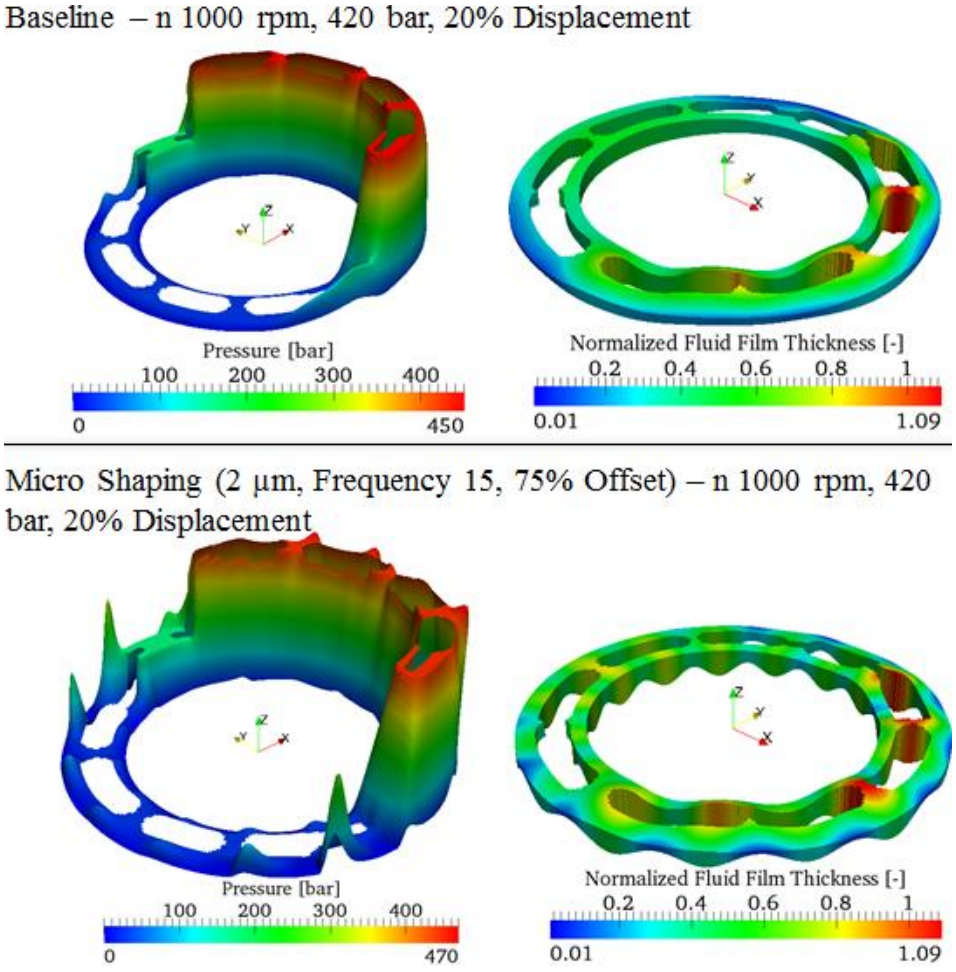

Figure 6.5. Comparison between standard (top) and micro-shaping (bottom, 2 µm, frequency 15, and 75% offset) at n=1000 rpm, Δp=420 bar, and β=20%; pressure (left) and fluid film thickness (right).

Figure 6.5, shows the simulation results for operating condition 3 (n=1000 rpm, Δp=420 bar, and β=20%). Pressure (left) and fluid film thickness (right) represented for both designs; the standard and micro-surfaced valve plate. Additional hydrodynamic pressure built up in the gap is present as well. In this case, increased fluid film thickness results in an increase of energy dissipated due to leakage flow in the gap.

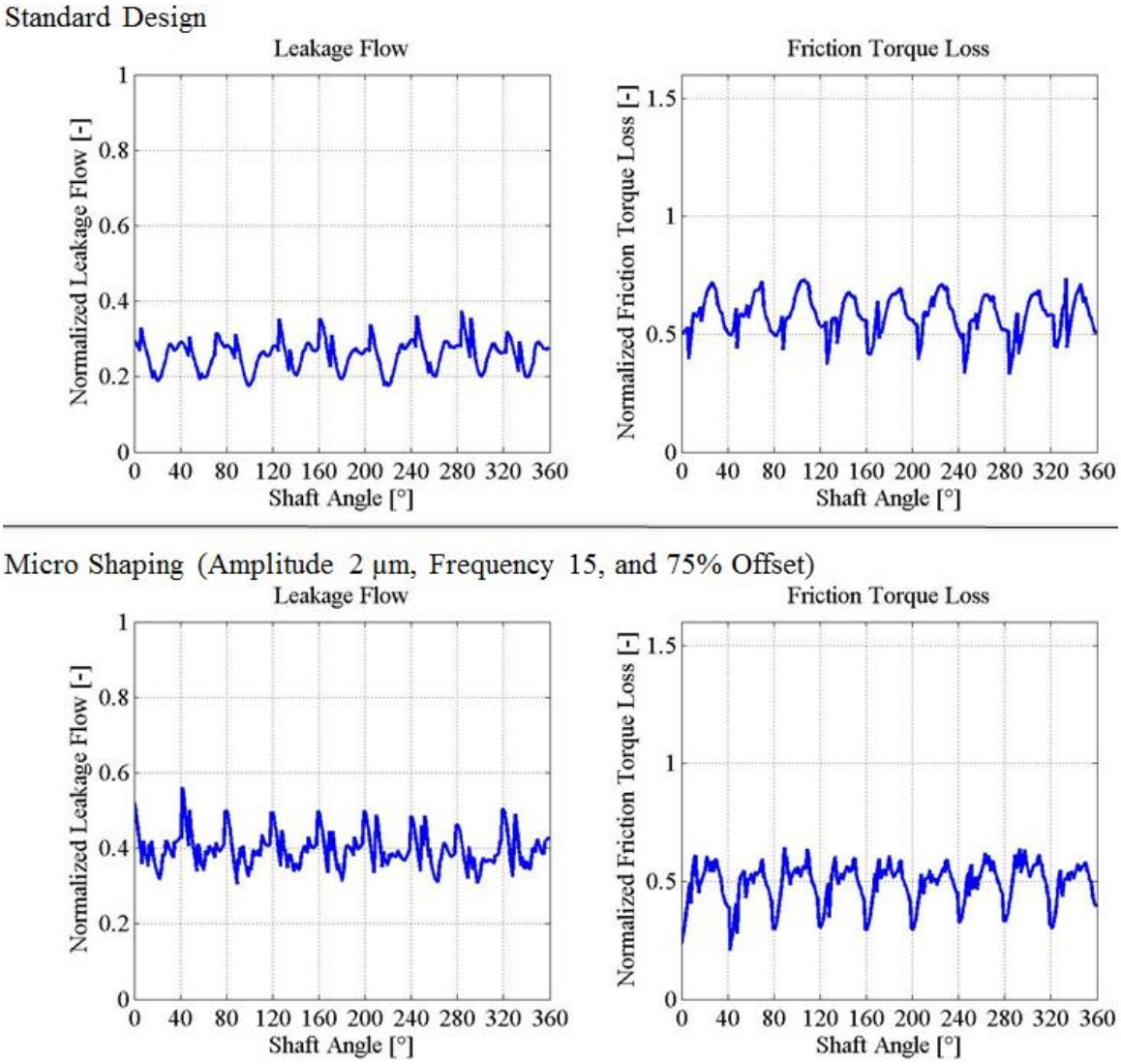

Figure 6.6. Leakage flow and friction torque loss for the standard and micro-shaping design (1000 rpm, 420 bar and 20% displacement).

Figure 6.6, shows a slight decrease in friction torque loss and an increase in leakage flow. In this case, the increase in energy dissipated due to leakage flow overcomes the reduction in energy dissipation due to reduced viscous friction; thus increasing the total energy dissipated in the thin fluid film by 23% relative to the baseline design.

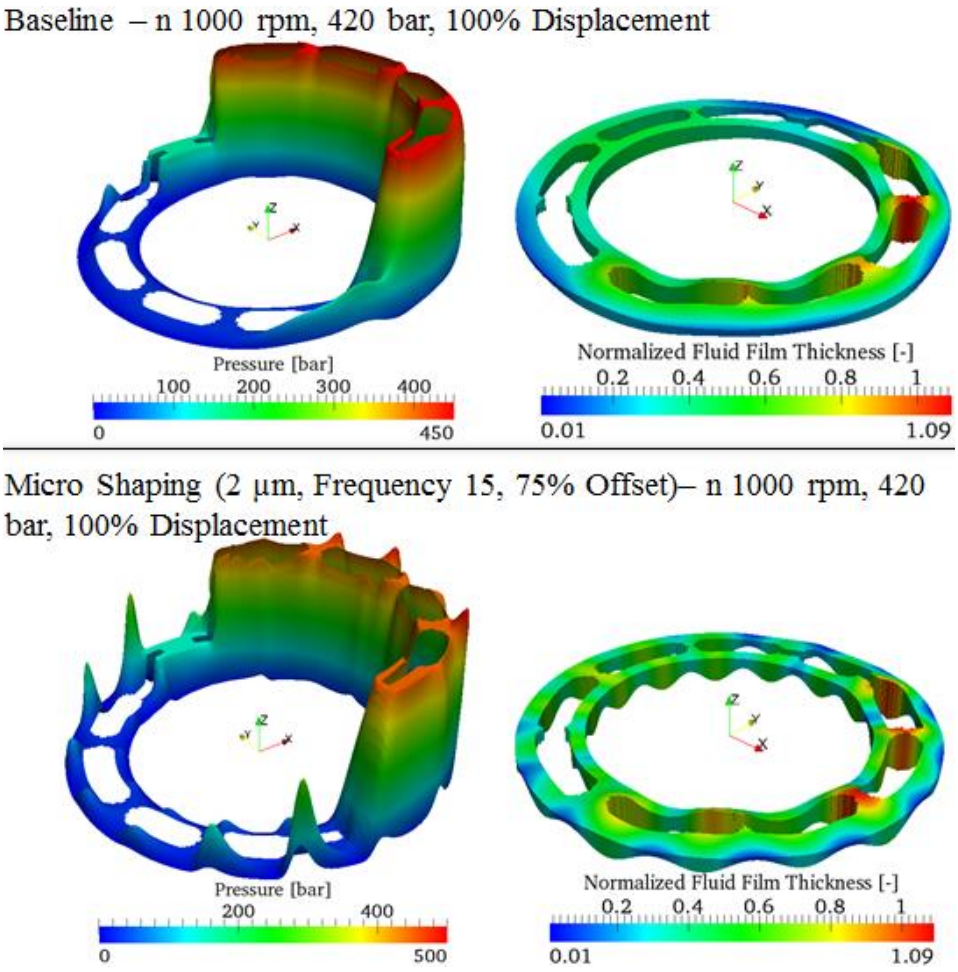

Figure 6.7. Comparison between standard (top) and micro-shaping (bottom, 2 µm, frequency 15, and 75% offset) at n=1000 rpm, Δp=420 bar, and β=100%; pressure (left) and fluid film thickness (right).

In Figure 6.7, the simulation results for operating condition 4, defined in Table 4.2, are shown. As in previous results the additional hydrodynamic pressure due to the waves is present. A slight increase in fluid film thickness is present as well.

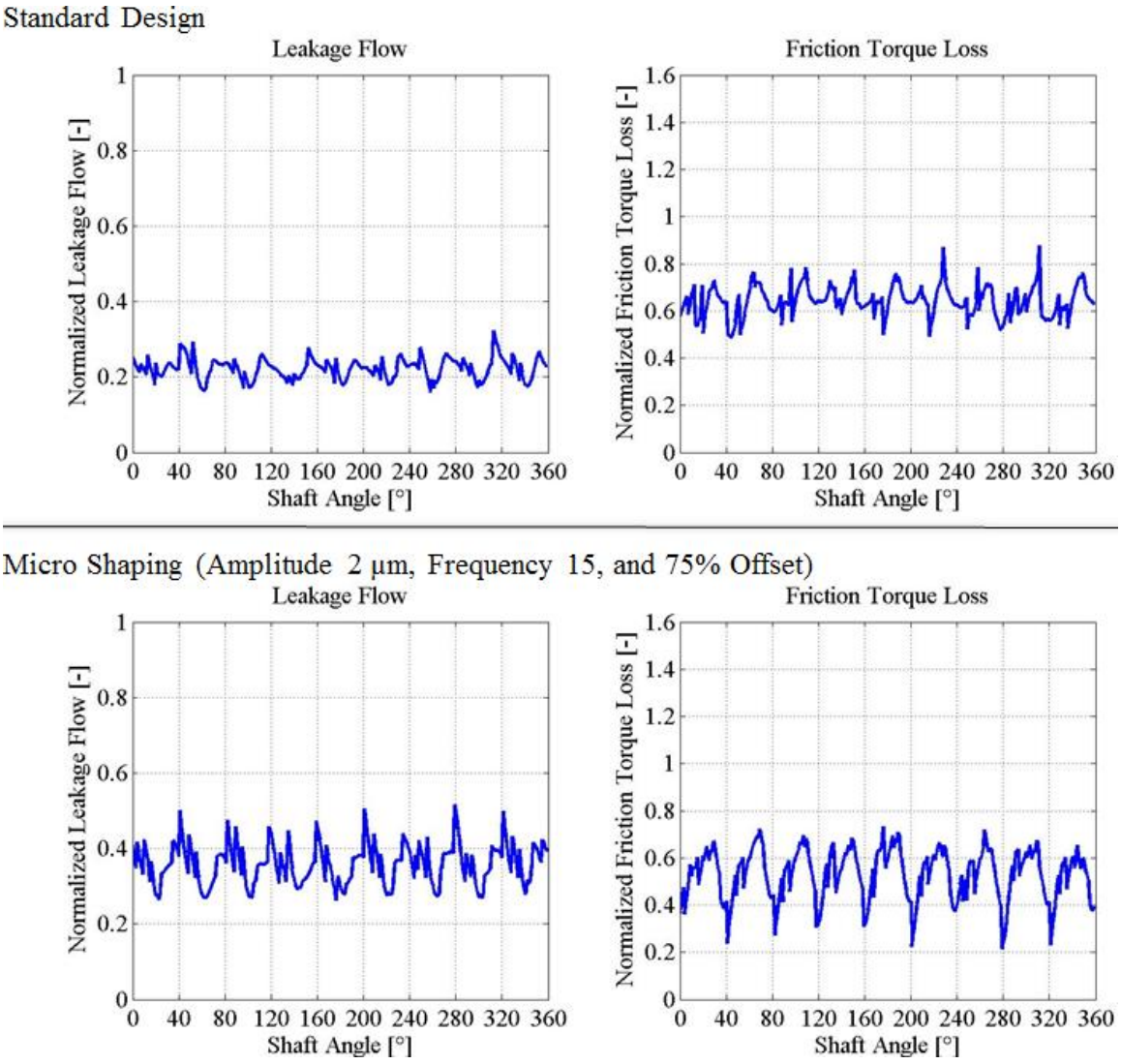

Figure 6.8. Leakage flow and friction torque loss for the standard and micro-shaping design (1000 rpm, 420 bar and 100% displacement).

Figure 6.8, shows the simulation results in terms of leakage flow (left) and friction torque loss (right). The power losses due to the leakage flow overpass the reduction in energy dissipation due to a reduced friction torque loss. This results in an overall increase of total energy dissipation of 22% relative to the original design.

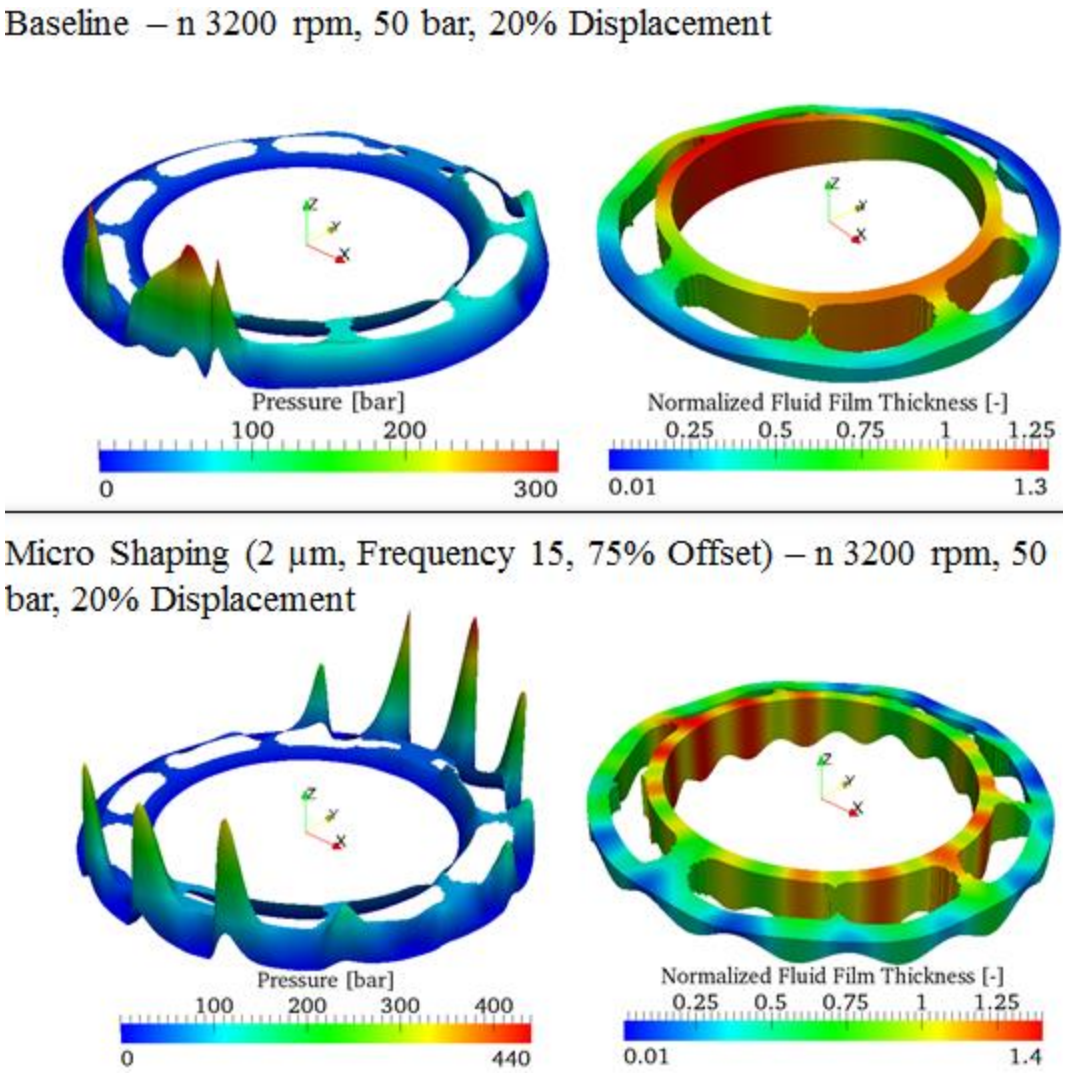

Figure 6.9. Comparison between standard (top) and micro shaping (bottom, 2 µm, frequency 15, and 75% offset) at n=3200 rpm, Δp=50 bar, and β=20%; pressure (left) and fluid film thickness (right).

In Figure 6.9, the simulation results for operating condition 5 are shown. The additional hydrodynamic pressure built up in the fluid film is increasing the load carrying capacity of the interface. These are shown as additional spikes on the bottom-left figure, which correspond to the location of the wave in the valve plate. It results in a much more stable fluid film. The extreme low fluid film thicknesses observed in the top-right figure are significantly reduced, compared to the bottom-right figure.

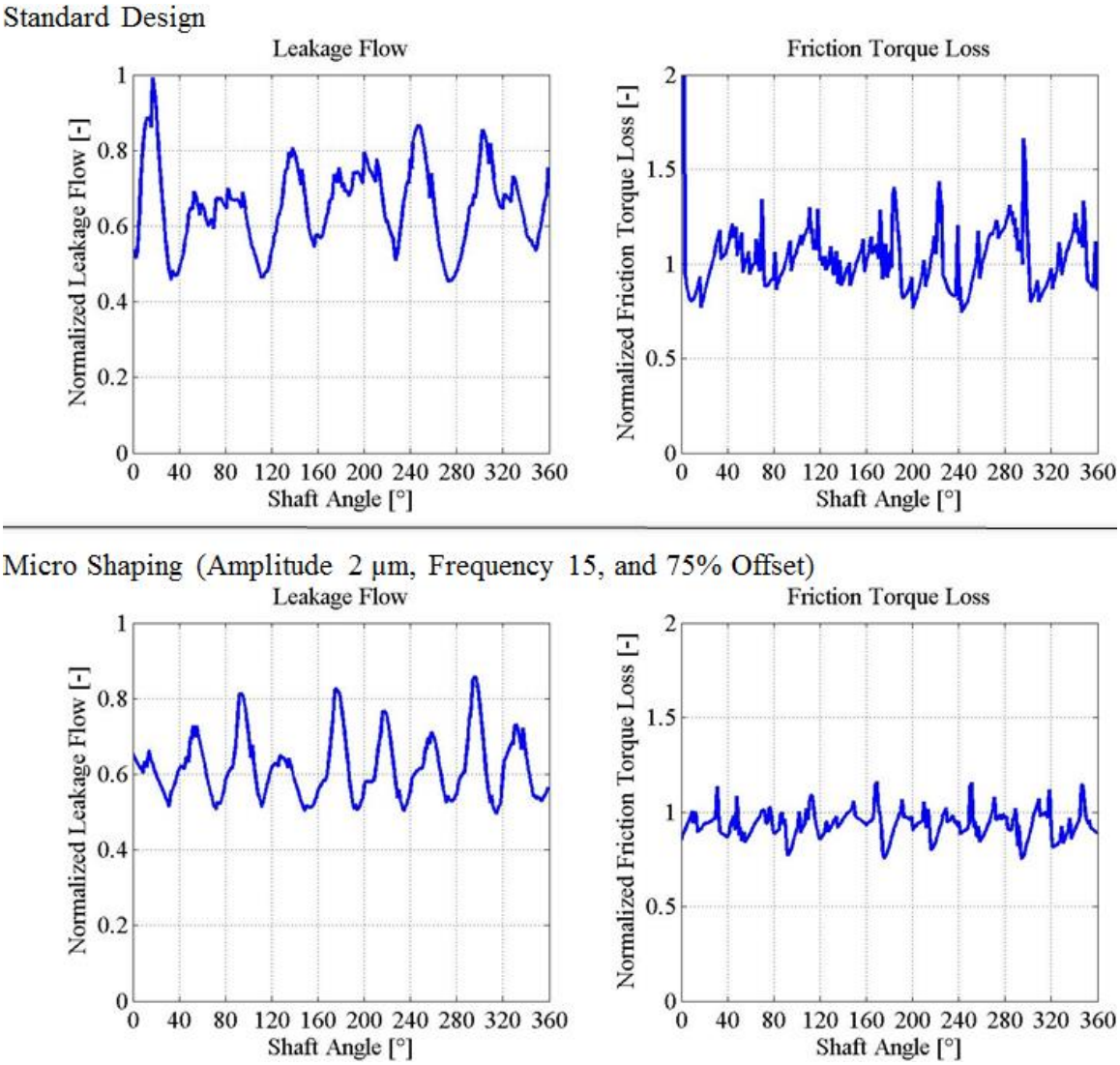

Figure 6.10. Leakage flow and friction torque loss for the standard and micro-shaping design (3200 rpm, 50 bar and 20% displacement).

Figure 6.10, shows the leakage flow and torque loss corresponding to rotational speed of 3200 rpm, 50 bar and low displacement (20% β). At this operating condition the benefits of the micro-surfaced pattern on the valve plate reduce both the leakage flow and the friction torque loss in the interface. This is explained by the fluid film geometry of the baseline (Figure 6.9). It shows a thick fluid film in the inner radius, which corresponds to a high leakage flow. Furthermore, an extremely low fluid film thickness is shown in the outer radius, which would generate high friction torque loss. The increase of load carrying capacity of the gap creates a better fluid film geometry which leaks less and

generates less viscous friction. These effects result in a reduction of total energy dissipation of 8% in the interface, compared to the baseline design.

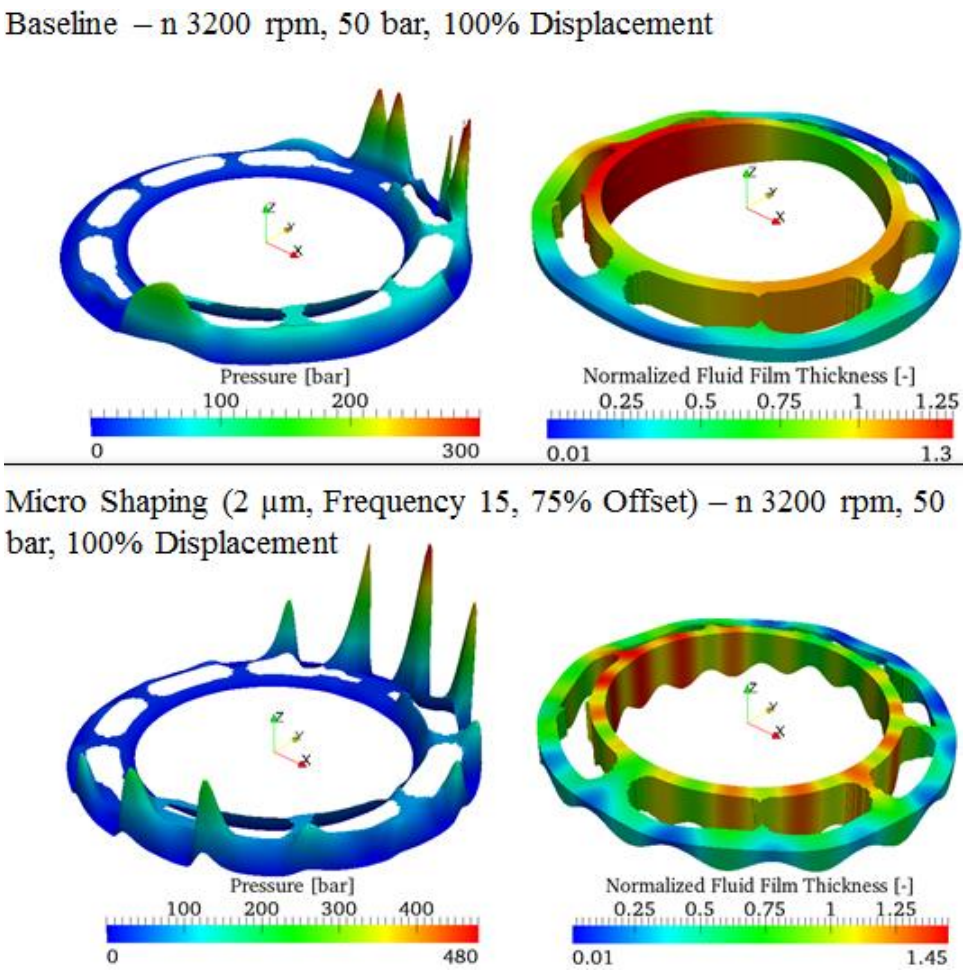

Figure 6.11. comparison between standard (top) and micro shaping (bottom, 2 µm, frequency 15, and 75% offset) at n=3200 rpm, Δp=50 bar, and β=100%; pressure (left) and fluid film thickness (right).

Figure 6.11 shows similar results to those shown in Figure 6.9, but now for operating condition 6. The additional load carrying ability of the fluid film results in a more uniform fluid film thickness. The extremely low fluid film thickness condition on the outer radius of the gap is significantly improved; thus reducing the viscous friction in the interface.

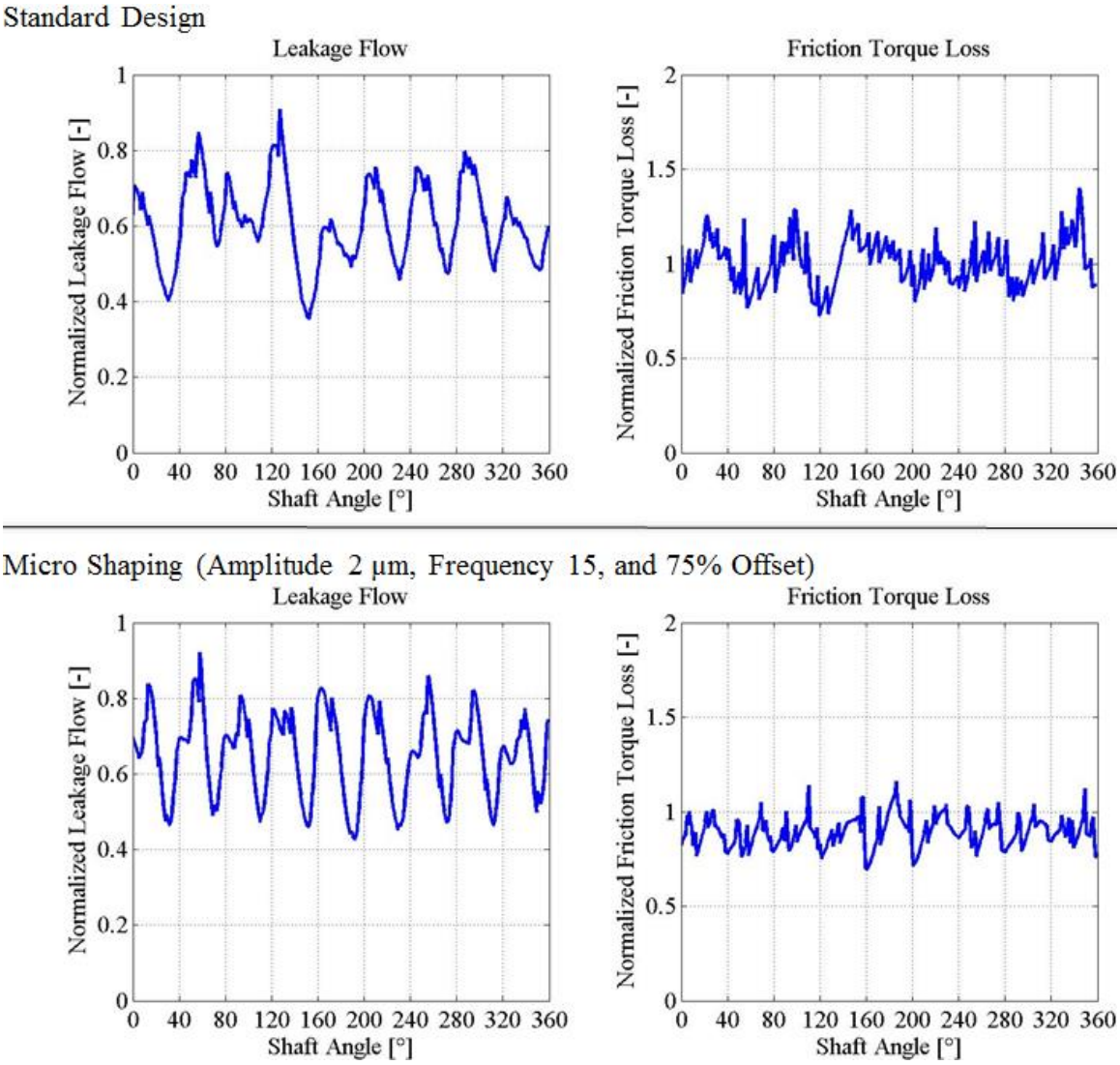

Figure 6.12. Leakage flow and friction torque loss for the standard and micro-shaping design (3200 rpm, 50 bar and 100% displacement).

Figure 6.12, differently from Figure 6.10 shows a slight increase in leakage. The friction torque loss is decreased considerably. This also can be explained with the increase of fluid film thickness on the outer edge, which reduces the torque loss. This result in a reduction of total energy dissipated in the gap of 9% relative to the baseline.

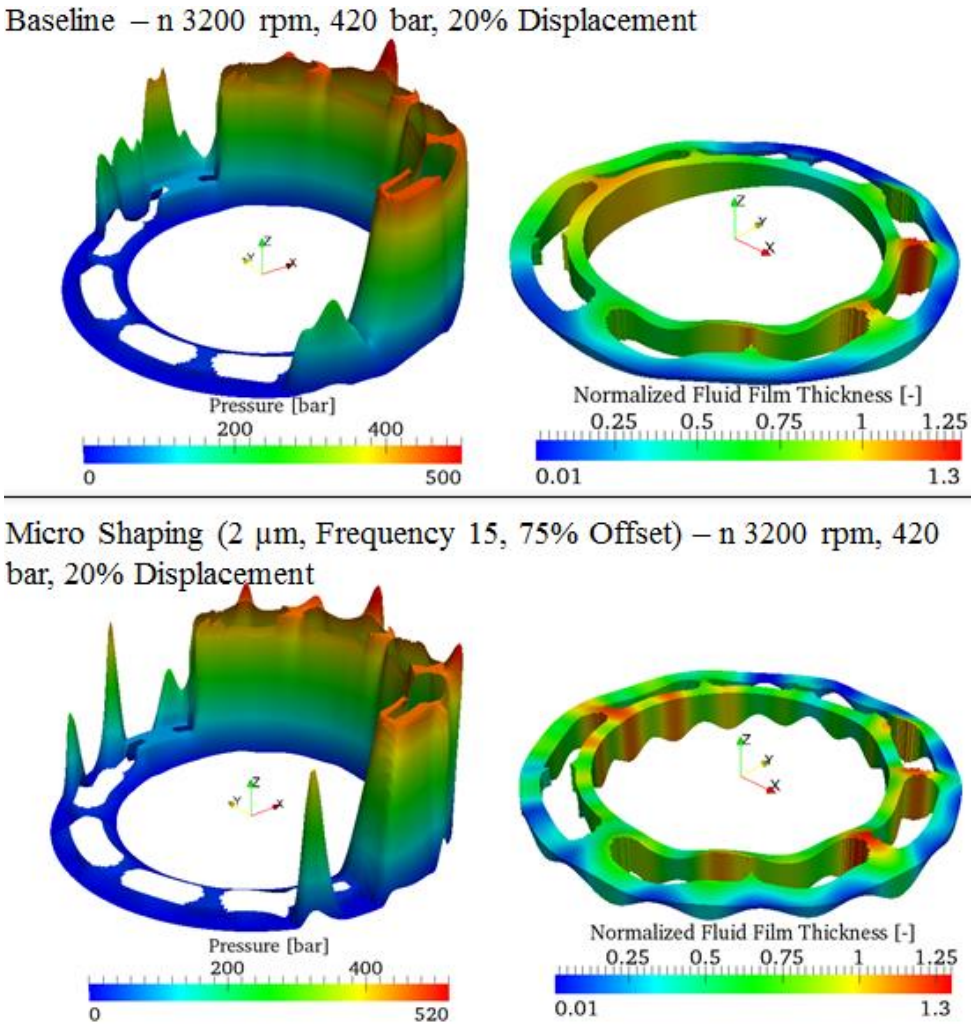

Figure 6.13. Comparison between standard (top) and micro shaping (bottom, 2 µm, frequency 15, and 75% offset) at n=3200 rpm, Δp=420 bar, and β=20%; pressure (left) and fluid film thickness (right).

Figure 6.13 illustrates the simulation results at n=3200 rpm, Δp=420 bar, and β=20% operating condition. Additional hydrodynamic pressure is built in the gap due to the wedges introduced in the valve plate. A thicker fluid film is observed all around.

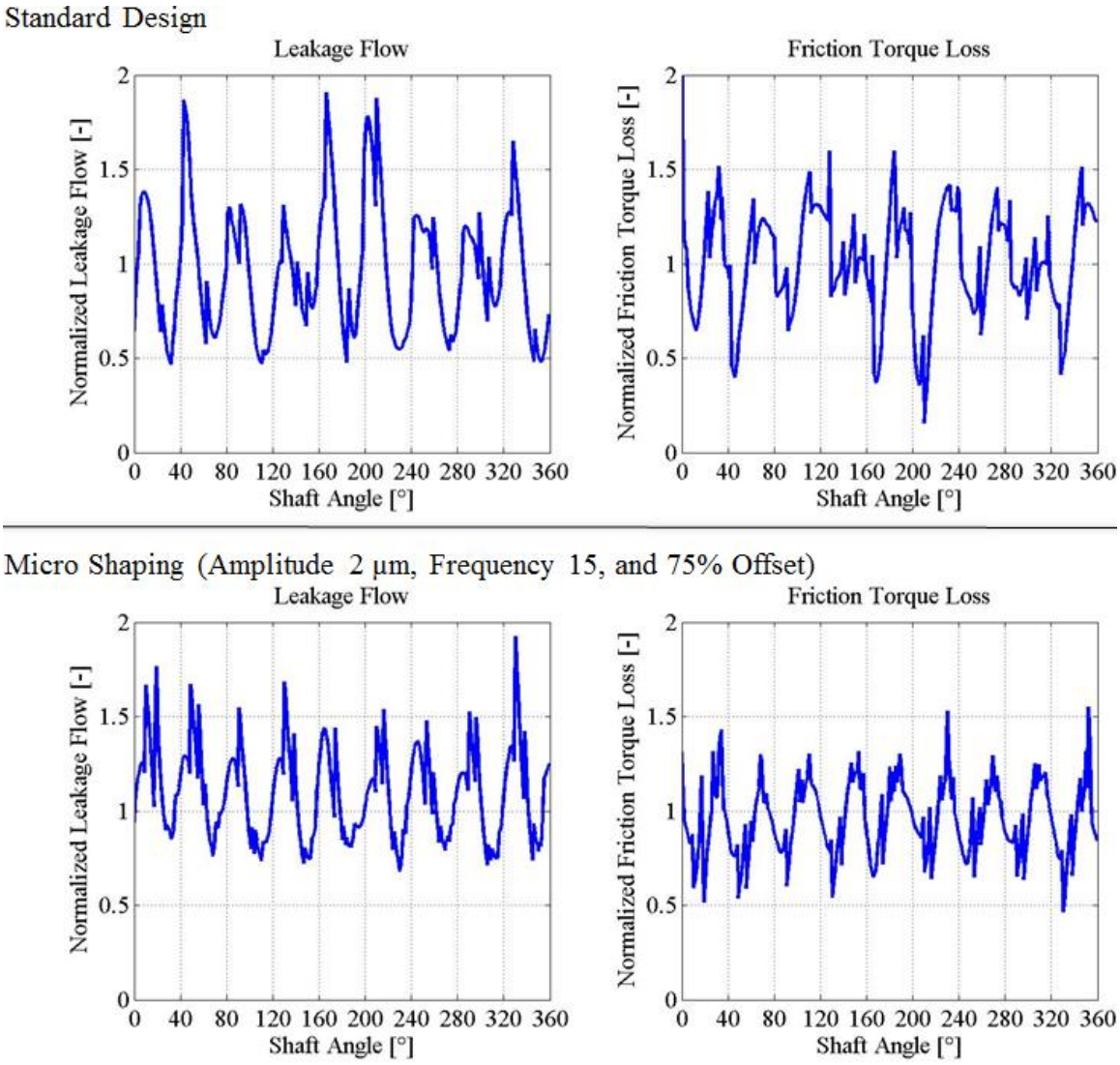

Figure 6.14. Leakage flow and friction torque loss for the standard and micro-shaping design (3200 rpm, 420 bar and 20% displacement).

Figure 6.14 shows the leakage flow and friction torque loss results of operating condition 7. The leakage flow is increased in the micro-surfaced design and the friction torque loss was slightly reduced. The increase in energy dissipation due leakage flow is larger than the reduction in energy dissipation due to the reduced viscous friction; thus resulting in a 4% increase in total energy dissipated in the fluid film.

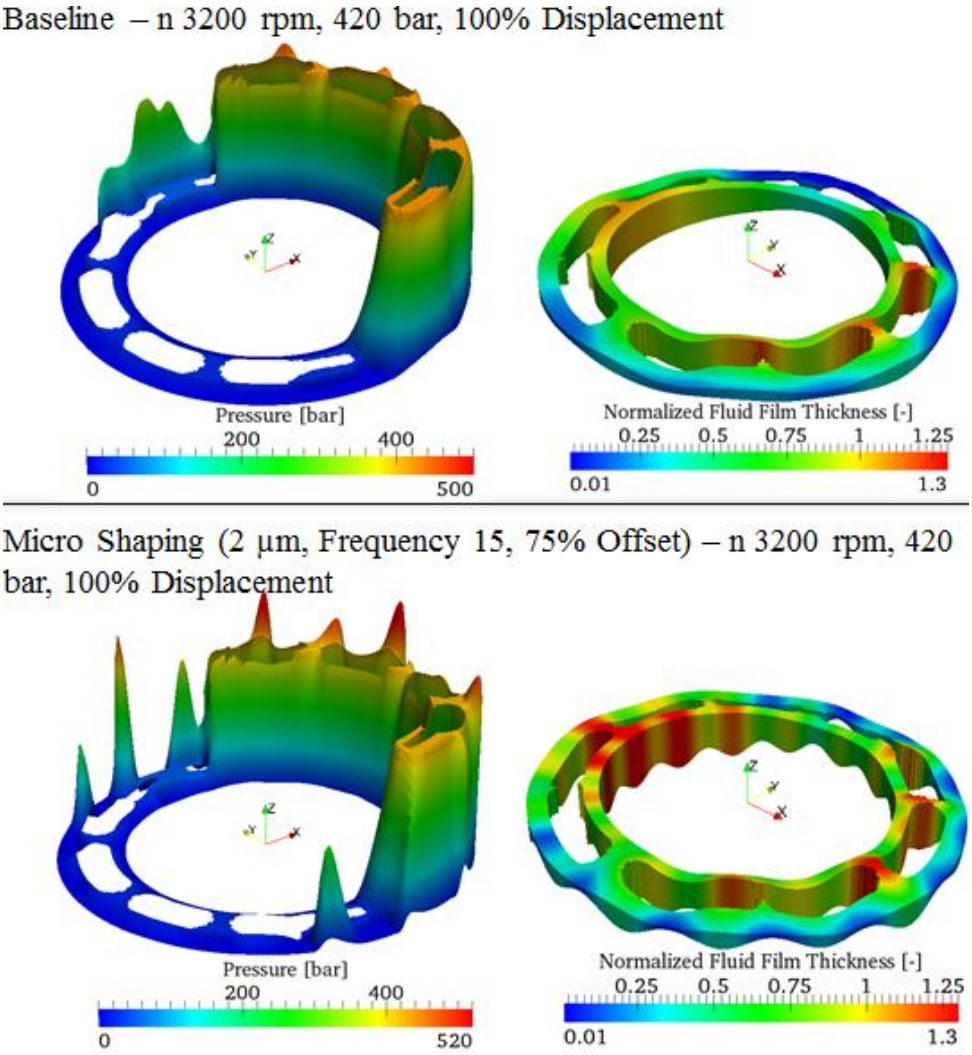

Figure 6.15. Comparison between standard (top) and micro shaping (bottom, 2 µm, frequency 15, and 75% offset) at n=3200 rpm, Δp=420 bar, and β=20%; pressure (left) and fluid film thickness (right).

Figure 6.15 represents the simulation results for operating condition n=3200 rpm, Δp=420 bar and full displacement. The hydrodynamic pressure built up is increased due to the wedging on the valve plate's surface. The fluid film thickness is significantly thicker all around in the interface although it maintains localized low fluid film thickness.

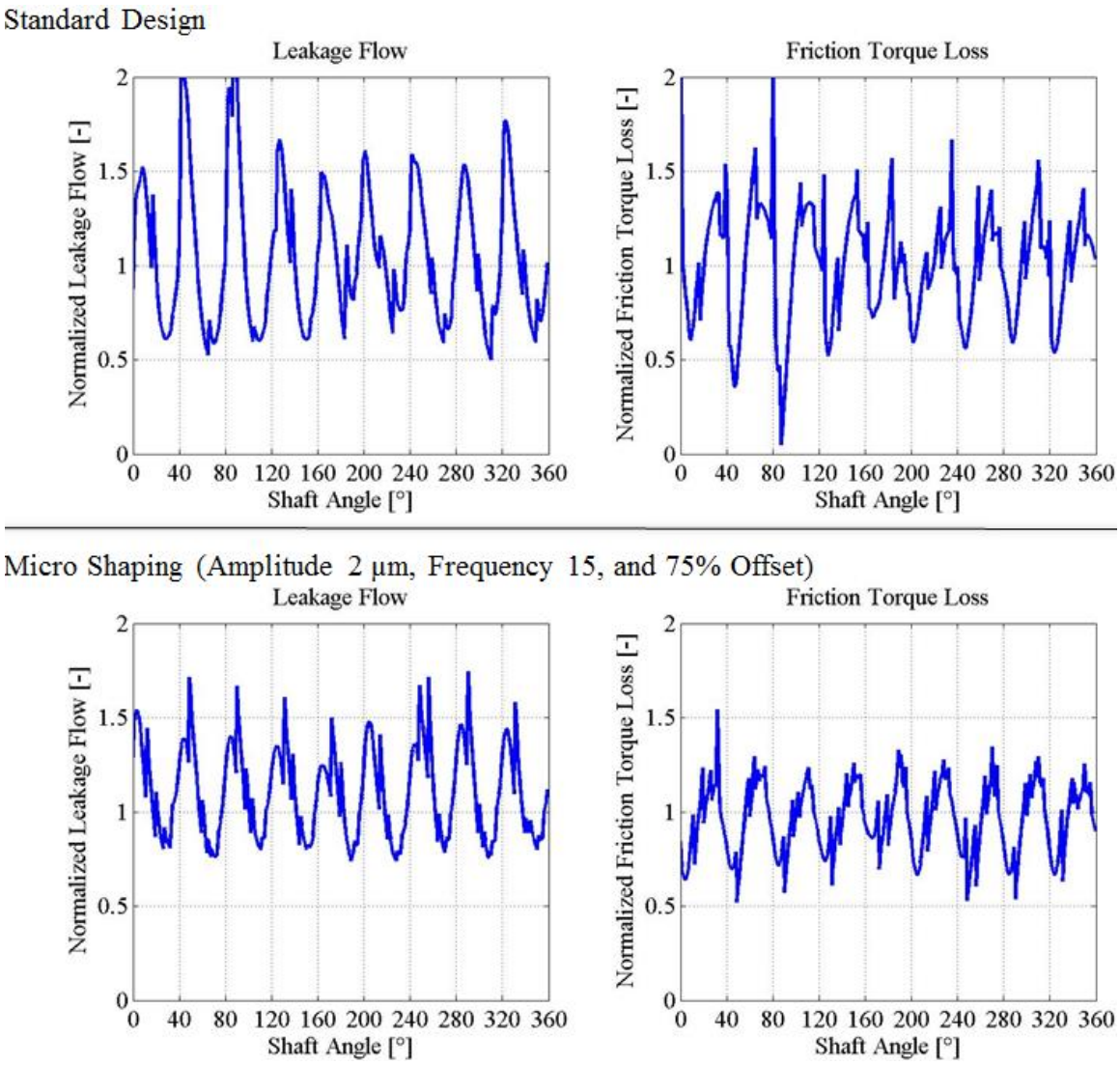

Figure 6.16. Leakage flow and friction torque loss for the standard and micro-shaping design (3200 rpm, 420 bar and 100% displacement).

Figure 6.16 illustrates the leakage and torque loss in the interface at operating condition 8. The leakage flow is slightly increase and the friction torque loss reduced by a small amount. Again, the increase of energy dissipation due to leakage flow overcomes the reduction in energy dissipation due to reduced viscous friction. This results in a 3% increase in total energy dissipation in the cylinder block/valve plate interface.

6.2 Design Space Analysis Overview

In this first section, a general overview of all the simulation results is provided for a selected number of operating conditions. The operating conditions selected to be analyzed in this section are the most representative of the general effects of the micro-surface shaping on the cylinder block/valve plate; this is why they were selected. The advantages of the micro-surfaced design will be compared against the standard (flat) design. Moreover, the limitations of this type of design will be discussed in brief.

In Figure 6.17, the simulation results for a single operating condition are shown, shaft rotational speed, 1000 rpm; pressure differential, 50 bar; and low displacement (20%). On the x-axis, the design number is displayed; this corresponds to the design number described in Table 4.1. The amplitude and offset were varied for every design. Each line in the figure represents a different frequency value; thus represents the impact of the design parameters on total energy dissipation. On the y-axis, the normalized total energy dissipation is shown; the total energy dissipation calculated was normalized against the standard design (baseline). At this operating condition, the micro-surface shaping presents the most significant positive impact on the performance of the lubricating gap. A maximum 46% reduction in total energy dissipation is seen in Figure 6.17. This was observed for design number 15 with a frequency of 10 waves.

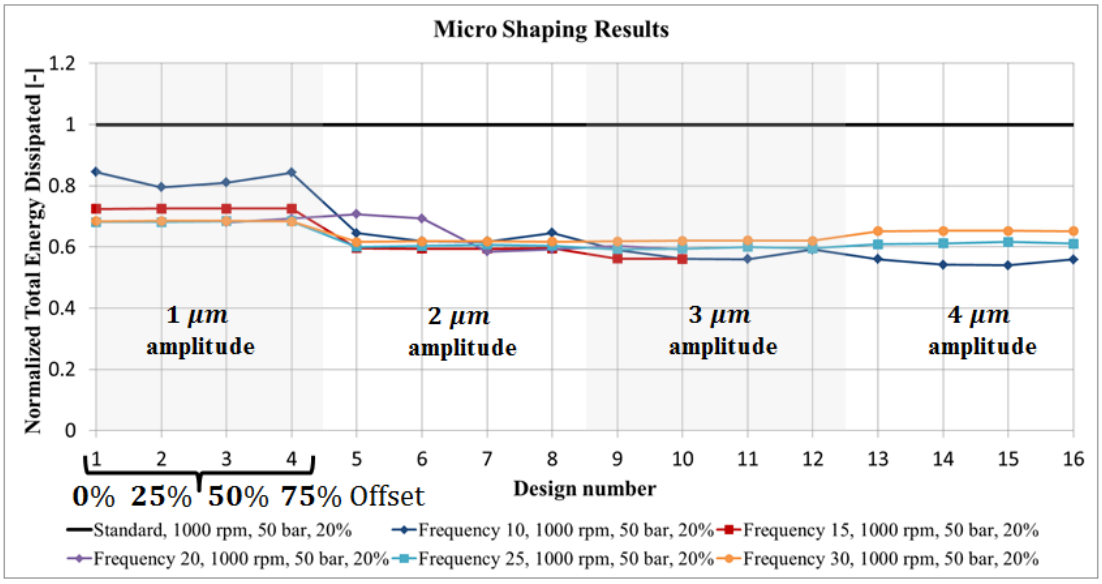

Figure 6.17. Micro-shaping results for OC 1000 rpm, 50 bar and 20% displacement.

The effects of the micro-surface shaping are of positive impact at this operating condition due to the increased load carrying capacity. This results in a thicker fluid film thickness, as mentioned, which in turn reduces the viscous friction in the gap. A slight increase in leakage is seen.

In Figure 6.18, a similar representation as in the previous figure is shown for a different operating condition, rotational speed, 3200 rpm; pressure differential, 420 bar; and full displacement. Similarly as in the previous figure the results are shown in the same manner. On the x-axis the design number and on the y-axis the normalized total energy dissipation with respect to the standard design is shown. As seen in this figure, it is shown that as the magnitude of the amplitude increases the total energy dissipation increases as well. The increase in total energy dissipation is due to the increase in leakage flow through the lubricating interface. The leakage flow is characterized by a cubic dependence to the fluid film thickness, whereas the viscous friction decreases linearly with the increase of the fluid film thickness.

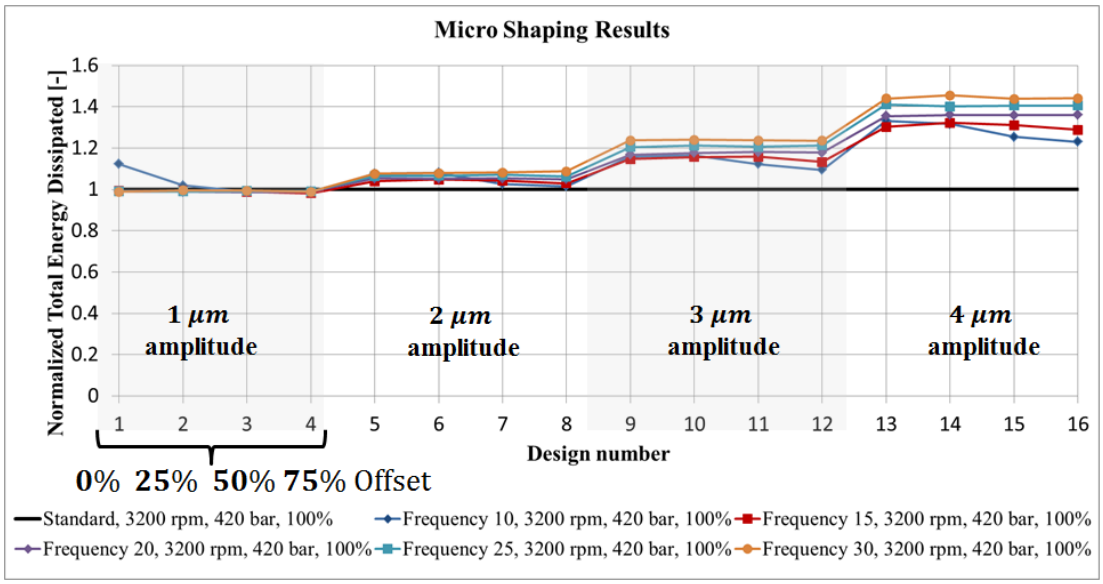

Figure 6.18. Micro-shaping results for OC 3200 rpm, 420 bar and 100% displacement.

6.3 Analysis of the Effects due to the Amplitude Parameter

In this section, an in-depth analysis of the impact of the amplitude on the fluid film thickness was performed. As shown in the previous section, the amplitude has the biggest

impact on the total energy dissipation on the cylinder block/valve plate interface due to the high sensibility of the Reynolds equation to the geometry. Simulation results are shown for the eight selected operating conditions described in Chapter 4.

In Figure 6.19, the normalized total energy dissipation is illustrated. The total energy dissipation was normalized with respect to the results from the standard design (flat surface on the valve plate), such that all the values where in the same order of magnitude. On the x-axis, the operating conditions are labeled, these correspond to the operating conditions described in Table 4.2. On the y-axis, the normalized total energy dissipation is shown. Each bar represents a different design varying the amplitude magnitude. The first one, is the standard design (blue bar); the second, sinusoidal wave with an amplitude of 1μm; and the following increment in steps of 1μm. For this analysis, the other two design parameters, the frequency and offset, were held fix (Frequency 15 and Offset 75%). These parameters were fixed at these parameters since they represent a good compromise between the total energy dissipation reduction and leakage increment at high pressure operating conditions. As mentioned in the previous section, the total energy dissipation reaches up to a maximum of 45% reduction at the operating condition: low rotational speed, low pressure differential and low displacement (1000rpm, 50 bar and 20% displacement). On the other hand, the total energy dissipation increases as the amplitude increases at high pressure differential of operation.

The sinusoidal wave aids the load carrying capacity of the interface by introducing an additional generation of pressure via hydrodynamic effects due to the wedge effect.

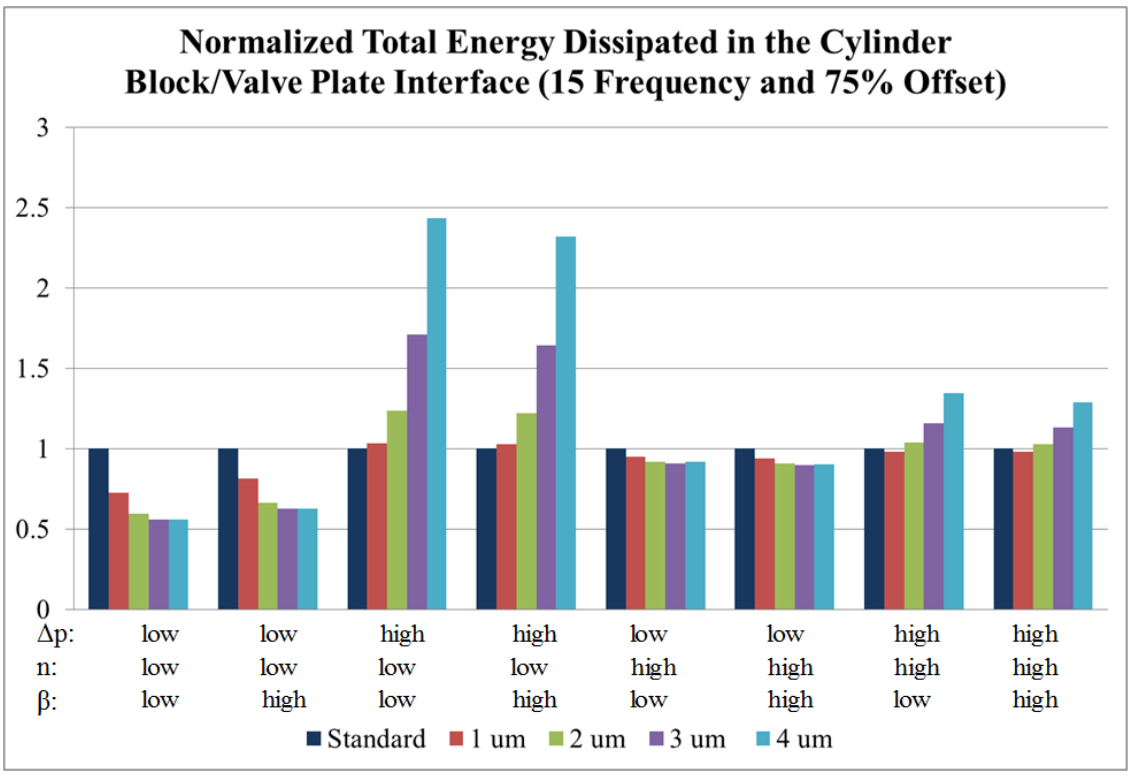

Figure 6.19. Sinusoidal wave amplitude effects on the total energy dissipation.

The increase of energy dissipation at the higher pressure differential operating conditions is explained by the increase in leakage flow over the cylinder block interface, while the reduction of the viscous friction is not in the same order of magnitude. The cubic dependence to the fluid film thickness of the leakage can be clearly seen in the Figure 6.20.

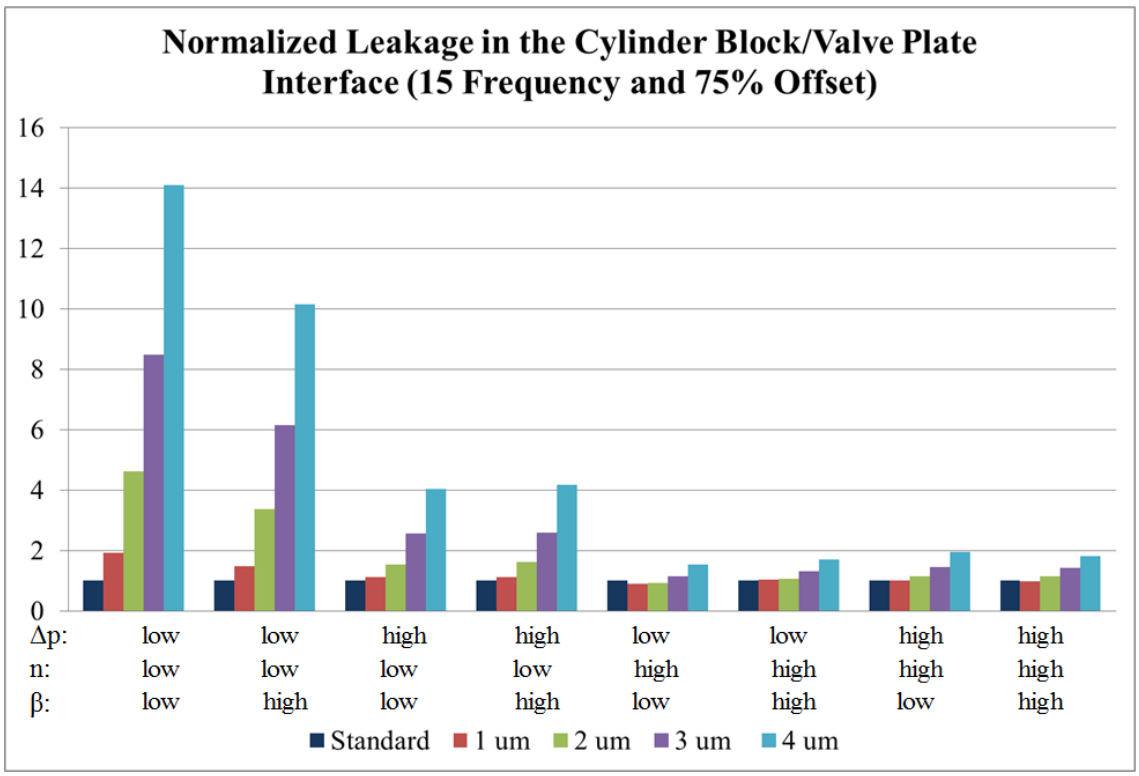

Figure 6.20. Sinusoidal wave amplitude effects on the leakage flow.

As presented in the figure above, the leakage increases for all the operating conditions. This is explained by the direct modification of the fluid film thickness geometry via the introduction of the micro shaping in the running surface. The leakage flow is a result of a thicker fluid film thickness, which is desired at low operating pressures.

6.4 Analysis of the Effects of the Frequency Parameter

The frequency parameter, as described in Chapter 4, defines the number of waves in the circumferential direction of the valve plate. This parameter is analyzed meticulously in this section. The effects on the total energy dissipation are reflected in the Figure 6.21. The operating conditions are labeled on the x-axis and the normalized energy dissipation with respect to the standard design is shown in the y-axis. Each bar represents a different design by modifying the frequency (number of waves) on the surface, and by holding fix the amplitude and offset. In this case, the amplitude is held at 2 μm and the offset at 75%. The reason for the selected parameters is the same as in the previous section; it represents

the best compromise between total energy dissipation reduction at low pressure operating conditions and leakage at higher pressure differentials.

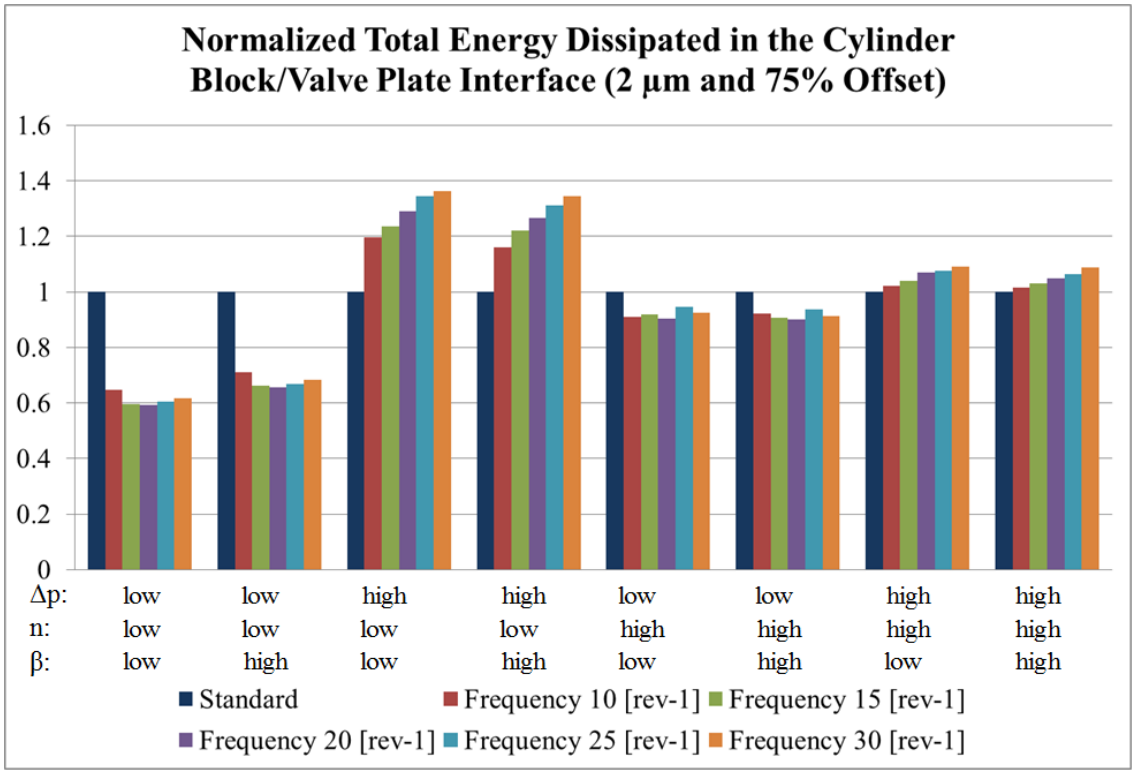

Figure 6.21. Normalized total energy dissipation varying the frequency parameter.

In Figure 6.21, the effect of the frequency on the energy dissipation is shown. At low pressure operating conditions the frequency of 15 decreases the total energy dissipation compared to the frequency of 10. There is no decrease of total energy dissipation as the magnitude increases after a frequency of 15; on the contrary, it increases the total energy dissipation. At higher pressure operating conditions, the total energy dissipation increases as the magnitude of the frequency increases. The best compromise comes from frequency of 15, since it achieves a high total energy dissipation reduction at low pressures and only a slight increase in total energy dissipation at high pressure operating conditions.

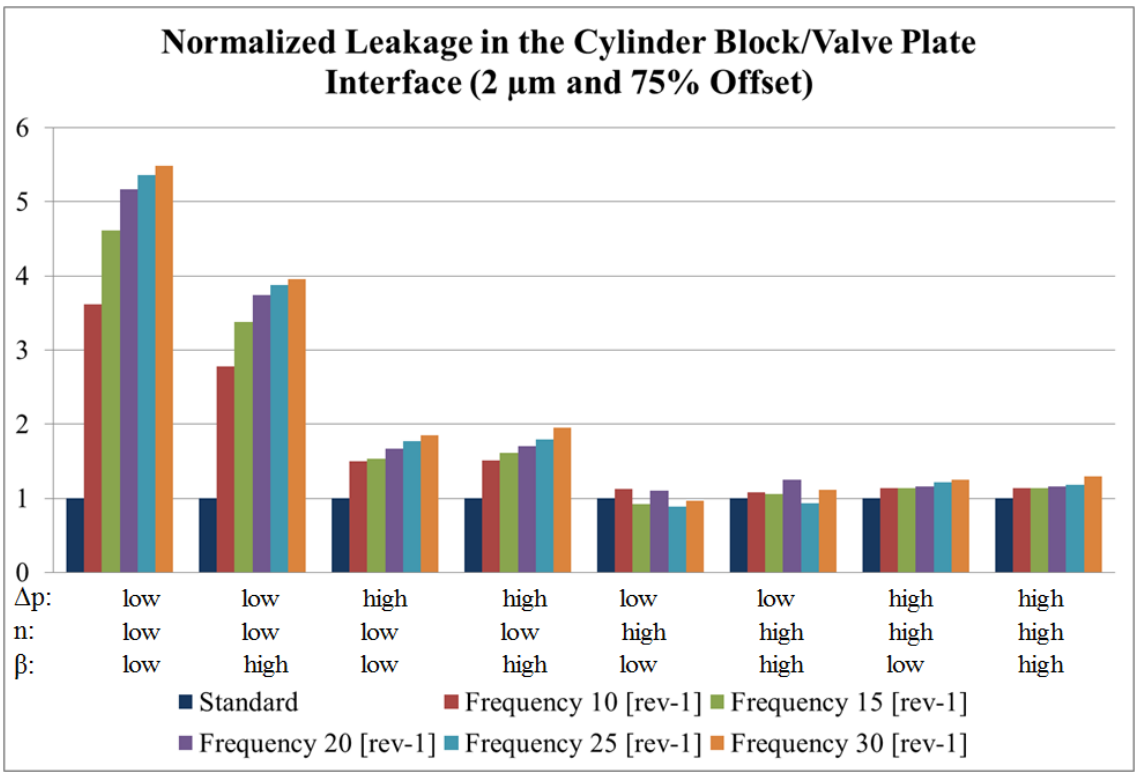

Figure 6.22. Normalized leakage flow varying frequency.

The results in Figure 6.21 can be well explained by the results displayed in Figure 6.22. Figure 6.21, illustrates the normalized leakage flow in the cylinder block/valve plate interface while varying only the frequency of waves on the circumferential direction. Operating conditions are labeled in the bottom axis and normalized leakage on the vertical axis. The leakage flow increases with increasing magnitude of the frequency, except at the operating condition of low pressure and high speed for both; low and high displacement.

6.5 Analysis of the Effects of the Offset Parameter

In this section, the offset parameter effect on the lubrication between the valve plate and the cylinder block is studied. The offset, defines the starting point of the sine wave as defined in Chapter 4. This is the first time that such parameter is studied in the influence of the sinusoidal wave on the performance of the lubricating gap. The purpose of this was

to further understand how the waviness pattern influences the behavior of the fluid film and learn if such parameter had an impact at all.

The normalized total energy dissipation with respect to the standard is displayed in Figure 6.23, Figure 6.24 and Figure 6.25. The operating conditions are labeled on the bottom axis and the normalized energy dissipation is displayed on the vertical axis. The amplitude parameter is held constant at 2 µm, since it is the best compromise between power loss reduction and increase in leakage at high operating conditions. The effect due to the change in the offset is displayed for three different frequencies; 10, 15 and 20 waves on the circumferential direction, in Figure 6.23, Figure 6.24 and Figure 6.25, respectively.

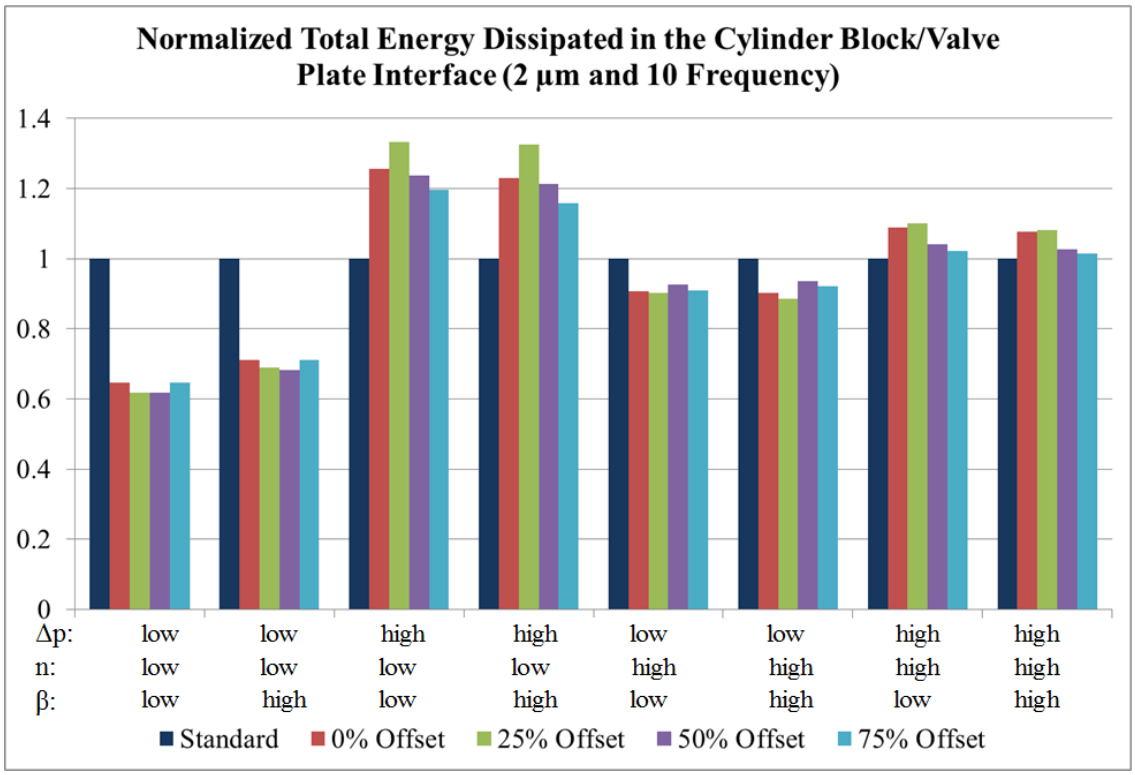

Figure 6.23. Normalized total energy dissipation varying offset.

In Figure 6.23, the offset has a large impact on the total energy dissipation, with frequency 10. This impact is larger at the high pressure operating conditions, from this

results it is clear that the 75% offset is the best across the board being the one with lowest energy dissipation at high pressure operating conditions.

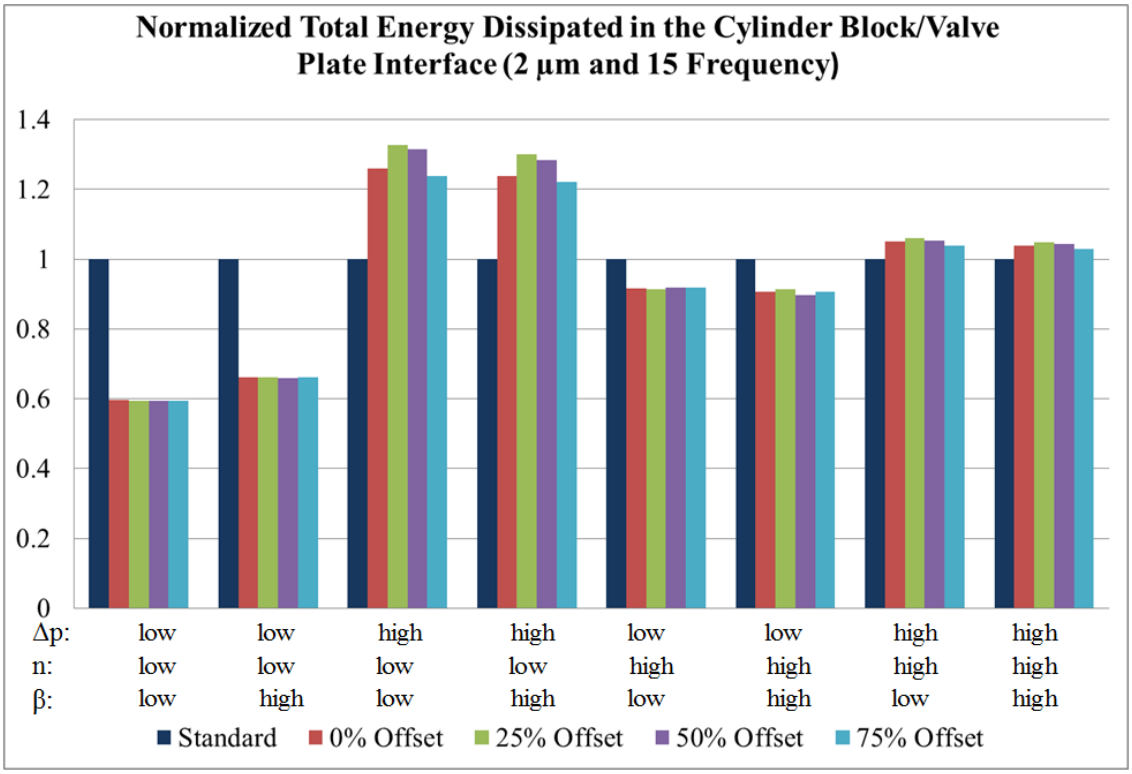

Figure 6.24. Normalized total energy dissipation varying offset.

In Figure 6.24, the offset has a significant impact on the total energy dissipation, with frequency 15. This impact is larger at the high pressure operating conditions, from this results, as in the previous result, it is clear that the 75% offset is the best across the board being the one with lowest energy dissipation at high pressure operating conditions.

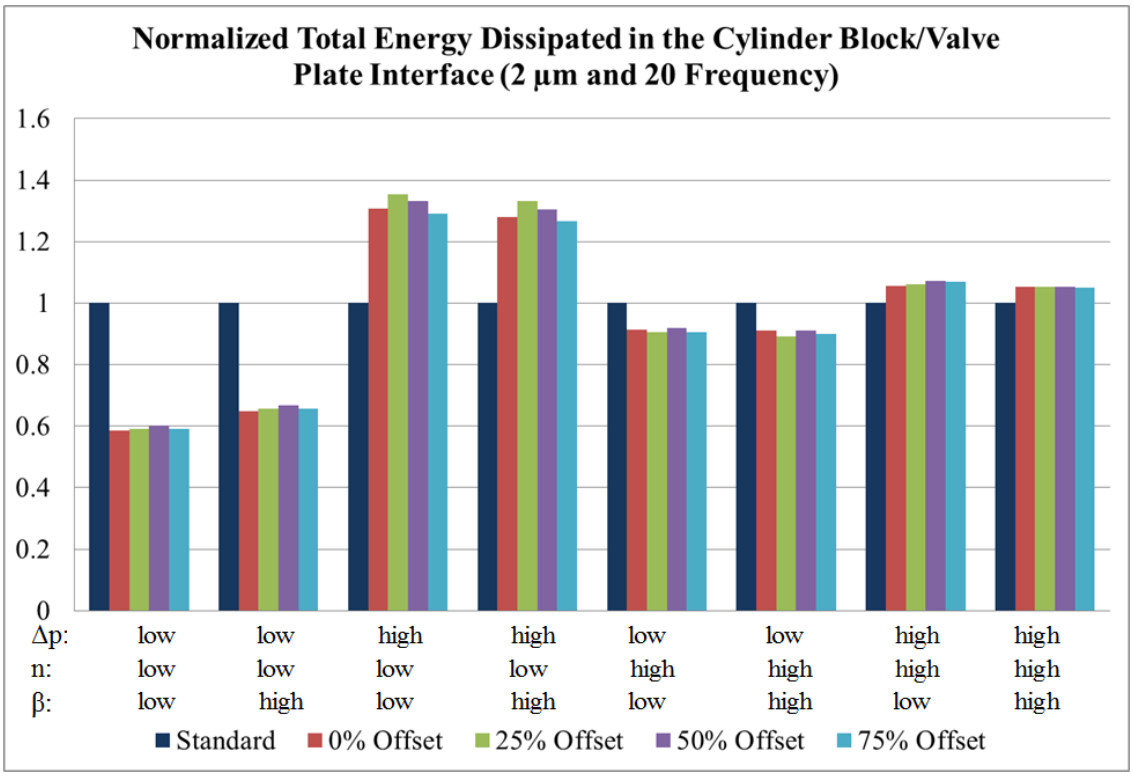

Figure 6.25. Normalized total energy dissipation varying offset.

In Figure 6.24, the offset does not have a significant impact on the total energy dissipation, with frequency 20. Similarly for greater frequencies, the offset loses relevance on the impact on total energy dissipation. This can be explained by the fact that at a lower number of waves, the fluid film is more sensitive in which direction the cylinder block tips toward. The cylinder block tilts during its operation. The tilt or tipping of the block depends on the operating condition. This has been proven in previous research done by Jouini (2008) and Zecchi (2013), where in separate test rigs they measured the valve plate's temperature at different points, by embedding thermocouples underneath the running surface of the valve plate. This was done in order to validate the numerical models developed by the authors to predict the performance of the cylinder block/valve plate interface. Their published measurements demonstrate that the temperature fields vary with the change in operating conditions, the temperature field is associated directly to the fluid film thickness in the gap. Zecchi (2013) matched the measured temperature fields in simulation, within a few degrees Celsius (°C). This was only possible through considering the relative motion of the block, translation on the z-

axial direction and rotation over the x- and y-axis, and elastic deformations due to pressure and thermal effects. This means the lubricating gap has localized areas of fluid film thickness at every specific operating condition. Depending on where the minimum fluid film thickness is located in the valve plate is going to determine if the offset is going to have a positive impact on the thin fluid film.

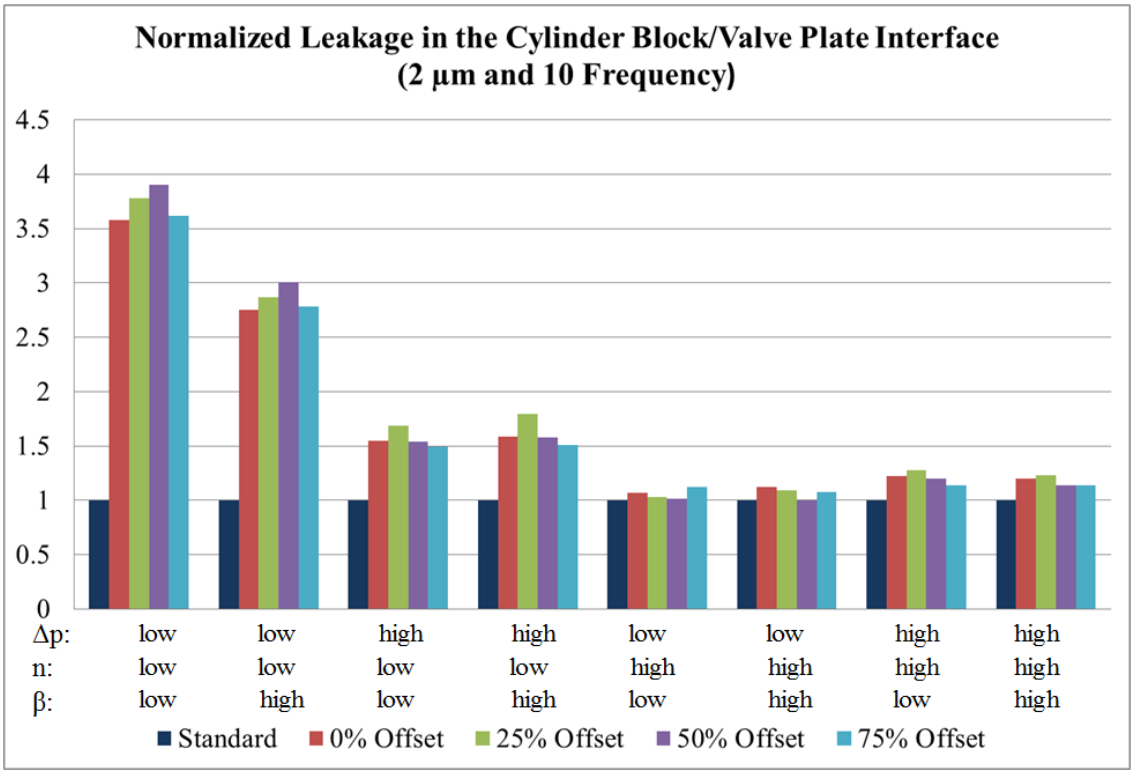

Figure 6.26. Normalized leakage flow in the cylinder block/valve plate interface varying the offset.

In Figure 6.26, illustrates the normalized leakage as the offset varies in steps of 25% for a frequency of 10. The offset has an impact on the leakage of the interface represented in the Figure 6.26. Which means that the increase in total energy dissipation represented in Figure 6.23 at high pressure operating conditions is caused by an increase in energy dissipation due to an increase in leakage flow. The difference in the leakage flow is due to the difference in positioning of the wave relative to the low fluid film thickness on the baseline design.

Figure 6.27 shows the baseline design fluid film thickness on the left, is clearly seen that the standard design presents low fluid film thickness near the outer dead center. and on the right multiple designs for varying offsets. As seen the fluid film thickness values are different between each design. On the right the same color scale is shown in order to make more apparent the differences in fluid film thickness. The z-x and z-y cross sections are shown for every design with the waved patter introduced on the valve plate. The design with 75% offset shows the lowest average fluid film thickness in the cross sections, especially if compared against the 0 and 25% offset designs. These results correspond to what was previously shown in Figure 6.26, a lower leakage for the 75% offset design.

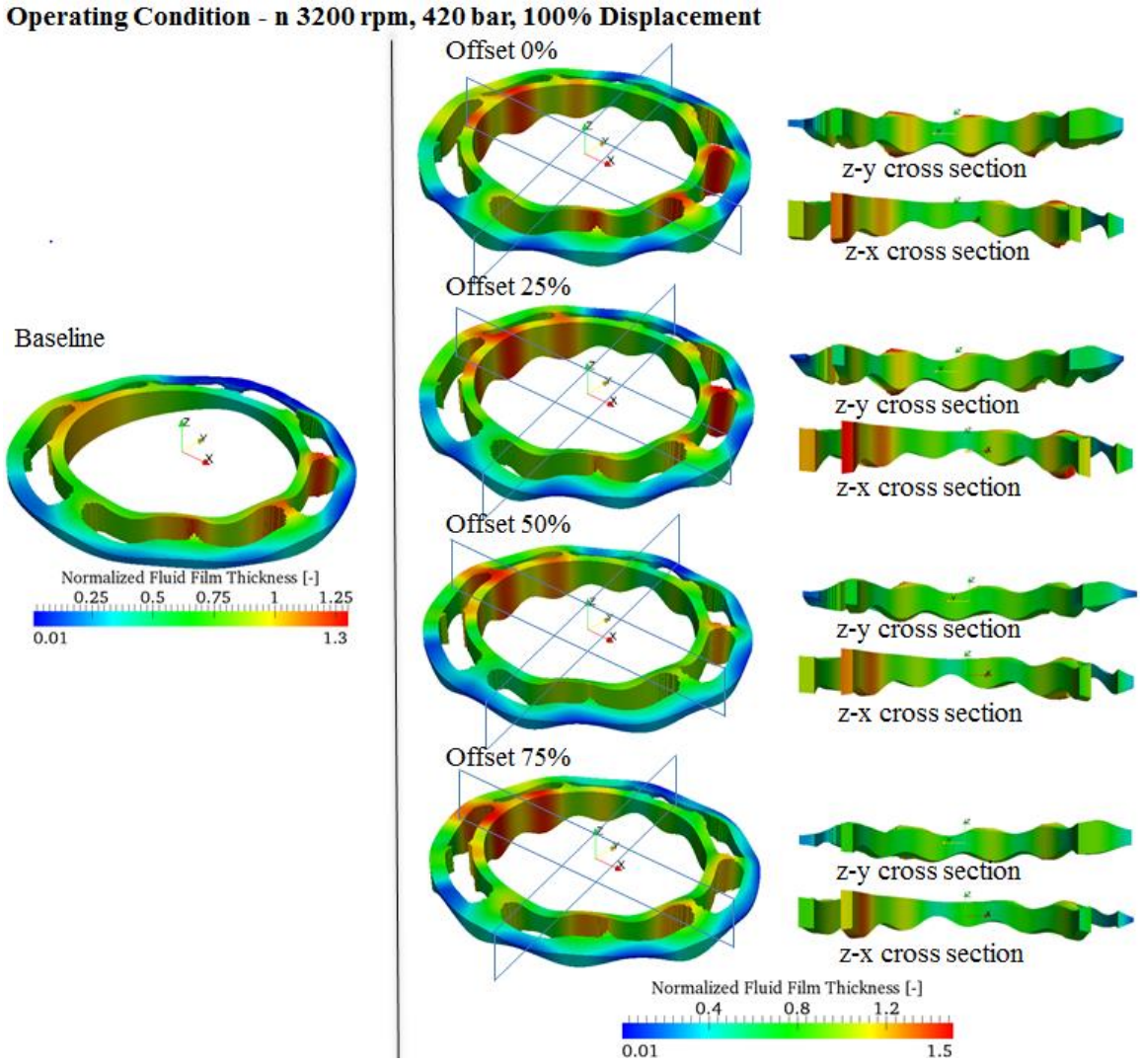

Figure 6.27. Comparison for different offset values (at 3200 rpm, 420 bar and full displacement).

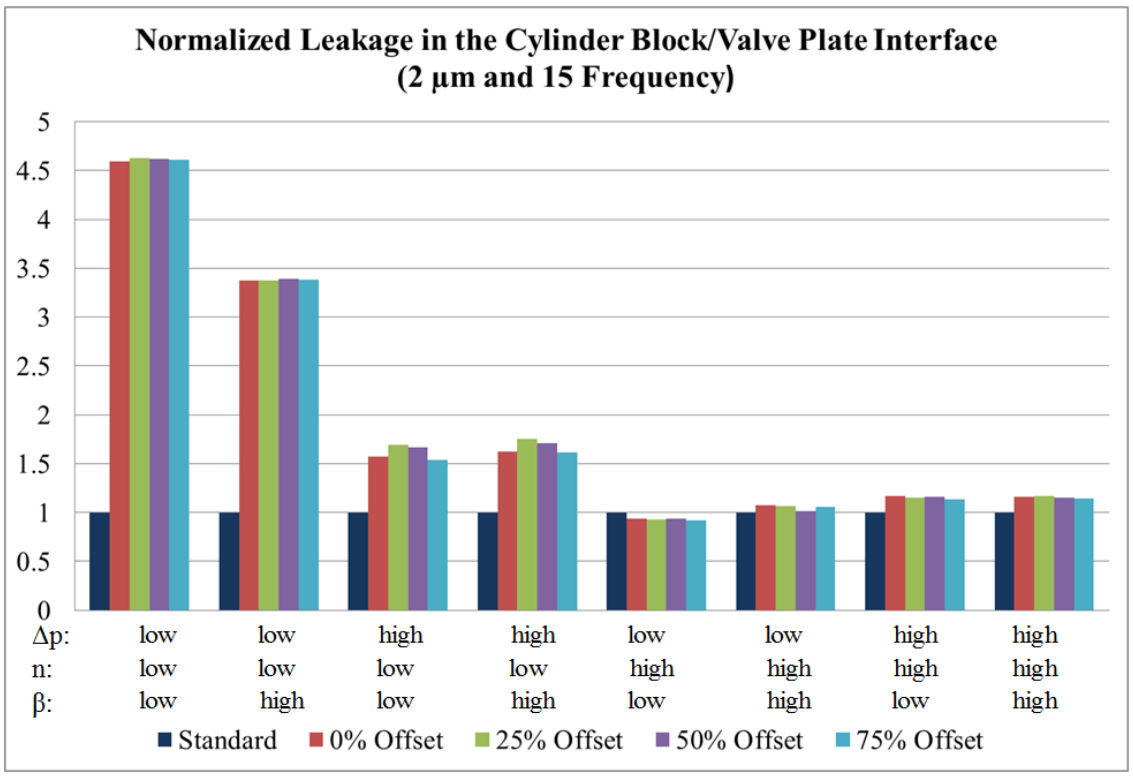

Figure 6.28. Normalized leakage flow in the cylinder block/valve plate interface varying the ofsset.

In Figure 6.28, the normalized leakage flow is shown for a frequency of 15. The offset doesn't have a significant impact on the leakage of the interface represented in the Figure 6.28. Which means that the increase in total energy dissipation represented in Figure 6.24 comes solely from an increase in viscous friction due to the different location of the peaks and valleys of the wave in the valve plate. The difference on the fluid film shape is better illustrated in the following figures.

CHAPTER 7. MICRO-SURFACE SHAPING ON THE CYLINDER BLOCK

7.1 Overview and Purpose

In this Chapter, the sinusoidal wave is introduced to the cylinder block's running surface instead of applying it on the valve plate. The purpose of this chapter is to investigate the advantages of introducing the micro-surface shaping on the cylinder block. The micro-surface shaping pattern on the cylinder block should have a different effect on the fluid film behavior than the one applied on the valve plate; because, of the elastic deformation caused by the pressure in the displacement chambers. As shown previously in the Chapter 3, is represented in Figure 7.1 when the inside of one displacement chamber is loaded with a reference pressure of 100 bar.

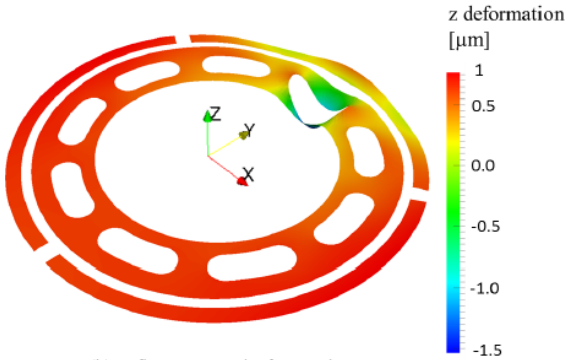

Figure 7.1. Deformation of the cylinder block surface due to pressure in a single displacement chamber (Zecchi, 2013).

The surface deformation of the cylinder block is a physical phenomenon that occurs during the normal operation of the machine. It creates a wavy profile on the high pressure side of the cylinder block, as mentioned in Chapter 5 this introduces an additional

generation of pressure due to the wedge effect. An example of the deformation of the cylinder block's running surface is shown in Figure 7.2.

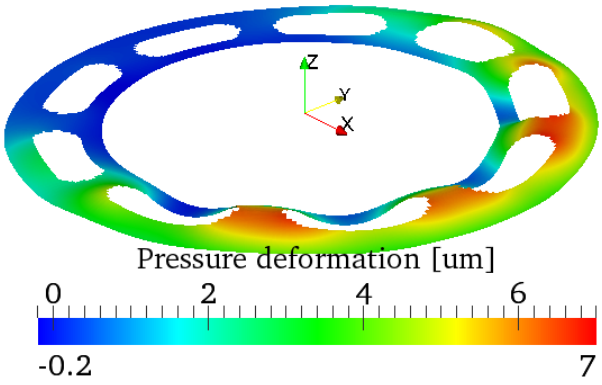

Figure 7.2. Pressure deformation of the cylinder block surface (3200 rpm, 420 bar and full displacement).

The idea of applying the sinusoidal wave on the cylinder block, is basically to apply the inverse sine wave of how the cylinder block deforms due to the pressure inside the displacement chamber. A visualization of this is shown in the following Figure. Additionally, an example of how the fluid film thickness would be shaped without elastic deformations or relative motion of the cylinder block is shown in Figure 7.4.

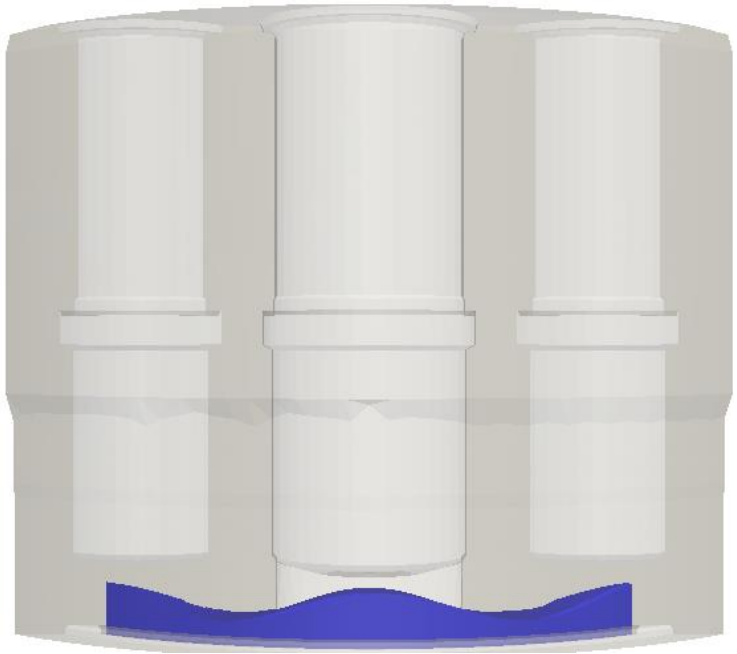

Figure 7.3. Cross section of the cylinder block and micro surface shaping representation (Scale x1000).

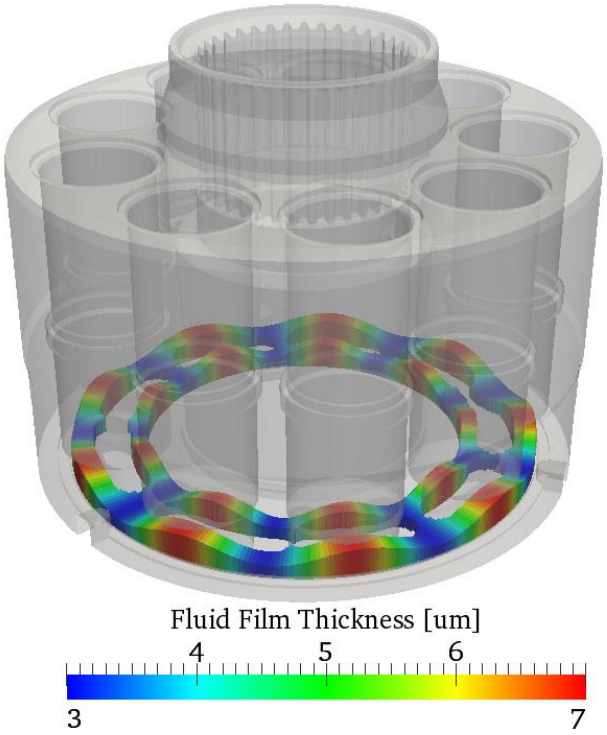

Figure 7.4. Fluid film thickness example with a 2 μm amplitude, 9 frequency and 10° or 25% offset (No Tilting and No Elastic Deformations on Both Solids).

The advantage, of the shaping on the cylinder block, would be that the shape of the fluid film would become pressure dependent. In the previous Chapter, it was noted that the sinusoidal wave can increase the total energy dissipation at high pressure operating conditions, due to the increase leakage flow in the interface. If the elastic pressure deformation cancels out the micro-surface shaping the fluid film thickness should be minimized thus reducing the leakage flow.

7.2 Simulation Results and Analysis

In this section, the simulation results for the micro-surface shaping on the cylinder block are analyzed in-depth. The purpose is to investigate if the shaping on the cylinder block has any advantages over the application of the micro-surfaced shaping on the valve plate, by making the fluid film geometry pressure dependent.

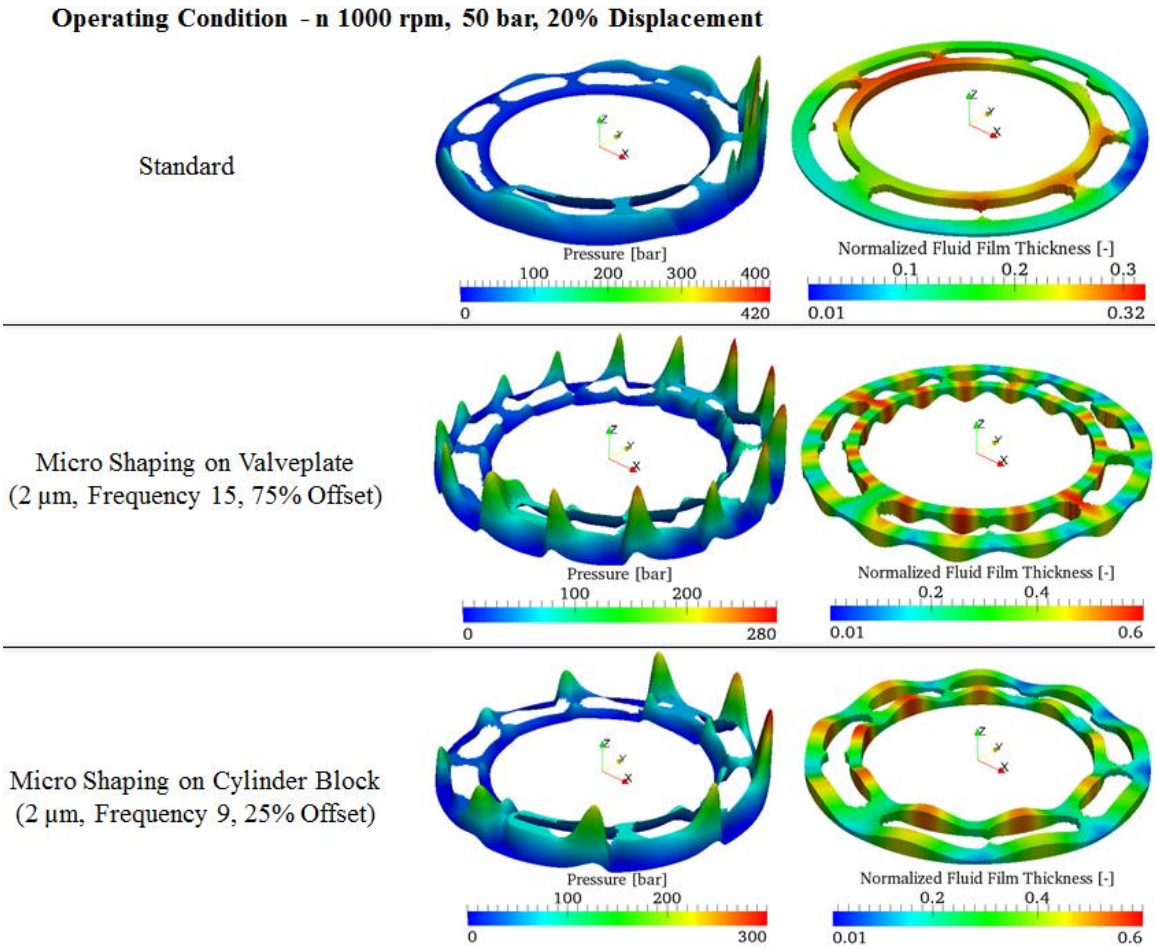

Figure 7.5. Pressure and fluid film thickness for the standard, micro shaping on valve plate and micro shaping on cylinder block (1000 rpm, 50 bar, 20% displacement).

The Figure 7.5 shows the pressure and the fluid film thickness for the baseline, waved valve plate and waved cylinder block at 1000 rpm, 50 bar and 20% displacement. The additional hydrodynamic pressure built up in the gap is evident for both waved designs. The number of waves in the gap is also seen in the number of additional pressure spikes observed. In the case of the valve plate a design with 15 waves is shown, whereas on the cylinder block only 9 waves were introduced (same number of displacement chamber in the cylinder block). The additional hydrodynamic pressure on the waved valve plate also corresponds to a higher load carrying capacity which also results in a higher reduction in total energy dissipation (40%). The waved cylinder block has an increase load carrying capacity compared to the baseline but only achieves 35% reduction in total energy dissipation relative to the baseline.

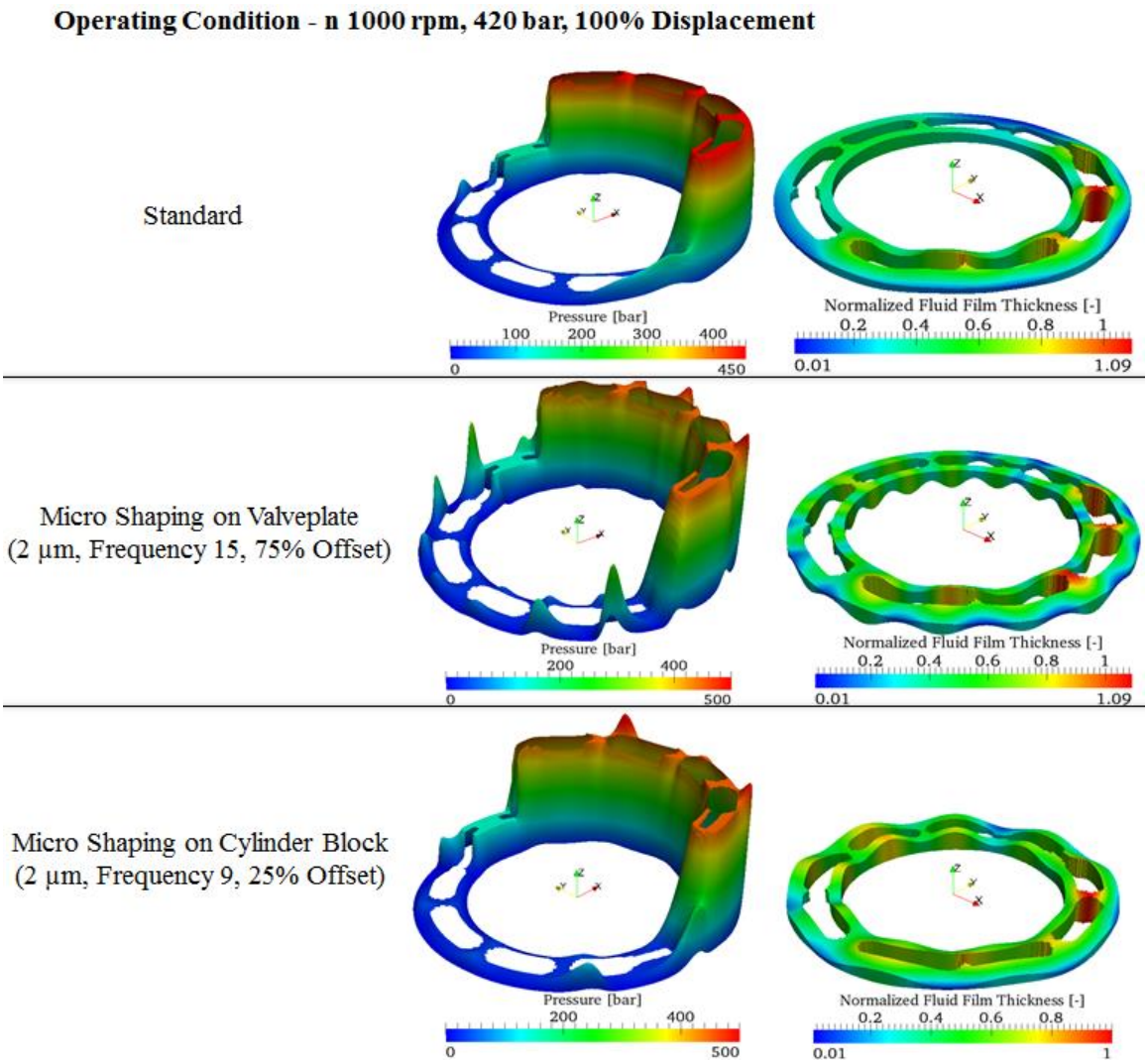

Figure 7.6. 3D Pressure and fluid film thickness representation (1000 rpm, 420 bar and full displacement).

In Figure 7.6, shows the pressure and fluid film thickness for 1000 rpm, 420 bar and full displacement. Similarly as in the previous operating condition, additional hydrodynamic pressure is present. The major difference between the previous operating condition (low pressure) and this one (high pressure) is the fluid film thickness shape on the waved cylinder block design. The waves on the high pressure side are less evident if compared to the waved valve plate. This will result in a lower fluid film thickness average and no localized low fluid film thickness areas; corresponding to a reduction in leakage flow and friction torque loss with respect to the waved valve plate design. The waved valve plate

design increases by 22% the total energy dissipation in the cylinder block interface, whereas the waved cylinder block raises it by 10%.

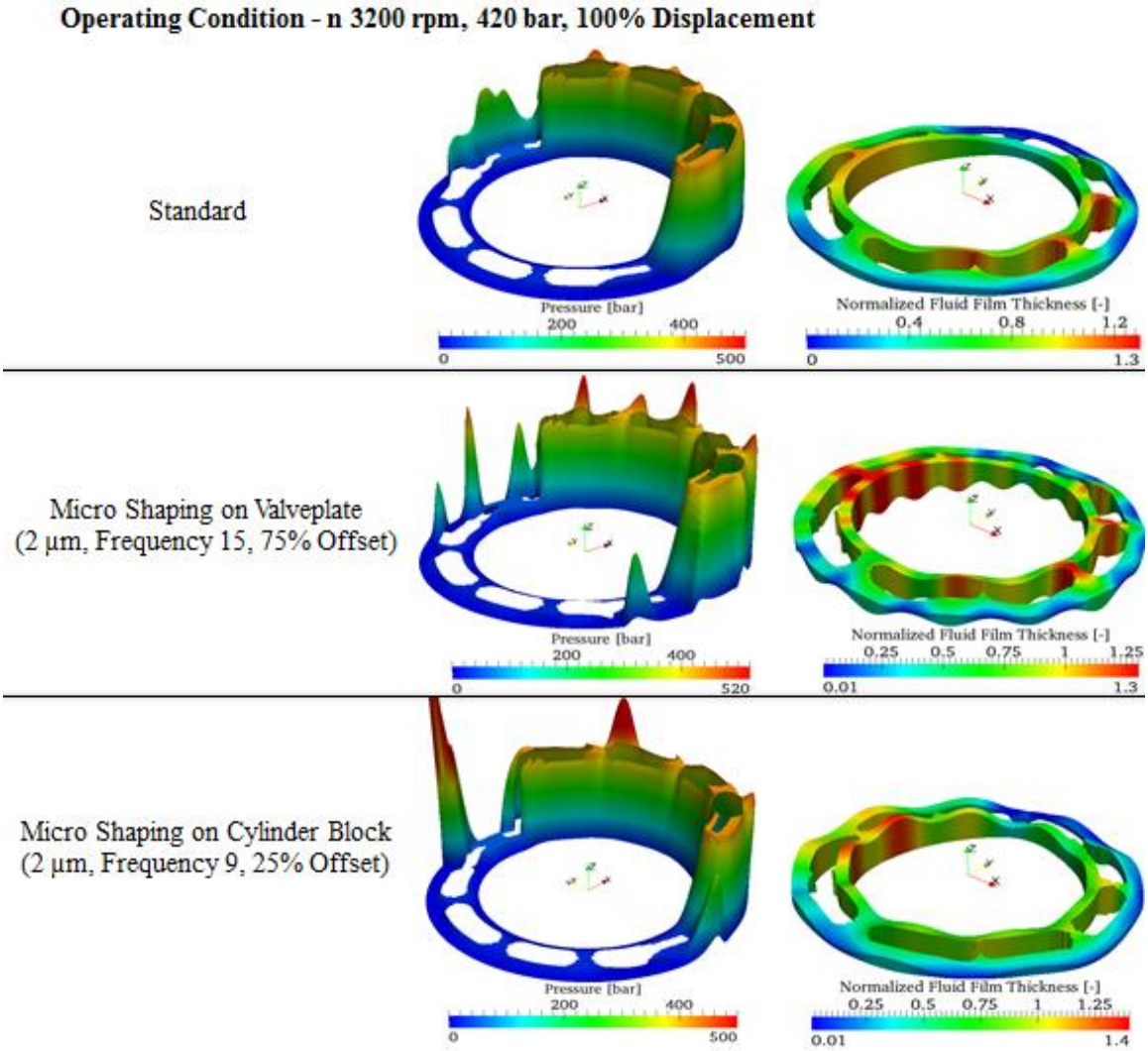

Figure 7.7. 3D Pressure and fluid film thickness representation (3200 rpm, 420 bar, 100% displacement).

In Figure 7.7, a comparison between the standard design and applying the wave on the cylinder block or on the valve plate is done by comparing the pressure and fluid film thickness in the cylinder block/valve plate interface. A similar behavior to the one previously discussed is observed. The waved geometry is almost not distinguishable in the waved valve plate, whereas the waved valve plate is clear. As mentioned before, this results in reduced leakage flow and less viscous friction, since the average fluid film thickness is lower and the localized low fluid film is reduced.

The normalized energy dissipation with respect to the standard design is represented in Figure 7.8. The amplitude was varied for every design and is labeled on the horizontal axis. In the vertical axis, the normalized total energy dissipation is displayed. Three different operating conditions are shown in the figure; 1000 rpm, 50 bar and low displacement (left), and 3200 rpm, 420 bar and full displacement (right), and 1000 rpm, 420 bar and full displacement (bottom) . These operating conditions were chosen since they are the most representative of the differences between applying the wave on the cylinder block or on the valve plate surface.

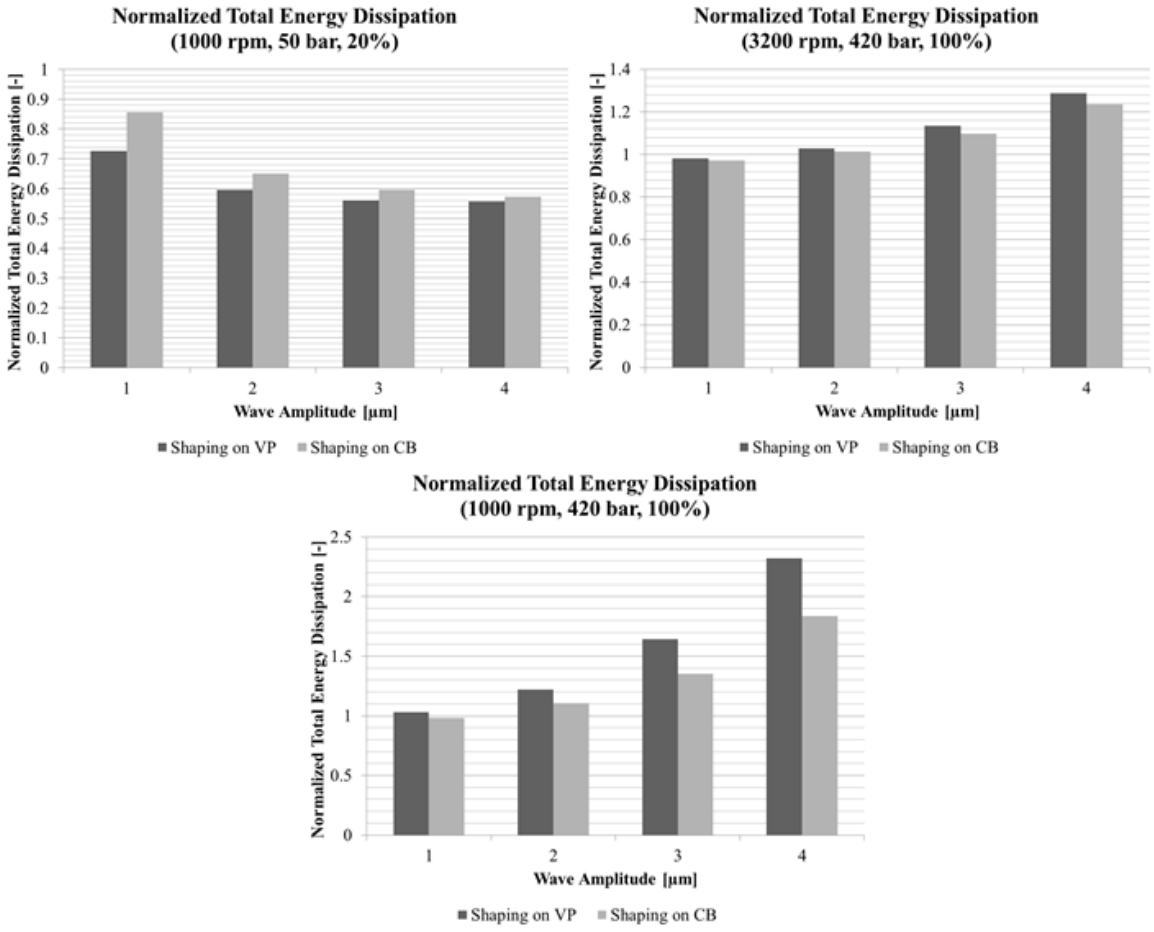

Figure 7.8. Normalized total energy dissipation comparison between valve plate and cylinder block.

In Figure 7.8, the reduction in total energy dissipation is slightly less for the micro-surface applied on the cylinder block surface at low pressure operating conditions. On the other hand, the increase in total energy dissipation at higher operating conditions is

considerably lower both at high and low speeds as seen in Figure 7.8. These results can be explained with Figure 7.5, Figure 7.6, and Figure 7.7.

The simulation results shown in Figure 7.9 are for operating condition 1000 rpm, 420 bar, and full displacement. The amplitude of the wave is labeled in the bottom axis. Leakage flow and friction torque loss are shown for the waved valve plate and cylinder block. The leakage flow is consistently higher for the micro-surfaced applied on the valve plate. The friction torque loss is lower for the waved cylinder block up to amplitude of 2 µm. The waved valve plate has a larger reduction for 3 and 4 µm, but both are still comparable in magnitude. This also can be explained by previously shown figures, where the fluid film has a lower average fluid film thickness and less localized low fluid film thickness points.

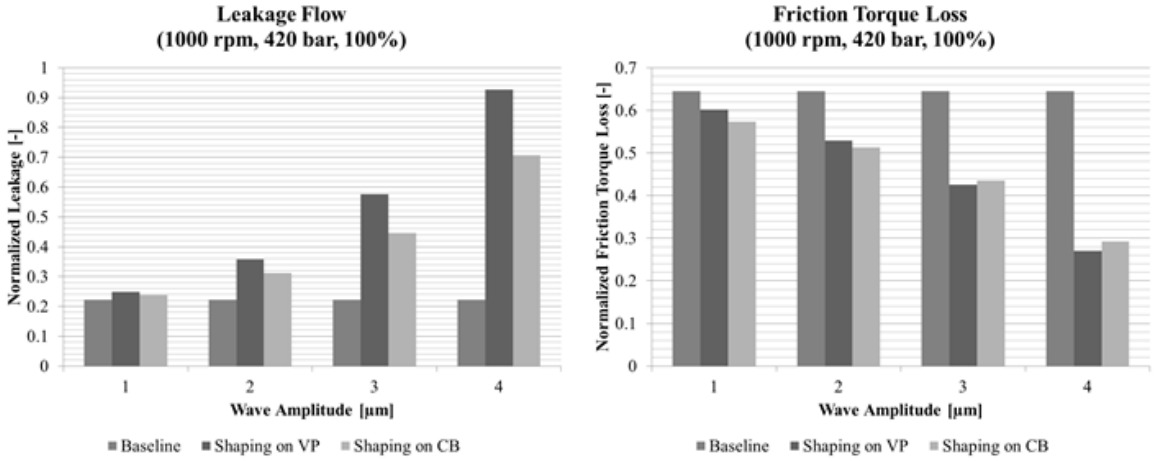

Figure 7.9. Simulation results comparison between wave on the VP or CB (1000 rpm, 420 bar, and full displacement).

In Figure 7.10, the normalized total energy dissipation with respect to the baseline design is represented for the standard, micro-surfaced valve plate (2 µm, frequency of 15 and 75% offset), and cylinder block (2 µm amplitude, frequency of 9 waves and 25% offset). On the horizontal axis the eight operating conditions selected for this thesis were labeled. Similarly as it was mentioned previously, a maximum reduction in total energy dissipation for both the waved valve plate and the cylinder block are shown; 40% and 35% respectively at low pressure, low speed and low displacement. Additionally, the waved cylinder block shows a lower increase in total energy dissipation in the cylinder

block/valve plate interface compared to the waved valve plate at high pressure operating conditions.

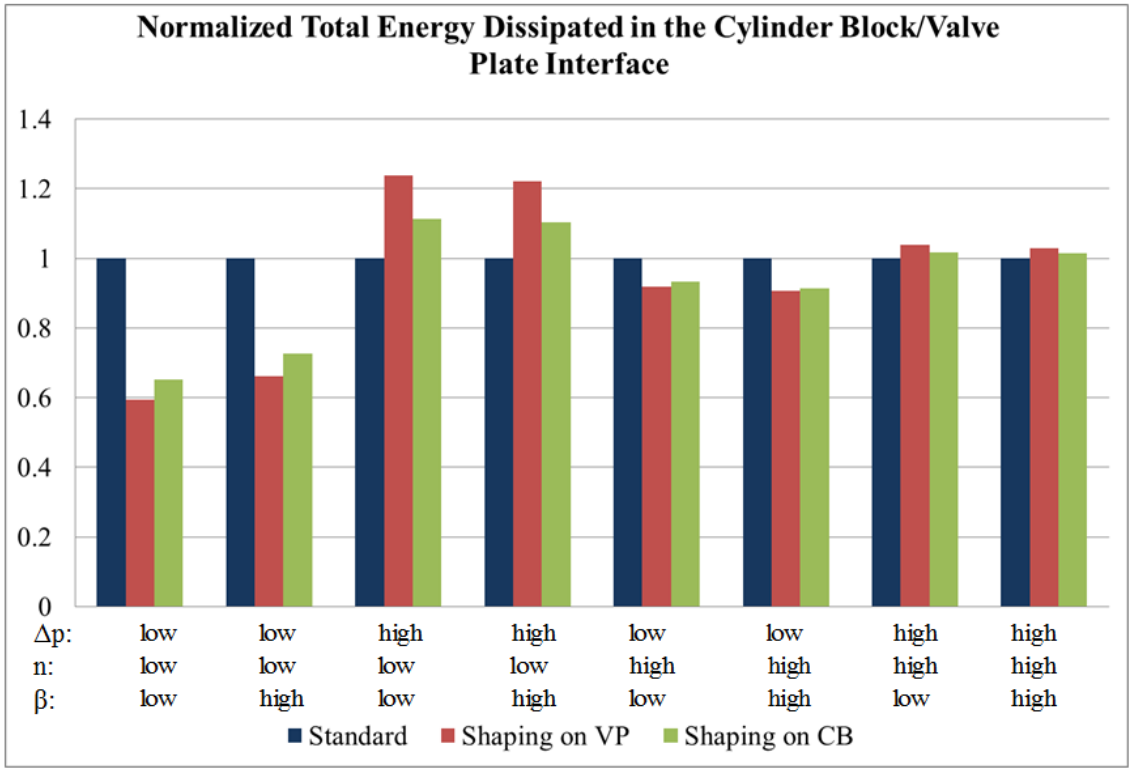

Figure 7.10. Normalized total energy dissipation in the cylinder block/valve plate interface comparison between wave on the VP or CB.

CHAPTER 8. CONCLUSIONS

The micro-surface shaping on the cylinder block/valve plate interface presents an interesting opportunity to improve the load carrying ability and to reduce the energy dissipation of the interface, therefore improving the overall performance of the axial piston machine. The design parameters, amplitude, frequency, and offset, were analyzed in-depth and the impact on the load carrying ability of the fluid film and energy dissipation are discussed and analyzed. These trends should enable improved designs in the future.

The amplitude, on the sinusoidal wave applied in the circumferential direction, is the parameter with the strongest impact on the performance of the cylinder block/valve plate interface. The Reynolds equation is extremely sensitive to film thickness changes, thus affecting the hydrodynamic pressure built up in the thin fluid film. It was found that for the range of operating conditions analyzed the given base design of 2 μm wave amplitude created the best results in reducing the total energy dissipation at low pressure operating conditions and the leakage increase at higher pressure conditions.

Moreover, the frequency (number of waves) plays an important role in the design of micro-surface shaping with a sinusoidal wave in the circumferential direction. It doesn't have a large impact on low pressure operating conditions. On the other hand, it does increase the total energy dissipation as the number of waves increase at high pressure operating conditions and will not benefit from more than a frequency of 15 at low pressure operating conditions.

These results predict up to 40% reduction in total energy dissipated in the lubricating gap at low pressure, low speed and low displacement while staying within bounds of reasonable limits of leakage increments at higher pressure operating conditions. This was achieved utilizing ±2 μm amplitude, 75% offset and a frequency of 15 waves on the circumferential direction on the valve plate surface.
Also, the offset of the wave with respect to the outer dead center of the piston was studied in this thesis for the very first time. It was found that the offset has a large impact on designs with a low number of waves (10-15) on the circumferential direction; whereas on designs with a large number of waves it doesn't have big effect. The effect has to do with the relative position of the cylinder block which is operating condition dependent, it was found that for frequencies of 10 and 15, an offset of 75% is the best compromise.

Moreover, a simulation-based comparison between the application of the micro-surface shaping, on the cylinder block or the valve plate running surface, was performed for the first time. It was found that the elastic deformation on the cylinder block due to the pressure inside the displacement chambers improves the performance of the interface compared to the waved valve plate design. It improves the performance by cancelling out the micro-surface waviness with the over imposed elastic deformation from the cylinder block. This flattens the surface thus decreasing the fluid film thickness; and reduces the leakage flow and in some case the viscous friction compared to the waved valve plate design. It can be used as a pressure dependent feature and help to improve the fluid film conditions in the entire range of operating conditions.

It was found that applying a sinusoidal wave of ±2 μm amplitude, 25% offset and a frequency of 9 waves on the cylinder block surface predicts up to 35% reduction in total energy dissipation at low pressure, low speed, and low displacement; whereas applying the shaping on the valve plate achieves a 40% reduction. On the other hand, it significantly improved the performance of the fluid film in comparison with the waved valve plate at high operating pressures. The waved valve plate (±2 μm amplitude, 75% offset and a frequency of 15) increased the total energy dissipation by ~3% at high speed,

high pressure and full displacement, but the cylinder block only increased by ~1%. Similarly at low speed, high pressure and full displacement, the waved valve plate increase the total energy dissipation by ~22%, whereas the waved cylinder block only raised it ~10%. This is explained by both lower leakage flow and lower friction torque loss, due to the more uniform shape of the fluid film. The localized low fluid film thickness conditions are reduced and the average of the fluid film thickness is reduced on the high pressure side.

LIST OF REFERENCES

LIST OF REFERENCES

Baker, J. (2008). Power losses in the lubricating gap between cylinder block and valve plate of swash plate type axial piston machines. Purdue University, MS Thesis.

Baker, J., & Ivantysynova, M. (2009). Advanced surface design for reducing power losses in axial piston machines. International Conference on Fluid Power, 10, pp. 15-30. Linköping, Sweeden.

Baker, J., & Ivantysynova, M. (2009). Power loss in the lubricating gap between cylinder block and valve plate of swash plate type axial piston machines. International Journal of Fluid Power, 10(2), 29-43.

Bergada, J. M., Davies, D. L., Kumar, S., & Watton, J. (2011). The effect of oil pressure and temperature on barrel film thickness and barrel dynamics of an axial piston pump. Meccanica, 639-654.

Bergada, J. M., Watton, J., & Kumar, S. (2008). Pressure, flow, force, and torque between the barrel and port plate in an axial piston pump. Journal of Dynamic Systems, Measurement, and Control, 011011.

Deeken, M. (2003). Simulation of the tribological contacts in an axial piston machine. O+ P Ölhydraulik und Pneumatik, 47, 11-12.

Franco, N. (1961). Pump design by force balance. Hydraulic and Pneumatic, 14(11), 101-107.

Hargreaves, D. J. (1991). Surface waviness effects on the load-carrying capacity of rectangular slider bearings. Wear, 145, 137-151.

Hibbert , G., Lindsay, D. V., Shute, N. A., & Turnbull, D. E. (1971). The balancing of piston and valveplate forces in axial piston pumps and motors. Technical Report British Hydromechanics Research Association.

Huang, C., & Ivantysynova, M. (2003). A new approach to predict the load carrying ability of the gap between valve plate and cylinder block. Proceedings of the Bath Workshop on Power Transmission and Motion Control PTMC, Bath, UK, (pp. 225-239).

Jacazio, G., & Vatta, F. (1981). The block-lift in axial piston hydraulic motors. Proceedings of the ASME/ASCE Bioengineering, Fluids Engineering and Applied Mechanics Conference, (pp. 1-7). Boulder, Colorado, USA.

Jouini, N., & Ivantysynova, M. (2008). Valve plate surface temperature prediction in axial piston machines. Proceedings of the 5th FPNI PhD Symposium, (pp. 95-110). Cracow, Poland.

Kim, J. K., & Jung, J. Y. (2003). Measurement of fluid film thickness on the valve plate in oil hydraulic axial piston pumps (Part I- bearing pad effects). KSME International Journal, 17(2), 246-253.

Kim, J. K., Kim, H. E., & Oh, S. H. (2005). Measurement of fluid film thickness on the valve plate in oil hydraulic axial piston pumps (Part II- sperical design effects). Journal of Mechanical Science and Technology, 19(2), 655-663.

Manring, N. D. (2000). Tipping the cylinder block of an axial piston swash-plate type hydrostatic machine. Journal of Dynamic Systems Measurements and Control, 216-221.

Manring, N. D., Johnson, R. E., & Cheruki, H. P. (2002). The impact of linear deformations on stationary hydrostatic thrust bearings. Journal of Tribology, 124(4), 874-877.

Matsumoto, K., & Ikeya, M. (1991). Friction and leakage characteristics between the valve plate and cylinder for starting and low speed conditions in a swashplate type axial piston motor. Transactions of the Japan Society of Mechanical Engineers - Part C 57, 2023-2028.

Olems, L. (2000). Investigations of the temperature behaviour of the piston cylinder assembly in axial piston pumps. International Journal of Fluid Power, 1(1), 27-38.

Pelosi, M., & Ivatysynova, M. (2011). The influence of pressure and thermal deformation on the piston/cylinder interface film thickness. Proceedings of the 52nd National Conference on Fluid Power 2011, NCFP I11-9.3.

Pelosi, M., & Ivatysynova, M. (n.d.). Surface deformation enables high pressure operation of axial piston pumps. ASME/Bath Symposium on Fluid Power and Motion Control. Arlington, Virginia, USA.

Rasheed, H. (1998). Effect of surface waviness of the hydrodynamic lubrciation of a plain cylindrical sliding element bearing. Wear, 223, 1-6.

Shin, J. H., & Kim, K. W. (2014). Effect of surface non-flatness on the lubrication characteristics in the valve part of a swash-plate type axial piston pump. Meccanica, 49(5), 1275-1295.

Wieczorek, U., & Ivatysynova, M. (2002). Computer aided optimization of bearing and sealing gaps in hydrostatic machines - the simulation tool CASPAR. International Journal of Fluid Power, 3(1), 7-20.

Yamaguchi, A., Sekine, H., Shimizu, S., & Ishida, S. (1990). Bearing/seal characteristics of the oil film between a valve plate and a cylinder block of axial pumps. JHPS, 18(7), 543-550.

Zecchi, M. (2013). A novel fluid structure interaction and thermal model to predict the cylinder block/valve plate interface performance in swash plate type axial piston machines. PhD Thesis, Purdue University.

Zecchi, M., & Ivantysynova, M. (2012). An investigation of the impact of micro surface shaping on the cylinder block/valve plate interface performance through a novel thermo-elasto-hydrodynamic model. The 7th FPNI PhD Symposium on Fluid Power.

Zecchi, M., & Ivantysynova, M. (2012). Cylinder block/valve plate interface - a novel approach to predict thermal surface loads. Proceedings of the 8th IFK. Dresden, Germany.

Zecchi, M., & Ivatysynova, M. (n.d.). A novel fluid structure interaction model for the cylinder block / valve plate interface of axial piston machines. Proceedings of the IFPE 2011. Las Vegas, Nevada, USA.

PUBLICATION

PUBLICATION

Chacon, R. and Ivantysynova, M. (2014). An investigation of the impact of micro surface on the cylinder block/valve plate interface performance. *Proceedings of the 8th FPNI Ph.D Symposium on Fluid Power, Lappeenranta, Finland.*